

# 博士論文 (要約)

Control for dissimilar  
momentum and heat transfer with streamwise  
travelling wave-like wall blowing and suction

(流れ方向進行波状の壁面吹き出し・  
吸い込みを用いた運動量と熱輸送の非相似制御)

カイトッカラ アルジュン ジョン

Kaithakkal Arjun John



# **Control for Dissimilar Momentum and Heat Transfer with Streamwise Travelling Wave-like Wall Blowing and Suction**



**Arjun John Kaithakkal**

Department of Mechanical Engineering  
The University of Tokyo

This dissertation is submitted for the degree of  
*Doctor of Philosophy*

Institute of Industrial Science

August 2020





## **Acknowledgements**

The passion and vigour with which my academic supervisor, Dr. Yosuke Hasegawa, pursue various research topics under the broad umbrella of fluid mechanics has made an everlasting impression on me. I gratefully acknowledge the help and support, both in academic and personal life, he had provided throughout my doctoral studies.

I thank all the members, present and past, of the Interfacial Transport Engineering Lab (Hasegawa Lab) for their encouragement. My years in the lab have gifted me a handful of cheerful moments, thanks to Gatti, Watanabe-san, Kametani-san, Osawa-san, Konstas, and Nakakura-san. For all the memorable moments in Tokyo, I am thankful to Srikanth, Vinod, Ashish, Santwana, Anurag, Shobhit, and Raja. The support from Chakko, Jesil, Vishnu, and Vivek are also acknowledged. I extend my sincere gratitude to Dr. Keiko Ito and the FSSC group of the University of Tokyo.

I sincerely thank Dr. Arnab K. De and Dr. Amaresh Dalal from IIT Guwahati for their guidance and help in my academic pursuit.

I want to thank the Ministry of Education, Culture, Sports, Science, and Technology (MEXT) of Japan for the financial support through its doctoral fellowship program for international students and the Japan Student Services Organization (JASSO) for their funding through MEXT-Honours scholarship.

Last but not least, I am indebted to my siblings: Aswathi, Aparna, Anjali, Anukutty, and parents for their prayers and unrelenting support and encouragement.



# Table of contents

<b>List of figures</b>	<b>ix</b>
<b>List of tables</b>	<b>xv</b>
<b>1 Introduction</b>	<b>1</b>
1.1 Thermo-fluid systems . . . . .	1
1.2 Reynolds analogy and Chilton-Colburn analogy . . . . .	2
1.3 Traveling wave-like blowing and suction control . . . . .	5
1.3.1 Drag reduction . . . . .	5
1.3.2 Heat transfer . . . . .	7
1.4 Generation of traveling wave using passive method . . . . .	8
1.4.1 Heat transfer through porous media . . . . .	9
1.5 Objectives and layout of the thesis . . . . .	10
<b>2 Laminar channel flow</b>	<b>13</b>
2.1 Numerical Methods and Conditions . . . . .	13
2.1.1 Governing equations . . . . .	13
2.1.2 Control input . . . . .	15
2.1.3 Numerical method . . . . .	16
2.1.4 Performance indices . . . . .	16
2.2 Control performance . . . . .	18
2.2.1 Comparison of the performance indices for $Re = 10, 100$ , and $500$ .	18

2.2.2	Effects of control power input on performance indices at $Re = 100$ .	19
2.2.3	Effects of the amplitude of the control input on performance indices for $Re = 100$ . . . . .	22
2.3	Mechanism of dissimilarity . . . . .	24
2.3.1	Influential layer thickness $\delta$ . . . . .	24
2.3.2	Phase analysis of velocity and thermal fields . . . . .	27
2.3.3	Budget analysis . . . . .	28
2.4	Conclusions . . . . .	30
<b>3</b>	<b>Turbulent channel flow</b>	<b>37</b>
3.1	Numerical Methods and Conditions . . . . .	37
3.1.1	Governing equations . . . . .	37
3.1.2	Numerical setup . . . . .	39
3.1.3	Control input . . . . .	40
3.1.4	Control performance indices . . . . .	41
3.2	Control Performances . . . . .	41
3.2.1	Skin-friction coefficient . . . . .	41
3.2.2	Stanton number . . . . .	44
3.2.3	Analogy factor . . . . .	44
3.2.4	Reynolds number effect and the scaling of the optimal wave parameters	47
3.3	Mechanisms of Dissimilarity . . . . .	51
3.3.1	Triple decomposition . . . . .	51
3.3.2	Decomposition into coherent and random contributions . . . . .	54
3.3.3	Coherent contribution for the globally optimal control input . . . . .	59
3.3.4	Random contribution for the globally optimal control input . . . . .	64
3.3.5	Visualization of the turbulence structures . . . . .	71
3.4	Discussions . . . . .	72
3.5	Conclusions . . . . .	76

<b>4 Conclusions</b>	<b>81</b>
<b>References</b>	<b>85</b>
<b>Appendix A Grid resolution effect</b>	<b>91</b>
A.1 Laminar channel flow . . . . .	91
A.2 Turbulent channel flow . . . . .	92
<b>Appendix B Effects of phase-angle</b>	<b>95</b>
B.1 Laminar channel flow . . . . .	95
B.2 Turbulent channel flow . . . . .	95
<b>Appendix C Budget equations</b>	<b>99</b>
C.1 Governing equations for the coherent and random components . . . . .	99
C.1.1 Derivation of the governing equations for the coherent components	99
C.1.2 Derivation of the governing equations for the random components .	100
C.2 Budget equation for $\overline{\tilde{v}(\tilde{\theta} - \tilde{u})}$ . . . . .	101
C.3 Budget equation for $\overline{v''(\theta'' - u'')}$ . . . . .	102
C.4 Budget equations for turbulent channel flow . . . . .	104
<b>Appendix D Optimal control analysis</b>	<b>109</b>
D.1 Governing Equations . . . . .	109
D.1.1 Numerical Methodology . . . . .	110
D.1.2 Performance indices . . . . .	112
D.1.3 Parametric study . . . . .	112
D.1.4 Optimal control analysis . . . . .	113
D.1.5 Results . . . . .	115



# List of figures

1.1	Analogy factor $A$ as a function of $Re_{D_h}$ for different heat transfer surfaces. Here $Re_{D_h}$ is the Reynolds number based on the hydraulic diameter $D_h$ which for a plain channel is given by $D_h = 4\delta$ , where $\delta$ is the half channel height. For laminar regime (dashed line), <i>i.e.</i> $Re_{D_h} < 3000$ , a constant heat flux condition is assumed resulting in a constant value for $A = 0.69$ . For the turbulent regime (solid line) $C_f = 0.087Re_{D_h}^{-1/4}$ (Dean, 1978) and $j = 0.024Re_{D_h}^{-1/5}Pr^{1/6}$ (Keys et al., 2005). For both laminar and turbulent regime $Pr$ is set equal to one. . . . .	4
1.2	Schematic showing traveling wave-like wall blowing and suction applied to a channel flow. . . . .	5
1.3	Schematic of heat transfer surfaces stacked one over other. . . . .	9
2.1	Schematic of the flow domain and the coordinate systems. . . . .	14
2.2	Contours of $C_f/C_{f_0}$ , $St/St_0$ , and $A$ as a function of $(\lambda_x, U_p)$ : $Re = 10$ (top row), $Re = 100$ (middle row), $Re = 500$ (bottom row). Contours with a value less than or equal to one are shown using dashed lines. . . . .	18
2.3	Contour plots of $\Pi_{net}$ , $\Pi_{csv}$ , $C_{f_{net}}/C_{f_0}$ , and $C_{f_{csv}}/C_{f_0}$ as a function of $(\lambda_x, U_p)$ for $Re = 100$ . In figure 2.3a, contours with a value less than or equal to zero are shown using dashed lines. . . . .	20
2.4	Contour plots of $A_{net}$ and $A_{csv}$ , as a function of $(\lambda_x, U_p)$ for $Re = 100$ . Contours with a value less than or equal to one are shown using dashed lines. . .	21
2.5	Effect of $\lambda_x$ on the control performance for $U_p = 0.75$ at $Re = 100$ . . . . .	21
2.6	Effects of $\phi_{rms}$ on skin friction drag and heat transfer for $(\lambda_x, U_p) = (2\pi, 0.75)$ at $Re = 100$ . . . . .	24

2.7	Wall-normal distributions of $\overline{yu'v'}$ , $\overline{y\theta'v'}$ , and $\overline{y(\theta' - u')v'}$ for $(\lambda_x, U_p) = (2\pi, 0.75)$ at $Re = 100$ . . . . .	25
2.8	Variation of (a) $\delta_{C_f}^N$ & $\delta_{St}^N$ and (b) $M_{C_f}/C_{f0}$ & $M_{St}/St_0$ as a function of $U_p$ for $(\lambda_x, U_p) = (2\pi, 0.75)$ at different Reynolds numbers. . . . .	27
2.9	Contour plots of the coherent components: (a) $\tilde{\theta}$ , (b) $\tilde{u}$ , (c) $(\tilde{\theta} - \tilde{u})$ , (d) $\tilde{v}$ , (e) $\tilde{p}$ , and (f) $\langle y(\tilde{\theta} - \tilde{u})\tilde{v} \rangle$ as a function of $(\xi, y)$ for $(\lambda_x, U_p) = (2\pi, 0.75)$ at $Re = 100$ . The arrows in the background of $\tilde{\theta}$ are the vector field $(\langle u \rangle - U_p, \tilde{v})$ scaled by a factor of 100. . . . .	29
2.10	Terms in the budget equation of $-\overline{(\theta' - u')v'}$ : $P$ = production; $T_D$ & $V_D$ = turbulent and molecular diffusion; $\Pi$ = pressure-velocity-temperature correlation; $\varepsilon$ = molecular dissipation, for $(\lambda_x, U_p) = (2\pi, 0.75)$ at $Re = 100$ . . . . .	31
2.11	The $\xi - y$ distribution of $\Pi$ and its two constituent terms. . . . .	31
2.12	Analogy factor $A$ as a function of $Re_{D_h}$ for different heat transfer surfaces. The figure is same as that shown in 1.1 but with the data points included from the present study. Here $Re_{D_h}$ is the Reynolds number based on the hydraulic diameter $D_h$ which for a plain channel is given by $D_h = 4\delta$ , where $\delta$ is the half channel height. For laminar regime (dashed line), <i>i.e.</i> $Re_{D_h} < 3000$ , a constant heat flux condition is assumed resulting in a constant value for $A = 0.69$ . For the turbulent regime (solid line) $C_f = 0.087Re_{D_h}^{-1/4}$ (Dean, 1978) and $j = 0.024Re_{D_h}^{-1/5}Pr^{1/6}$ (Keys et al., 2005). For both laminar and turbulent regime $Pr$ is set equal to one. . . . .	33
2.13	Same plot as in figure 2.12, except that $A_{csv}$ is plotted instead of $A$ from the present study. . . . .	34
3.1	Schematic of the flow domain. . . . .	38
3.2	Normalized skin-friction coefficient $C_f/C_{f0}$ . Contours with a value less than or equal to one are shown by dashed lines. . . . .	42
3.3	Skin-friction coefficient: (a) $C_{f_{net}}/C_{f0}$ and (b) $C_{f_{csv}}/C_{f0}$ . Contours with a value less than or equal to one are shown by dashed lines. . . . .	43
3.4	Normalized Stanton number $St/St_0$ . Contours with a value less than or equal to one are shown by dashed lines. . . . .	44



- 3.5 Analogy factor  $A$ . The red circle indicates the wave parameters  $(\lambda_x, U_p) = (1.96, 0.30)$  obtained from the optimal control theory (Yamamoto et al., 2013) and the red triangle indicates the global optimum of the wave parameters, i.e.,  $(\lambda_x, U_p) = (1.12, 0.30)$  obtained from the present DNSs. Contours with a value less than or equal to one are shown by dashed lines. . . . . 45
- 3.6 Analogy factor: (a)  $A_{net}$  and (b)  $A_{csv}$ . The circle indicates the wave parameters  $(\lambda_x, U_p) = (1.96, 0.30)$  obtained from the optimal control theory (Yamamoto et al., 2013) and the triangle indicates the global optimum of wave parameters  $(\lambda_x, U_p) = (1.12, 0.30)$  obtained from the present DNSs. Contours with a value less than or equal to one are shown by dashed lines. . . 45
- 3.7 Contour plot of (a)  $C_f/C_{f0}$ , (b)  $St/St_0$ , and (c)  $A$ , as a function of  $(\lambda_x, U_p)$  for  $Re_\tau = 300$ . Contours with a value less than or equal to one are shown by dashed lines. . . . . 47
- 3.8 Contour plot of (a)  $C_f/C_{f0}$ , (b)  $St/St_0$ , and (c)  $A$ , as a function of  $(\lambda_x^+, U_p^+)$  for  $Re_\tau = 150$  (black lines) and  $Re_\tau = 300$  (thick red lines). Contours with a value less than or equal to one are shown by dashed lines. . . . . 49
- 3.9 Analogy factor  $A$  as a function of  $Re_{D_h}$  for different heat transfer surfaces. The figure is same as that shown in 1.1 but with the data points included from the present study. Here  $Re_{D_h}$  is the Reynolds number based on the hydraulic diameter  $D_h$  which for a plain channel is given by  $D_h = 4\delta$ , where  $\delta$  is the half channel height. For laminar regime (dashed line), i.e.  $Re_{D_h} < 3000$ , a constant heat flux condition is assumed resulting in a constant value for  $A = 0.69$ . For the turbulent regime (solid line)  $C_f = 0.087Re_{D_h}^{-1/4}$  (Dean, 1978) and  $j = 0.024Re_{D_h}^{-1/5}Pr^{1/6}$  (Keys et al., 2005). For both laminar and turbulent regime  $Pr$  is set equal to one. . . . . 52
- 3.10 Same plot as in figure 3.9, except that  $A_{csv}$  is plotted instead of  $A$  from the present study. . . . . 53
- 3.11 Comparison of  $C_f$  and  $St$  estimated from FIK-identity equations (3.10) and (3.11) with those obtained from direct integration of wall shear stress and wall heat flux given by equations (1.1) and (1.2) for all 140 cases considered in the present DNSs. . . . . 55
- 3.12 Contour plots of (a)  $\Delta C_f^C/C_{f0}$ , (b)  $\Delta C_f^R/C_{f0}$ , (c)  $\Delta St^C/St_0$ , and (d)  $\Delta St^R/St_0$  as functions of  $\lambda_x$  and  $U_p$ . Contours with a value less than or equal to 0 are shown using dashed lines. . . . . 57

3.13	Contributions of (a) coherent and (b) random components to the analogy factor. Contours with a value less than or equal to 0 are shown using dashed lines. . . . .	58
3.14	Wall-normal distributions of the integrands of the coherent and random contributions to dissimilarity (refer equation (3.16)). . . . .	59
3.15	$\xi - y$ distribution of coherent contribution $\langle y\tilde{v}(\tilde{\theta} - \tilde{u}) \rangle$ . The red dashed line indicates the location of $y = -0.90$ , where the coherent contribution has a positive peak. Contours with a value less than 0 are shown using dashed lines. . . . .	60
3.16	Contour plots of the coherent components: (a) $\tilde{\theta}$ , (b) $\tilde{u}$ , (c) $\tilde{\theta} - \tilde{u}$ , (d) $\tilde{v}$ , and (e) $\tilde{p}$ . Contours with a value less than 0 are shown using dashed lines. . . . .	61
3.17	Enlarged view of $\tilde{\theta}$ in the near wall region. The vectors show the phase-averaged velocity field $(\langle u \rangle - 0.30, \tilde{v})$ . Contours with a value less than 0 are shown using dashed lines. . . . .	62
3.18	Terms in the budget equation for (a) $-\overline{\tilde{v}\tilde{u}}$ , (b) $-\overline{\tilde{v}\tilde{\theta}}$ , and (c) $-\overline{\tilde{v}(\tilde{\theta} - \tilde{u})}$ . $P_C$ = production; $P_{C1_C}$ & $P_{C2_C}$ = coupling terms; $T_{D_C}$ & $V_{D_C}$ = turbulent and molecular diffusion; $\Pi_C$ = correlation between velocity/temperature fluctuation and pressure gradient; $\epsilon_C$ = molecular dissipation. . . . .	65
3.19	Terms in the budget equation for (a) $-\overline{v''u''}$ , (b) $-\overline{v''\theta''}$ , and (c) $-\overline{v''(\theta'' - u'')}$ . $P_R$ = production; $P_{C1_R}$ & $P_{C2_R}$ = coupling terms; $T_{D_R}$ & $V_{D_R}$ = turbulent and molecular diffusion; $\Pi_R$ = correlation between velocity/temperature fluctuation and pressure gradient; $\epsilon_R$ = molecular dissipation. . . . .	67
3.20	Gradient of the difference between the mean temperature and velocity along the lower half of the channel. $y_p = -0.96$ and $y_n = -0.81$ correspond to the locations where the random contribution to dissimilarity have positive and negative peaks, respectively . . . . .	68
3.21	$\xi - y$ distribution of the random contribution $\langle y(\theta''v'' - u''v'') \rangle$ . The dash-dotted line (red) and dashed (blue) line represent the location of $y_p = -0.81$ and $y_n = -0.96$ where the random contribution to dissimilarity have positive and negative peaks, respectively. Contours with a value less than 0 are shown using dashed lines. . . . .	68

- 3.22 a) The ratio of the wall-normal gradients of the phase-averaged temperature and velocity fields,  $S$ , and b) the inverse of the turbulent Prandtl number for the random component,  $(Pr_t'')^{-1}$ . The red dash-dotted and blue dashed lines represent the locations of  $y_p = -0.81$  and  $y_n = -0.96$  where the random contribution to dissimilarity have positive and negative peaks, respectively. Contours with a value less than or equal to 1 are shown using dashed lines. . . . . 70
- 3.23 Instantaneous distribution of the random contribution  $yv''(\theta'' - u'')$  in the bottom half of the channel at  $\xi = 0$ . The enlarged view of the near-wall region is shown in the bottom figure. The vectors show the random velocity components  $(v'', w'')$ . The red dash-dotted and blue dashed lines represent the locations of  $y_p = -0.81$  and  $y_n = -0.96$  where the random contribution to dissimilarity have positive and negative peaks, respectively. . . . . 70
- 3.24 Top view of the isosurfaces of  $Q^+ = -0.03$  for the uncontrolled (*top*) and controlled (*bottom*) (for the optimal case) channel flow at  $Re_\tau = 150$ . . . . . 72
- 3.25 Isosurfaces of  $Q^+ = 0.03$  (white),  $yv''(\theta'' - u'') = 0.01$  (red), and  $yv''(\theta'' - u'') = -0.01$  (blue) for the bottom half of (a) uncontrolled flow and (b) controlled flow with the globally optimal input at  $Re_\tau = 150$ . The arrows in the controlled case represents wall blowing and suction which is uniform in the spanwise direction. . . . . 73
- 3.26 Wall-normal distributions of the eddy viscosity  $E_{v_0}$  (solid line) and eddy diffusivity  $E_{d_0}$  (dashed line) for the uncontrolled flow. . . . . 76
- 3.27 Analogy factor  $A$  obtained from URANS simulations. The circle and triangle indicates the control input obtained from the optimal control theory (Yamamoto et al., 2013) and the global optimum obtained in the present DNS, respectively. Contours with a value less than or equal to 1 are shown using dashed lines. . . . . 77
- 3.28 Contour plot of  $C_f/C_{f_0}$  obtained from URANS. Contours with a value less than or equal to 1 are shown using dashed lines. . . . . 77
- 3.29 Contour plot of  $St/St_0$  obtained from URANS. . . . . 78
- A.1 Effect of grid resolution on the performance indices for the reference phase speed of  $U_p = 0.75$  at  $Re = 500$ . . . . . 91

A.2	Contour plot of $A$ around the optimal point $(\lambda_x, U_p) = (5\pi/14, 0.30)$ . The black contours represent Case O and thick red contours represent Case 1 (refer Table A.1). The + indicates the 35 cases for which the additional simulations are carried out. . . . .	92
A.3	Variation of (a) $C_f/C_{f_0}$ and $St/St_0$ and (b) $A$ as a function of $U_p$ for $\lambda_x = 5\pi$ . The black lines represent Case - O and thick red lines represent Case - 2 (refer Table A.1). The + indicates the 10 cases for which the additional simulations are carried out. . . . .	93
B.1	Effect of phase-angle on the performance indices for the optimal point of $(\lambda_x, U_p) = (2\pi, 0.75)$ at $Re = 100$ . The phase-angles equal to zero and 180 degree correspond to sinuous and varicose modes, respectively. . . . .	96
B.2	$C_f/C_{f_0}$ , $St/St_0$ , and $A$ as a function of phase-angle between the top and bottom wall for (a) the globally optimal point $(\lambda_x, U_p) = (5\pi/14, 0.30)$ and (b) $(\lambda_x, U_p) = (5\pi/4, 0.30)$ . . . . .	97
D.1	Dimensions of the computational domain and coordinate system. . . . .	110
D.2	Update of cost functional ( $J$ ), skin friction coefficient ( $C_f/2$ ), and Stanton number ( $St$ ) with iteration. . . . .	116
D.3	Snapshots of the streamwise velocity field ( <i>left</i> ) and temperature field ( <i>right</i> ) for three different time steps: from top to bottom, $t = 0$ ( <i>initial field</i> ); $t = 4$ ; $t = 27$ . The velocity vectors shown at the top and bottom wall represent the profile of the optimal control input for that particular time instant. A unit wall normal velocity vector is shown at $x = 15.83$ in the velocity field for $t = 0$ (top left figure) using a red arrow, as a reference. . . . .	117
D.4	The streamwise variation of the RMS value of the control input. . . . .	118

# List of tables

2.1	Comparison of the present traveling wave parameters with those used by Min et al. (2006), Mamori et al. (2010), and Higashi et al. (2011). . . . .	15
2.2	Effects of $\phi_{rms}$ on performance indices for $(\lambda_x, U_p) = (2\pi, 0.75)$ at $Re = 100$ . . . . .	23
3.1	Summary of the control performances for the globally optimal control input with $(\lambda_x, U_p) = (1.12, 0.30)$ . . . . .	46
3.2	Computational domain size, number of spectral modes, number of grid points and grid spacing in physical space, and the time-step used for $Re_\tau = 150$ and 300, respectively. . . . .	50
3.3	Summary of the control performances for $Re_\tau = 150$ and 300 at their respective optimal points. Here $(\lambda_x^+, U_p^+)$ and $(\lambda_{xc}^+, U_{pc}^+)$ respectively represents quantities normalised in wall units corresponding to the un-controlled and controlled flow. . . . .	50
A.1	Computational domain size, number of spectral modes, number of grid points in the physical space, and grid spacing used for the grid resolution check. . . . .	92
D.1	Control Performance . . . . .	115



# Chapter 1

## Introduction

### 1.1 Thermo-fluid systems

Thermo-fluids devices like heat exchangers have a wide range of industrial applications leading to a never-ending demand for improving their energy efficiencies. For the ease of analysis, the heat exchangers can be thought of as internal flows with heat transfer. Now depending on whether an internal flow system is dominated by natural or forced convection, the objectives for improving the energy efficiency are different.

For natural convection dominated systems, the objective is to improve the heat flux for a given temperature difference. In the non-dimensional form, this can be represented as  $Nu = Nu(Ra)$ . Here, the Nusselt number  $Nu$  and the Rayleigh number  $Ra$  respectively represent heat flux and temperature difference, in their dimensionless formats. For the classical turbulent Rayleigh-Bénard convection, that serves as the canonical system for the study on natural convection, the relation follows as  $Nu \propto Ra^\beta$ , where  $0.28 \lesssim \beta \lesssim 0.5$  (Hewitt, 2014). Tremendous effort has been made to identify techniques that can improve  $Nu$  for a given  $Ra$  with (active techniques) or without (passive techniques) using additional power input (see e.g. Wang et al. (2019)).

However, for forced convection dominated system, an effort intended to improve the energy efficiency need to simultaneously aim at decreasing the pressure loss and increasing the heat transfer. The pressure loss and the heat transfer are respectively quantified using the non-dimensional parameters, *i.e.*, the skin-friction coefficient  $C_f$  and the Stanton number  $St$ , defined as

$$C_f = \frac{2}{Re} \left( \frac{d\bar{u}}{dy} \right)_w, \quad (1.1)$$

$$St = \frac{1}{RePr} \left( \frac{d\bar{\theta}}{dy} \right)_w. \quad (1.2)$$

Here, the Reynolds number  $Re$  denotes the relative importance of inertia force over viscous force and the Prandtl number  $Pr$  denotes the ratio of momentum and thermal diffusivities of the fluid; whereas  $d\bar{u}/dy$  and  $d\bar{\theta}/dy$  represent the mean velocity and temperature gradients in the wall-normal direction, respectively. The subscript  $w$  indicates a quantity on the wall. Note that the Stanton number is related to the Nusselt number via  $St = Nu/RePr$ . The ultimate aim for the heat transfer community is to achieve least conceivable pressure loss and secure maximum possible heat transfer, *i.e.* to decrease  $C_f$  and to increase  $St$ . This is, however, challenging due to the similarity in the transport mechanisms of momentum and heat transfer.

## 1.2 Reynolds analogy and Chilton-Colburn analogy

The similarity between momentum and heat transfer was first recognized by Reynolds (Reynolds, 1874) through the currently well-known concept as ‘Reynolds analogy’. The analogy is based on the similarity in the governing equations as well as the transport mechanisms pertaining to momentum and heat transfer. It predicts that at  $Pr$  around unity,

$$2St \approx C_f. \quad (1.3)$$

The above equation was later modified by Chilton & Colburn (Chilton and Colburn, 1934) to take into account the effect of the Prandtl number and equation (1.3) is rewritten as

$$2j \approx C_f, \quad (1.4)$$

where  $j = StPr^{2/3}$  is called the Colburn factor. Even though equations (1.3) and (1.4) are not based on any physical laws, they serve as quite useful tools in industrial applications to predict heat transfer rate once the value of pressure loss is known.

It should be noted, however, that even if the governing equations of momentum and heat transfer are similar, their respective dynamics were found to show non-negligible dissimilarity for the canonical flow configurations such as boundary layer (Antonia et al., 1988), mixing layer (Fiedler, 1975), channel flow (Antonia et al., 2009), and pipe flow (Bremhorst and Bullock, 1970). Since the Reynolds analogy is based on the similarity in the transport equations of momentum and heat, it is expected to be valid when  $Pr$  is equal



to unity and at the same time the governing equations, as well as the boundary conditions, of streamwise momentum and temperature are in an identical form (Kasagi et al., 2012; Kestin and Richardson, 1963). Nonetheless, even under such ideal scenarios dissimilarity is observed for turbulent Couette flow (Pasinato, 2011) and channel flow (Pasinato, 2011; Zhou et al., 2019).

The series of above results suggest towards the possibility of further enhancing the dissimilarity between heat and momentum transfer through flow control. For example, previous studies (Foures et al., 2014; Hassanzadeh et al., 2014; Motoki et al., 2018) applied a variational approach to find out the optimal perturbations to enhance scalar mixing for a given base flow. Considering that it is not always feasible to introduce such a three-dimensional perturbation throughout a flow domain, one alternative is to manipulate the flow from a fluid-solid boundary by either active or passive means. These flow control techniques cause large deviations from Reynolds analogy. Such a scenario is termed as dissimilar heat transfer and can be quantified using the analogy factor  $A$  defined as

$$A = 2j/C_f. \quad (1.5)$$

The existing heat transfer enhancement techniques, such as dimples (Elyyan et al., 2008), offset fins (Manglik and Bergles, 1995), wavy fins (Ismail and Velraj, 2009), louvered fins (Achaichia and Cowell, 1988; Dong et al., 2007), riblets (Han et al., 1978), vortex generators (Fiebig, 1995) etc., in fact, result in enhanced heat transfer at the expense of further increase in the pressure drop. As a result, the ratio between the Stanton number and the skin friction coefficient is commonly lower than that of a flat wall, *i.e.*  $A < 1.0$ , as can be seen in figure 1.1. Even the widely recognized drag-reducing techniques such as polymer additives are no exception; it has been shown numerically that polymer additives also results in  $A < 1.0$  for a turbulent channel flow (TCF) (Yu and Kawaguchi, 2005). However, a carefully designed traveling wave-like wall blowing and suction control input is found capable of achieving  $A > 1.0$  (Hasegawa and Kasagi, 2011; Higashi et al., 2011; Yamamoto et al., 2013) (refer figure 1.1).

In this thesis, by making use of the canonical flow configuration of a channel flow, we analyse the dissimilar effect on momentum and heat transfer by a control input in the form of a traveling wave-like wall blowing and suction.

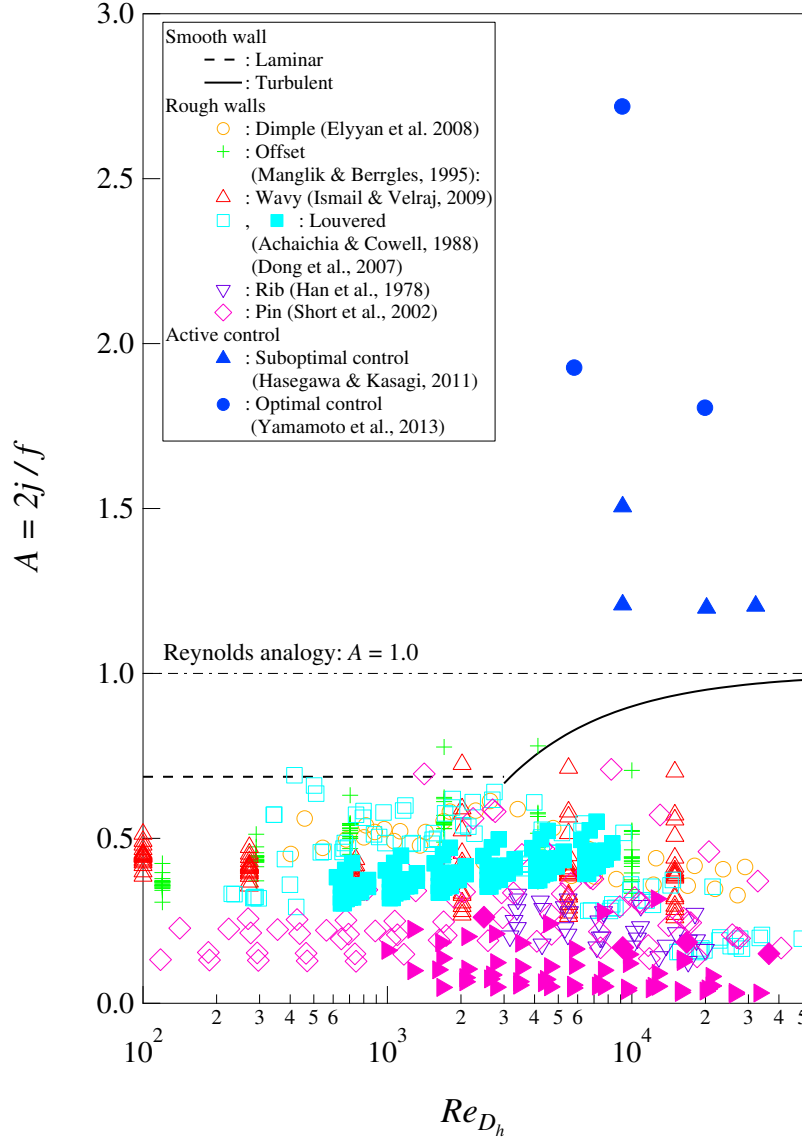


Figure 1.1 Analogy factor  $A$  as a function of  $Re_{D_h}$  for different heat transfer surfaces. Here  $Re_{D_h}$  is the Reynolds number based on the hydraulic diameter  $D_h$  which for a plain channel is given by  $D_h = 4\delta$ , where  $\delta$  is the half channel height. For laminar regime (dashed line), *i.e.*  $Re_{D_h} < 3000$ , a constant heat flux condition is assumed resulting in a constant value for  $A = 0.69$ . For the turbulent regime (solid line)  $C_f = 0.087Re_{D_h}^{-1/4}$  (Dean, 1978) and  $j = 0.024Re_{D_h}^{-1/5}Pr^{1/6}$  (Keys et al., 2005). For both laminar and turbulent regime  $Pr$  is set equal to one.

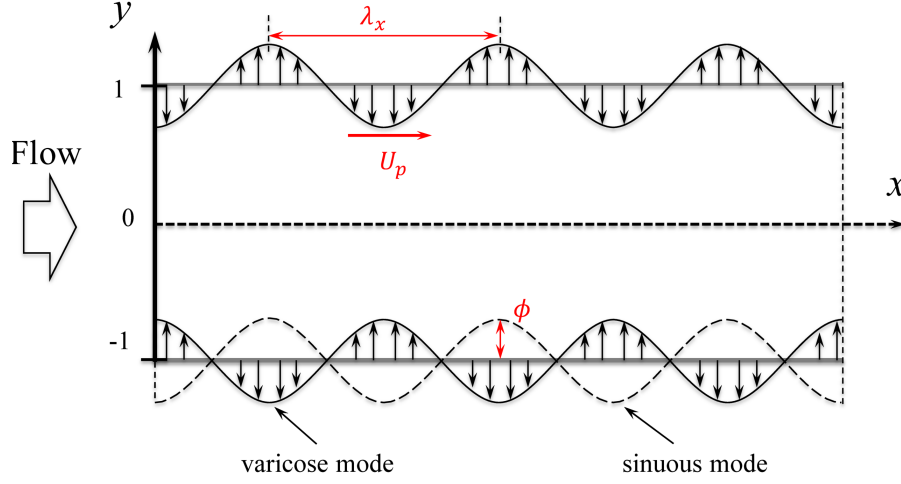


Figure 1.2 Schematic showing traveling wave-like wall blowing and suction applied to a channel flow.

### 1.3 Traveling wave-like blowing and suction control

The sinusoidal traveling wave with zero-net-mass-flux wall blowing and suction is defined as

$$v_w = \phi \sin \left\{ \frac{2\pi}{\lambda_x} (x - U_p t) \right\}, \quad (1.6)$$

where,  $\phi$ ,  $\lambda_x$ , and  $U_p$  are the amplitude, wavelength, and phase-speed of the traveling wave, respectively. Figure 1.2 shows the schematic of a traveling wave-like wall blowing and suction control input in two-dimensional channel flow configuration. The control input is called an upstream traveling wave (UTW) when  $U_p < 0$  and a downstream traveling wave (DTW) when  $U_p > 0$ . Also, depending on the phase difference between the control input at the top and bottom wall they can be called either a sinuous mode configuration, when the phase difference is zero, or a varicose mode configuration, when the phase difference is  $180^\circ$ .

#### 1.3.1 Drag reduction

Wall blowing and suction is a typical example of an active control technique. It was Choi et al. (1994) who first introduced the drag reduction capability of wall blowing and suction, now commonly referred to as the 'opposition control'. This control input was found effective for both turbulent- channel flows (Choi et al., 1994) as well as boundary layers (Kametani and Fukagata, 2011). Subsequent work by Min et al. (2006) showed that a sub-laminar drag, that is a drag below that of the laminar regime, can be achieved using wall blowing and

suction in the form of a traveling wave in a channel flow. However, studies by Fukagata et al. (2009) and Bewley (2009) explained that there is a fundamental limitation for performance by traveling wave-like wall blowing and suction: *"Power of the control input applied at the walls is always larger than the power saved (due to drag reduction below the laminar level)"* (Bewley, 2009). So from an energetic view point, *i.e.* taking into account the energy required to drive the control input, the ultimate aim for flow control is to relaminarise the flow field. Studies by Ogino et al. (2019) and Koganezawa et al. (2019) established the drag reduction capability of the traveling wave-like wall blowing and suction control input in other canonical flow configurations such as the turbulent Taylor–Couette flow and pipe flow, respectively.

There exists two distinct mechanisms of drag reduction by a traveling wave-like wall blowing and suction in a channel flow. The first one is the so-called streaming (or pumping) effect, which causes a net mass flux in the opposite direction to the applied traveling wave even without imposing a pressure gradient (Hoepffner and Fukagata, 2009). Since the control input itself assists to drive the flow downstream, the external pressure gradient for achieving a given flow rate can be reduced. This effect exists for both laminar and turbulent flows. By analyzing the phase-relationship between the fluctuating velocity components Mamori et al. (2010) revealed that the viscous effect induces a near-wall phase shift between streamwise and wall-normal velocity fluctuations, and thus generates the Reynolds shear stress, which is the origin of the streaming effect. They also found that a varicose mode is more effective than a sinuous mode for achieving drag reduction. Woodcock et al. (2012) derived an asymptotic expression for an induced net flow due to the streaming effect and confirmed that the varicose mode is more effective.

The second mechanism is the stabilising effect through interaction between the applied traveling wave-like control input and the underlying wall turbulence. Obviously, it is present only in turbulent and not in laminar channel flows. The stability analysis by Lee et al. (2008) revealed that the drag reducing UTWs destabilises a turbulent flow, hence the drag reduction achieved by (Min et al., 2006) is mostly caused by the streaming effect. Their analysis also showed that streak amplification due to transient growth is significantly suppressed when a DTW is applied. It was later proved that significant drag reduction, and even relaminarization can be achieved using a DTW (Lieu et al., 2010) when the parameters of the traveling wave are determined based on the receptivity analysis (Moarref and Jovanović, 2010). Following studies by different researchers clarified on the impact of traveling wave parameters on drag reduction and found that the varicose mode is most effective in reducing the drag (*e.g.* Mamori et al. (2014); Quadrio et al. (2007); Woodcock et al. (2012)).

### 1.3.2 Heat transfer

Although the complex responses of skin-friction drag to various control inputs have been extensively investigated, studies considering their impacts on the thermal field and the dissimilarity between momentum and heat transfer are still limited. [Suzuki et al. \(1988\)](#) and [Inaoka et al. \(1999\)](#) considered a turbulent boundary layer disturbed by insertion of a cylinder and a square duct, respectively. They observed significant dissimilarity downstream of the obstacles. [Matsubara et al. \(2015\)](#) also conducted direct numerical simulations (DNSs) of a TCF with a spanwise rib, and the detailed mechanisms of dissimilarity caused by the spanwise rib were discussed based on flow visualization, statistics, and spectral analyses. With respect to active control, dissimilarity caused by wall blowing from a spanwise slot in a turbulent boundary layer is considered in [Kong et al. \(2001\)](#) and [Araya et al. \(2008\)](#). Although the above studies clearly show the responses of the velocity and thermal fields to a disturbance are fundamentally different, they mostly focus on the local effects downstream of the region where a control is applied.

Studies considering the dissimilar response of velocity and temperature field in a channel flow subjected to a travelling wave-like wall blowing and suction control are also quite limited. Based on their DNSs and by considering a limited parameter range for the traveling wave-like control input, [Higashi et al. \(2011\)](#) showed that it is possible to have dissimilar heat transfer enhancement, *i.e.* simultaneous achievement of heat transfer augmentation and friction drag reduction, by applying UTW, for both laminar- and turbulent channel flows. However, the optimal control analysis by [Hasegawa and Kasagi \(2011\)](#) and [Yamamoto et al. \(2013\)](#) found that DTWs in varicose mode configuration as the most suitable candidate for achieving dissimilar heat transfer enhancement.

The study by [Yamamoto et al. \(2013\)](#) indicated that, for a TCF, the optimal wave have a wavelength around 250 in wall units and phase velocity approximately 30% of the bulk mean velocity. Though these results are based on the optimal control analysis, there is no guarantee that these values are indeed the global optimum due to the following two reasons. First, [Yamamoto et al. \(2013\)](#) used the gradient-based method to updated the control inputs, so that the resultant control inputs may have reached only a local minima. Second, the time horizon in their optimization is set to be  $T^+ = 100$  in the wall unit, which is still much smaller than the time period ( $T^+ \sim O(10^4)$ ) required to obtain converged statistics. Ideally, the time horizon employed in the optimal control theory should be large enough, so that it takes into account the entire future dynamics until the controlled flow reaches a statistically equilibrium state. Nonetheless, increasing the time horizon above  $T^+ = 100$  not only requires huge computational resources, but also causes numerical instability in

solving the adjoint equations backward in time (Yamamoto et al., 2013). This also poses a fundamental question on to what extent the optimal control theory with a limited time horizon could predict the global optimal parameters of the traveling wave-like input for dissimilar heat transfer enhancement.

More recently, Floryan and Zandi (2019) considered a traveling wave-like wall deformation in a laminar channel flow (LCF). Through a detailed analyses of particle trajectories within the fluid, they demonstrated the ability of DTW to cause drag reduction and mixing enhancement. Even though the particle trajectories provide useful information on mixing mechanisms inside the flow, it is not directly linked to the heat and mass transport from the wall to the bulk of a fluid, which is the main interest in the present thesis.

Thus, there exists the absence of a systematic study on the effect of traveling wave parameters on dissimilar heat transfer and a lack of clarity on the generation mechanism of dissimilarity. These issues are covered for a laminar and turbulent channel flow in detail in chapters 2 and 3, respectively.

## 1.4 Generation of traveling wave using passive method

As will be shown in chapters 2 and 3, a characteristic feature common at the optimal point for both laminar- and turbulent channel flows, subjected to a traveling wave-like blowing and suction, is the presence of a spanwise roll. These rollers are created near the wall and plays a prominent role in the dissimilarity generated between momentum and heat transfer. Similar spanwise rolls have also been observed over flow configurations that allow wall transpiration, *i.e.* a non-zero value for the wall-normal velocity on the wall. Examples include flows over plant canopies (Finnigan, 2000), riblets (García-Mayoral and Jiménez, 2011), and porous surfaces (Jimenez et al., 2001). So for reproducing the dissimilar heat transfer mechanism generated by a traveling wave-like blowing and suction passively, we are left with using either riblets or porous surfaces.

Considering real world applications, it is common to have connected parallel channel flows as schematically shown in figure 1.3. Meanwhile, it has been shown both experimentally and numerically (see *e.g.* Bons (2002), Stalio and Nobile (2003), Forooghi et al. (2018)) that the heat transfer efficiency of ribbed surfaces are below that of the smooth surfaces. These studies have found that, for riblets, the heat transfer efficiency quantified in terms of the analogy factor  $A$  is less than for smooth surface, *i.e.*  $A/A_0 < 1$ , where  $A_0$  represents the

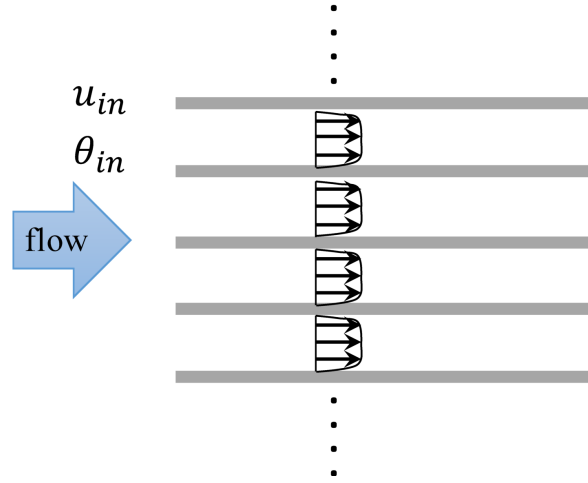


Figure 1.3 Schematic of heat transfer surfaces stacked one over the other.

analogy factor for flat surface. This lead us to the selection of porous surfaces as the natural choice for generating traveling wave-like blowing and suction passively.

### 1.4.1 Heat transfer through porous media

Owing to large surface area to volume ratio of porous materials they act as effective passive control technique for enhancing the heat transfer. The classical example is that of the Rayleigh-Bénard systems for natural convection flows. Instead of the  $Nu \propto Ra^{1/3}$  scaling for pure-fluid Rayleigh-Bénard convection, the porous Rayleigh-Bénard convection follows a linear scaling of  $Nu \propto Ra$  (Hewitt et al., 2012). Thus giving a higher heat flux  $Nu$  for the same given temperature difference  $Ra$  for the porous Rayleigh-Bénard convection compared to that of a pure-fluid Rayleigh-Bénard convection. This perfectly demonstrates the importance of having a sound understanding of the flow through porous media.

Consequently, literature covering analytical, experimental, and numerical studies on flow through porous media are exhaustive. The three volumes of 'Transport phenomena in porous media' edited by Ingham and Pop (Ingham and Pop, 1998, 2002, 2005) speaks for itself. This also owes to the ubiquitous character of flow through porous media both in nature and industrial applications. Flow over canopies and river beds (Nepf, 2012), heat transfer operations in packed beds (Boomsma et al., 2003), porous burners (Howell et al., 1996), transpiration cooling (Dahmen et al., 2015) etc. are to name a few. For knowing the recent trends in these topics see the review by Wood et al. (2020).

With reference to porous TCFs, it has been well established that the wall permeability of the porous media lead to enhanced momentum transfer compared to that of an impermeable wall, leading to increase in skin-friction drag. The Kelvin-Helmholtz instability initiated spanwise rollers, on top of the low- and high-speed streaks and quasi streamwise vortices that already exists in impermeable TCFs, have been associated with this increased momentum transfer (Breugem et al., 2006; de Segura et al., 2018; Jimenez et al., 2001; Suga et al., 2018). These spanwise rollers are generated by wall-normal permeability of the substrate. Thus by controlling the wall-normal permeability of the substrate with respect to the wall permeability in the streamwise and spanwise direction, it is possible to minimise the increase in drag or even achieve drag reduction compared to the impermeable wall (de Segura et al., 2018; Rosti et al., 2018). However, when the ratio of permeability along the wall-normal direction to that along streamwise direction is greater than one, the study by Suga and Kuwata (2017) and Suga et al. (2018) showed that, the streamwise permeability have the strongest impact on wall turbulence, whereas the wall turbulence doesn't get significantly influenced by the wall-normal permeability. Further studies by (Chandesris et al., 2013) and (Nishiyama et al., 2020) clarified on the impact of isotropic and anisotropic wall permeability on heat transfer in a TCF, respectively. In both these studies the bottom wall was made permeable while the top wall was kept impermeable. The turbulence enhancing streamwise permeability was found effective for increasing heat transfer as well. However, it is not yet clear how the wall permeability will effect the velocity and temperature field in a flow domain with multiple parallel channels, especially when the flow is laminar and developing.

In chapter 4 of this thesis we propose and explore the use of porous media as a potential passive control strategy to generate travelling wave-like wall blowing and suction. By making use of the volume penalisation method (Khadra et al., 2000), a class of immersed boundary method (Mittal and Iaccarino, 2005), we solved one set of governing equations for both the fluid and porous media. The flow inside the porous media is modeled using the Darcy's law which relates the flow rate inside the porous media to the applied pressure gradient (Nield and Bejan, 2006).

## 1.5 Objectives and layout of the thesis

The objectives from the study are mainly three. First, to perform a systematic study on the effect of traveling wave parameters of wall blowing and suction on velocity and temperature field, in both laminar and turbulent channel flows. Second, to understand the mechanism



of dissimilar heat transfer enhancement. And finally to identifying a passive mechanism to generate traveling wave-like blowing and suction.

Including the current chapter, the thesis consists of five chapters. In chapter 2, we present the results from a series of DNSs of heat and momentum transfer in a fully developed LCF subjected to a traveling wave-like wall blowing and suction. By systematically changing the wavelength  $\lambda_x$  and the phase speed  $U_p$  of a traveling wave, their impacts on the skin friction coefficient  $C_f$ , the Stanton number  $St$ , and their ratio,  $A = 2St/C_f$ , named the analogy factor, are evaluated at different Reynolds numbers. Significant dissimilar heat transfer enhancement is confirmed for  $U_p > 0$ . It is also found that such a control input remains advantageous even when the power consumption for applying the control input is taken into consideration. In order to analyze the dissimilar responses of the velocity and thermal fields to the applied control input, we introduce the influential layer thickness and the magnitude, of the Reynolds shear stress and the convective heat flux. It is shown that the influential layer thicknesses for the velocity and thermal fields are kept relatively similar for fast traveling waves, and can be well correlated with the Stokes layer thickness determined by the temporal period of the wave and the fluid viscosity. In contrast, a significant difference in their magnitudes is confirmed. Phase and budget analyses of the coherent velocity and thermal fluctuations reveal that the continuity constrain on the velocity field is the primary reason for dissimilar heat transfer enhancement.

Chapter 3 acts as an extension of Chapter 2 and discusses the results from the DNSs of a fully developed TCF to clarify the effects of travelling wave-like wall blowing and suction on dissimilar heat transfer enhancement. A parametric study is performed by systematically changing  $\lambda_x$  and  $U_p$  of the traveling wave. The instantaneous velocity and thermal fields are decomposed into coherent and random components, unlike the case of LCF where there exists only the coherent component. Then, the contribution from each component to dissimilar heat transfer enhancement is evaluated separately. It is found that the random component makes a dominant contribution to dissimilarity, and this can be explained by an indirect effect through the modification of the coherent field by the applied control. Based on the above mechanisms, we propose a simple unsteady Reynolds-averaged Navier–Stokes (URANS) approach, where the phase-averaged velocity and thermal fields are solved directly whereas the effects of the random component are modelled by the Boussinesq eddy viscosity and diffusivity hypothesis. It is shown that the present URANS can capture the overall trend of dissimilar heat transfer enhancement in a wide parameter range of  $\lambda_x$  and  $U_p$ . In analogy with LCF, the impact of continuity constraint on the generation of dissimilarity is confirmed from both the phase and budget analyses.

In chapter 4 we propose and explore the use of porous media as a passive means to generate a travelling wave-like wall blowing and suction. Since it is important to induce a travelling wave from the leading edge of the channel for effective heat transfer enhancement, a source of disturbance is introduced upstream of the porous media. It is found that by fine tuning the porous and geometric parameters, dissimilar heat transfer enhancement can be achieved using porous media.

Finally, the thesis is summarised in chapter 4 followed by the appendix sections.

# Chapter 2

## Laminar channel flow

### 2.1 Numerical Methods and Conditions

#### 2.1.1 Governing equations

The present study deals with a fully developed laminar flow between two parallel plates. The schematic of the computational domain is shown in figure 2.1. The fluid is assumed to be incompressible and Newtonian. We also assume that the changes of physical properties due to the temperature change are negligible, so that the temperature can be treated as passive scalar. Throughout the present study, the velocity and thermal fields are assumed to be two-dimensional. Hence, the governing equations for the velocity and thermal fields are the following Navier-Stokes, continuity and energy equations:

$$\frac{\partial u_i}{\partial t} + \frac{\partial (u_j u_i)}{\partial x_j} = -\frac{\partial p}{\partial x_i} + \frac{1}{Re} \frac{\partial^2 u_i}{\partial x_j \partial x_j}, \quad (2.1)$$

$$\frac{\partial u_i}{\partial x_i} = 0, \quad (2.2)$$

$$\frac{\partial \theta}{\partial t} + \frac{\partial (u_j \theta)}{\partial x_j} = \frac{1}{RePr} \frac{\partial^2 \theta}{\partial x_j \partial x_j} + Q, \quad (2.3)$$

where,  $u_i = (u, v)$  represent the velocity components in the streamwise and wall-normal directions  $x_i = (x, y)$ . And,  $p, t, \theta$ , and  $Q$  denote static pressure, time, temperature, and heat source, respectively. Throughout this thesis, a dimensional quantity will be denoted with a superscript of an asterisk, while a dimensionless quantity is expressed without a superscript. The half-channel height,  $\delta^*$ , the bulk mean velocity,  $U_b^*$ , and the bulk mean temperature,  $\theta_b^*$ ,

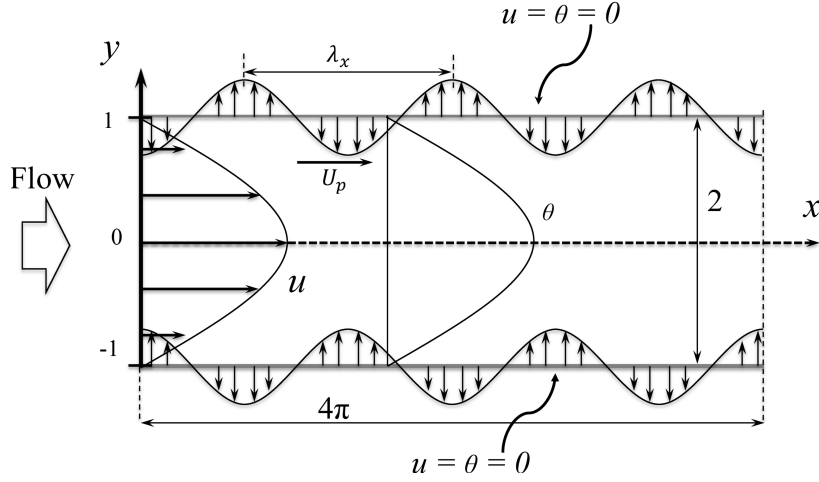


Figure 2.1 Schematic of the flow domain and the coordinate systems.

are used for non-dimensionalization. Based on Hasegawa and Kasagi (2011); Yamamoto et al. (2013), both  $U_b^*$  and  $\theta_b^*$  are defined based on their volume average as

$$U_b^* = \frac{1}{2\delta^*} \int_{-\delta^*}^{\delta^*} \bar{u}^* dy, \quad (2.4)$$

$$\theta_b^* = \frac{1}{2\delta^*} \int_{-\delta^*}^{\delta^*} \bar{\theta}^* dy. \quad (2.5)$$

The Reynolds number  $Re$  and the Prandtl number  $Pr$  are defined as  $Re = U_b^* \delta^* / \nu^*$  and  $Pr = \nu^* / \alpha^*$ , where  $\nu^*$  and  $\alpha^*$  represent the kinematic viscosity and the thermal diffusivity of the fluid, respectively.

Following previous studies (Hasegawa and Kasagi, 2011; Yamamoto et al., 2013), the governing equations for  $u$  and  $\theta$  are made similar by setting  $Q = -\partial \bar{p} / \partial x$  and  $Pr = 1$ . The over-bar represents averaging along homogeneous direction  $x$ , and time  $t$ . The boundary conditions for  $u$  and  $\theta$  are also made similar by setting  $u = \theta = 0$  on both the walls. Under such an ideal situation, both the governing equations and boundary conditions for  $u$  and  $\theta$  become similar, so that it can be considered as the most difficult case to achieve dissimilarity. Even in this case, however, dissimilar heat transfer enhancement is possible due to the continuity constraint on the velocity field as will be shown later. Hence, the present condition is suitable to clarify the fundamental difference between the divergence-free fluid vector and the conservative scalar.

	$\phi_{rms}$	$\lambda_x$	$U_p$	$Re$	$Pr$
Min et al. (2006)	0.11	$\pi \sim 4\pi$	$-6.0 \sim 2.25$	1333.33	–
Mamori et al. (2010)	0.11	$2\pi/5 \sim 200\pi$	$-7.5 \sim 7.5$	1333.33	–
Higashi et al. (2011)	0.11	$\pi \sim 4\pi$	$-9.0 \sim 9.0$	1333.33	1.0
present study	0.11	$2\pi/5 \sim 4\pi$	$-3.0 \sim 3.0$	10, 100, & 500	1.0

Table 2.1 Comparison of the present traveling wave parameters with those used by Min et al. (2006), Mamori et al. (2010), and Higashi et al. (2011).

### 2.1.2 Control input

As discussed in chapter 1 and shown in figure 2.1, the sinusoidal traveling wave-like wall normal control input takes the form:

$$v_w = \phi \sin \left\{ \frac{2\pi}{\lambda_x} (x - U_p t) \right\}, \quad (2.6)$$

where,  $\phi$ ,  $\lambda_x$ , and  $U_p$  are the amplitude, wavelength, and phase speed of the traveling wave, respectively. A subscript of  $w$  indicates a quantity on the bottom wall. In the previous studies (Hasegawa and Kasagi, 2011; Yamamoto et al., 2013), it has been reported that applying a traveling wave in a varicose mode at the top and bottom walls is most effective for dissimilar heat transfer enhancement and has been found true for the present setup as well (see appendix B.1 for more detailed results). Accordingly, the present control input at the top wall is given by the same formula but with opposite sign. This makes the controlled flow statistically symmetric about the channel center. Therefore, without loss of generality, the following discussions in this chapter focus on only the bottom half of the channel.

Table 2.1 summarizes the parameter ranges of the traveling wave, i.e.,  $\phi_{rms}$ ,  $\lambda_x$ , and  $U_p$  considered in the present study and comparison with those considered in previous studies (Higashi et al., 2011; Mamori et al., 2010; Min et al., 2006). Here,  $\phi_{rms}$  represents the root-mean-square value of the magnitude of the traveling wave normalized by the bulk mean velocity. As will be shown later, the optimal combination of  $\lambda_x$ , and  $U_p$  can be identified within the current parameter ranges.

### 2.1.3 Numerical method

The governing equations are numerically solved by a pseudo spectral method. The present code has been verified and successfully applied to control and estimation problems in fully developed turbulent channel flows (Hasegawa and Kasagi, 2011; Suzuki and Hasegawa, 2017). For temporal discretization, the second-order Adams-Bashforth and Crank-Nicolson methods are used for the convection and diffusion terms, respectively. The dimensions of the computational domain in the streamwise and wall-normal directions are set to be  $(L_x, L_y) = (4\pi, 2.0)$  as shown in figure 2.1. The numbers of Fourier modes and Chebyshev polynomials in the  $(x, y)$  directions are  $(N_x, N_y) = (64, 65)$ , respectively. Since 3/2-rule is applied to remove an aliasing error, the numbers of grid points in the physical space are  $(M_x, M_y) = (96, 97)$ . Consequently, there are approximately 6 Fourier modes (or 9 physical grid points) to cover the smallest wavelength, *i.e.*  $\lambda_x = 2\pi/5$ , considered in the present study. We have conducted an additional grid convergence study to verify the present grid resolution. The results of the grid convergence test is summarized in appendix A.1.

In the present study, three different Reynolds numbers  $Re = 10, 100$ , and  $500$  are considered as listed in Table 2.1. All simulations were started from a parabolic velocity profile under a constant flow rate condition without any initial perturbations. After applying a control, each simulation was run for a sufficiently long period, so that both velocity and thermal fields reach a fully developed state. Afterwards, all statistics were obtained. It should be noted that, in all the cases considered, the induced velocity and thermal fields are coherent to the control input. This means the velocity and thermal fields becomes steady in the frame moving with the phase speed of an applied traveling wave. The coherent velocity and thermal fields induced by the traveling wave will be analyzed in detail in §2.3.

### 2.1.4 Performance indices

The pressure drop and heat transfer characteristics are evaluated by the skin-friction coefficient  $C_f$  and the Stanton number  $St$ , which are respectively defined as

$$C_f = \frac{\tau_w^*}{\rho^* U_b^{*2}/2} = \frac{2}{Re} \left( \frac{d\bar{u}}{dy} \right)_w, \quad (2.7)$$

$$St = \frac{q_w^*}{\rho^* C_p^* U_b^* \Theta_b^*} = \frac{1}{Re Pr} \left( \frac{d\bar{\theta}}{dy} \right)_w. \quad (2.8)$$

Here  $\tau_w^*$ ,  $\rho^*$ ,  $q_w^*$ , and  $C_p^*$  are the wall shear stress, the fluid density, the wall heat flux, and the specific heat of the fluid, respectively. Accordingly, the analogy factor  $A$  is defined as the ratio of the above two quantities:

$$A \equiv \frac{2St}{C_f} = \left( \frac{d\bar{\theta}}{dy} \right)_w \left( \frac{d\bar{u}}{dy} \right)_w^{-1}. \quad (2.9)$$

For the present uncontrolled flow,  $A$  becomes exactly unity since  $C_{f0} = 2St_0 = 6/Re$ , where the subscript of 0 indicates an uncontrolled flow value. The aim of the present study is to increase  $A$  above unity.

The power consumption in an uncontrolled flow is solely determined by the pumping power  $P_p^*$  per unit area required to drive the flow, so that it is proportional to the wall friction, i.e.,  $P_p^* = U_b^* \tau_w^*$ . In a controlled case, however, additional power consumption  $\Pi_{net}^*$  for applying a control should also be taken into account:

$$\Pi_{net}^* = \overline{\left( p_w^* v_w^* + \frac{1}{2} \rho^* v_w^{*3} \right)}, \quad (2.10)$$

where the first and second terms account for pressure work and the kinetic energy of the control input, respectively. Although the above power consumption is exact, it can be negative locally in space and time. Since the energy recovery from the fluid to an actuator is unrealistic, we also introduce more conservative measure for evaluating power consumption for control as follows:

$$\Pi_{csv}^* = \overline{\left( S_1 p_w^* v_w^* + \frac{1}{2} S_2 \rho^* v_w^{*3} \right)}, \quad (2.11)$$

where  $S_1$  and  $S_2$  are switching functions and defined so that only positive power consumption is integrated, while negative power consumption is discarded. Namely,

$$S_1 = \begin{cases} 1 & (p_w^* v_w^* > 0) \\ 0 & (p_w^* v_w^* \leq 0), \end{cases} \quad S_2 = \begin{cases} 1 & (v_w^* > 0) \\ 0 & (v_w^* \leq 0). \end{cases} \quad (2.12)$$

Then, the total power consumption is given by  $P_{net}^* = P_p^* + \Pi_{net}^*$  or  $P_{csv}^* = P_p^* + \Pi_{csv}^*$ . Accordingly, the effective wall shear stresses based on the total power consumption can be defined as  $\tau_{w_{net}}^* = P_{net}^*/U_b^*$  and  $\tau_{w_{csv}}^* = P_{csv}^*/U_b^*$ , respectively. The corresponding skin-friction coefficients are

$$C_{f_{net}} = \frac{\tau_{w_{net}}^*}{\rho^* U_b^{*2}/2}, \quad C_{f_{csv}} = \frac{\tau_{w_{csv}}^*}{\rho^* U_b^{*2}/2}. \quad (2.13)$$

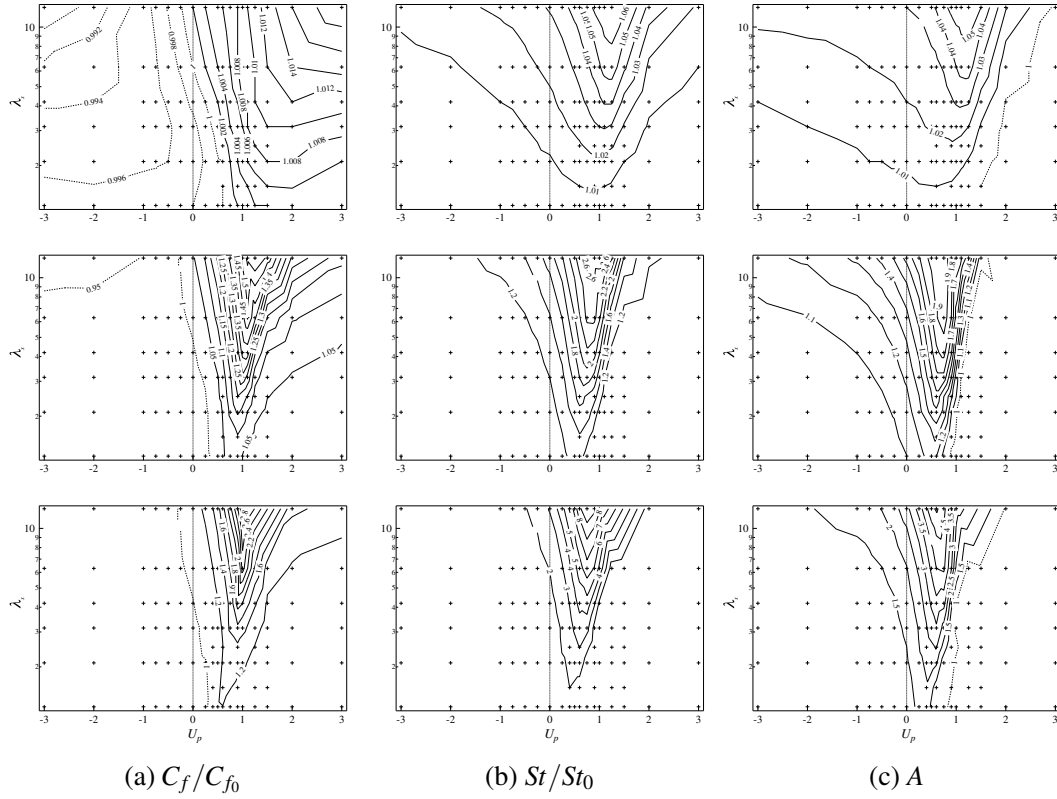


Figure 2.2 Contours of  $C_f/C_{f_0}$ ,  $St/St_0$ , and  $A$  as a function of  $(\lambda_x, U_p)$ :  $Re = 10$  (top row),  $Re = 100$  (middle row),  $Re = 500$  (bottom row). Contours with a value less than or equal to one are shown using dashed lines.

Finally, in analogy with the definition equation (2.9) of  $A$ , we can define  $A_{net}$  and  $A_{csv}$  as follows

$$A_{net} = \frac{2St}{C_{f_{net}}}, \quad A_{csv} = \frac{2St}{C_{f_{csv}}}. \quad (2.14)$$

Consequently,  $A_{net}$  and  $A_{csv}$  can be considered as the overall efficiencies taking into considerations of the energy expenditure for applying a control.

## 2.2 Control performance

### 2.2.1 Comparison of the performance indices for $Re = 10, 100$ , and $500$

The contour plots of  $C_f/C_{f_0}$ ,  $St/St_0$ , and  $A$  in the  $\lambda_x - U_p$  plane for the three Reynolds numbers considered are shown in figure 2.2. The general trends of the performance indices,



i.e.,  $C_f/C_{f0}$ ,  $St/St_0$ , and  $A$  remain similar as  $Re$  increases from 10 to 500. Both  $C_f/C_{f0}$  and  $St/St_0$  have their maximum between  $0 < U_p < 1.5$ . This can be explained by the presence of the critical layer (Maslowe, 1986), where the responses of the velocity and thermal fields are amplified due to the coincidence of the local mean velocity and the phase speed of an applied control input. Accordingly, V-shaped contours of  $C_f/C_{f0}$  and  $St/St_0$  can be confirmed. It should be emphasized, however, that they are not enhanced in a similar manner. Rather,  $St/St_0$  tends to be enhanced more than  $C_f/C_{f0}$ . As a result, the maximum of  $A$  is observed around  $U_p \approx 0.75$  for a given  $\lambda_x$ . We also note that both  $C_f/C_{f0}$  and  $St/St_0$  are enhanced with increasing  $\lambda_x$ , and so is  $A$  within the range considered here.

As reported by the previous studies (Mamori et al., 2010; Min et al., 2006; Woodcock et al., 2012), realization of sub-laminar drag ( $C_f/C_{f0} < 1$ ) with an UTW can be confirmed for all the three Reynolds numbers considered. This is due to the pumping effect (Hoepffner and Fukagata, 2009) in which a net mass flux is generated in the direction opposite to the applied travelling wave, and thus contributes to reduce pumping power to achieve a certain flow rate. Meanwhile,  $St/St_0$  is commonly increased above unity with an UTW. Consequently, as reported by Higashi et al. (2011), simultaneous drag reduction and heat transfer enhancement, i.e.,  $C_f/C_{f0} < 1$  and  $St/St_0 > 1$ , can be confirmed in a wide range of UTWs. It should be emphasized, however, that the peak of  $A$  appears for a DTW with the phase speed of  $U_p \approx 0.75$ . Indeed, as will be shown later, UTW is no longer effective when the power consumption for applying the control is taken into account.

For  $Re = 10$ , due to its viscous-dominated flow, there is no substantial variations in the performance indices with respect to their uncontrolled flow values. On the contrary,  $C_f$ ,  $St$ , and  $A$  are significantly enhanced for  $Re = 100$  and 500. Since the qualitative features of the performance indices for  $Re = 100$  and 500 remain similar,  $Re = 100$  will be considered as the reference Reynolds number for further analyses in the following sections.

### 2.2.2 Effects of control power input on performance indices at $Re = 100$

The contour plots of  $\Pi_{net}$  and  $\Pi_{csv}$  at  $Re = 100$  are shown in figure 2.3a and 2.3b, respectively. From figure 2.3a, it is found that  $\Pi_{net}$  is negative for DTWs with  $0 < U_p < 1.5$ . This suggests that, at least theoretically, it is possible to recover energy from the flow field when a DTW is applied. Meanwhile,  $\Pi_{net}$  is always positive for UTWs. We can also confirm that  $\Pi_{csv}$  is always positive by its conservative definition, refer equation (2.11), as shown in figure 2.3b.

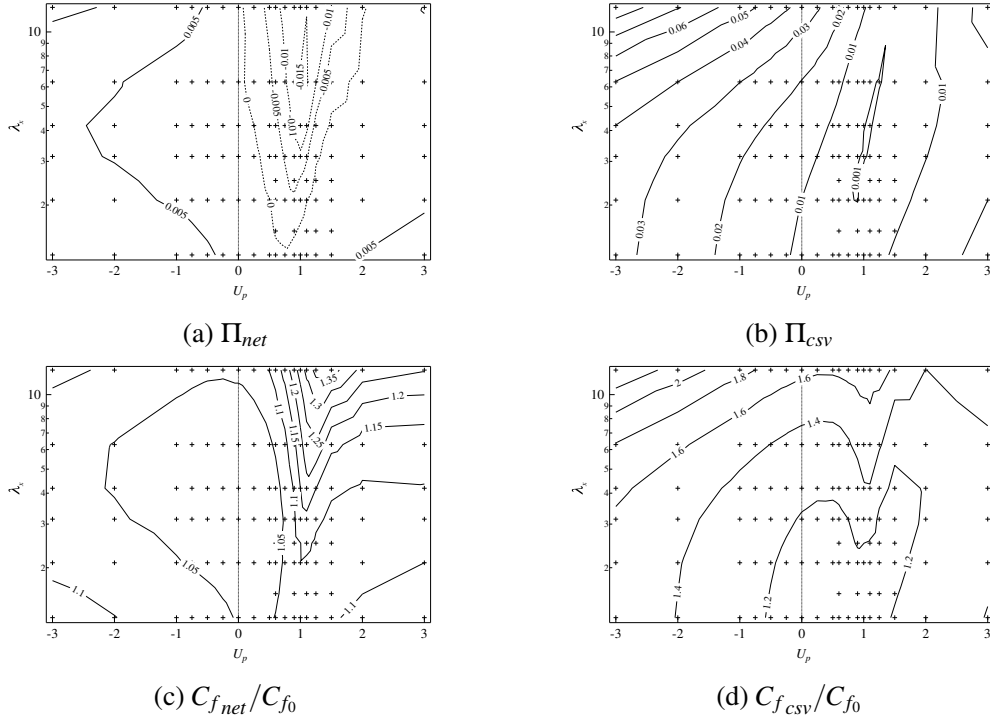


Figure 2.3 Contour plots of  $\Pi_{net}$ ,  $\Pi_{csv}$ ,  $C_{f_{net}}/C_{f_0}$ , and  $C_{f_{csv}}/C_{f_0}$  as a function of  $(\lambda_x, U_p)$  for  $Re = 100$ . In figure 2.3a, contours with a value less than or equal to zero are shown using dashed lines.

The corresponding contours of  $C_{f_{net}}/C_{f_0}$  and  $C_{f_{csv}}/C_{f_0}$  are plotted in figure 2.3c and 2.3d. First, it can be seen from figure 2.3c that  $C_{f_{net}}/C_{f_0}$  becomes always larger than unity when the control power input is taken into account. This is consistent to the fundamental limit proved by Bewley (2009) and Fukagata et al. (2009), indicating that it is impossible to make the total power consumption less than that needed for a uncontrolled flow under a fixed flow rate. As evident from figures 2.3a and 2.3b, there is an unique  $(\lambda_x, U_p)$  combination where  $\Pi_{net}$  or  $\Pi_{csv}$  reaches its minimum. This suggests that both  $A_{net}$  and  $A_{csv}$  could have the optimal combination of  $(\lambda_x, U_p)$ , unlike the case for  $A$ .

The contour plots of  $A_{net}$  and  $A_{csv}$  are shown in figure 2.4. It is found that dissimilar heat transfer enhancement ( $A_{net} > 1$  or  $A_{csv} > 1$ ) is achieved even when the control power input is taken into account. Another interesting observation is that UTW is no longer effective for dissimilar heat transfer enhancement as well as energy saving even for the relatively small amplitude of the control input, i.e.,  $\phi_{rms} = 0.11$ , considered in the present study. Figure 2.4b reveals that  $A_{csv}$  have the optimal combination of  $(\lambda_x, U_p) = (2\pi, 0.75)$  leading to the

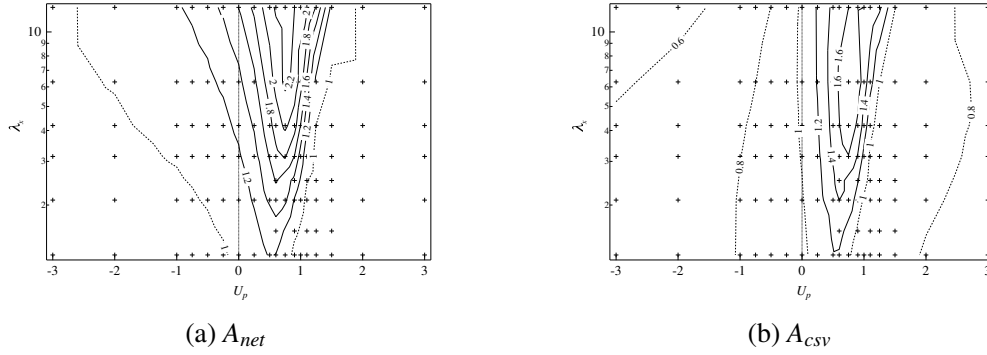


Figure 2.4 Contour plots of  $A_{net}$  and  $A_{csv}$ , as a function of  $(\lambda_x, U_p)$  for  $Re = 100$ . Contours with a value less than or equal to one are shown using dashed lines.

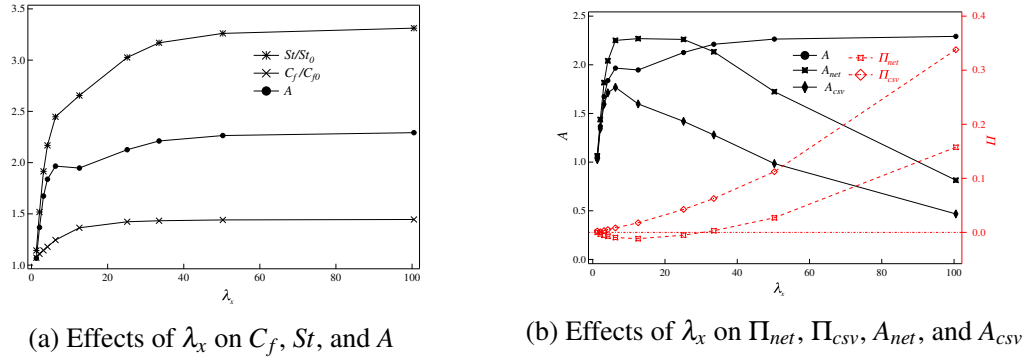


Figure 2.5 Effect of  $\lambda_x$  on the control performance for  $U_p = 0.75$  at  $Re = 100$ .

maximum value of  $A_{csv} = 1.77$ . On the other hand,  $A_{net}$  monotonically increases with  $\lambda_x$  within the current parameter range.

In order to clarify whether there exists the optimal wavelength for  $A$  and  $A_{net}$ , we carried out additional simulations for  $U_p = 0.75$  with a longer streamwise domain size of  $32\pi$ , while the grid resolution is kept unchanged. The results are shown in figure 2.5.  $C_f/C_{f0}$  and  $St/St_0$  asymptotically converge to 1.45 and 3.31, respectively. As a result, the asymptotic value of  $A$  is 2.29. Shown in figure 2.5b are the plots of  $\Pi_{net}$  and  $\Pi_{csv}$  along with those of  $A_{net}$  and  $A_{csv}$ . It is found that  $\Pi_{net}$  have its minimum at  $\lambda_x = 4\pi$ , leading to the maximum of  $A_{net}$  at  $(\lambda_x, U_p) = (4\pi, 0.75)$ . Hereafter, the combination of  $(\lambda_x, U_p) = (2\pi, 0.75)$ , which is optimal for  $A_{csv}$ , is considered as a reference point for further analyses.

### 2.2.3 Effects of the amplitude of the control input on performance indices for $Re = 100$

Although the complete parametric survey including the amplitude of the control input is out of the present scope, the effects of  $\phi_{rms}$  on  $C_f/C_{f0}$  and  $St/St_0$  for the reference point, i.e.,  $(\lambda_x, U_p) = (2\pi, 0.75)$ , is presented in figure 2.6. In previous studies (Higashi et al., 2011; Mamori et al., 2010), linear analysis has been often used to estimate the impacts of a traveling wave. Assuming the linear responses of the velocity and thermal fluctuations, it is expected that  $(C_f - C_{f0})$ ,  $(St - St_0)$ , and thus  $(2St - C_f)$  are proportional to the square of the magnitude of the control input. Meanwhile, Min et al. (2006) showed that non-linear effects become evident for  $(C_f - C_{f0})$  when the amplitude of a traveling wave is large. Hence, it is of interest how the non-linear effects appear in heat transfer.

The current results, taking into account non-linearity, shown in figure 2.6 reproduce the non-linear effects on skin friction drag reported by Min et al. (2006). Furthermore, a similar trend is also observed for heat transfer. Namely, both  $(C_f - C_{f0})$  and  $(St - St_0)$  becomes lower than those predicted in the linear regime for a large amplitude. Assuming that the data for  $\phi_{rms} = 0.01$  lies in the linear regime, the deviation of  $(2St - C_f)$  from that predicted by the linear regime increases from 15% to 70% when the  $\phi_{rms}$  increases from 0.05 to 0.30. The impacts of  $\phi_{rms}$  on various performance indices obtained in the present study are summarized in Table 2.2. It is also found that the deviation from the linear regime becomes more prominent in the order of  $(C_f - C_{f0})$ ,  $(C_{f_{net}} - C_{f0})$  and  $(C_{f_{csv}} - C_{f0})$ . Meanwhile,  $A$  monotonically increases with  $\phi_{rms}$ . We also note that the control power input should be proportional to  $\phi_{rms}^3$  in the linear regime (refer equations (2.10) and (2.11)). This dependency can be confirmed for lower amplitudes, but also start saturating for large amplitudes. As a result,  $A_{csv}$  saturates faster than  $A$  and  $A_{net}$  as  $\phi_{rms}$  increases. Considering the rapid increase of  $\Pi_{csv}$ , further increase of  $\phi_{rms}$  is not advantageous from an energetic viewpoint. Indeed,  $A_{csv}$  increases to around 2.0 with increasing  $\phi_{rms}$  up to 0.2 and then starts decreasing for a further higher  $\phi_{rms}$  (see, Table 2.2). In summary, we conclude that linear analysis provides the upper limit of the performance on dissimilar heat transfer. With increase in  $\phi_{rms}$ , however, the deviation from linear regime becomes more pronounced, and therefore non-linear analysis is necessary for quantitative evaluations of the control effects.

$\phi_{rms}$	$C_f/C_{f_0}$	$C_{f_{net}}/C_{f_0}$	$C_{f_{csv}}/C_{f_0}$	$\Pi_{net} \times 10^2$	$\Pi_{csv} \times 10^2$	$St/St_0$	$(2St - C_f)$	$A$	$A_{net}$	$A_{csv}$
0.01	1.00	1.00	1.00	-0.01	0.01	1.02	0.00	1.02	1.02	1.02
0.05	1.07	1.03	1.10	-0.29	0.15	1.44	0.02	1.34	1.41	1.31
0.11	1.24	1.09	1.38	-0.95	0.83	2.45	0.07	1.97	2.25	1.77
0.15	1.39	1.14	1.70	-1.48	1.87	3.35	0.12	2.41	2.93	1.97
0.20	1.56	1.22	2.17	-2.05	3.66	4.46	0.17	2.86	3.66	2.06
0.25	1.72	1.30	2.76	-2.57	6.18	5.59	0.23	3.24	4.31	2.03
0.30	1.88	1.38	3.47	-2.99	9.53	6.75	0.29	3.59	4.89	1.95

Table 2.2 Effects of  $\phi_{rms}$  on performance indices for  $(\lambda_x, U_p) = (2\pi, 0.75)$  at  $Re = 100$ .

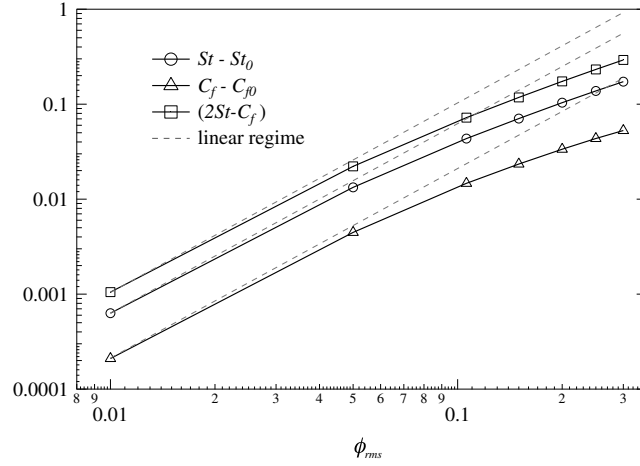


Figure 2.6 Effects of  $\phi_{rms}$  on skin friction drag and heat transfer for  $(\lambda_x, U_p) = (2\pi, 0.75)$  at  $Re = 100$ .

## 2.3 Mechanism of dissimilarity

### 2.3.1 Influential layer thickness $\delta$

Under a constant flow rate condition considered, the Fukagata-Iwamoto-Kasagi identity (FIK-identity) for  $C_f$  and its extension to  $St$  (Fukagata et al., 2002; Hasegawa and Kasagi, 2011) result in the following relationships:

$$C_f = \frac{6}{Re} + 3 \int_{-1}^1 y \overline{u'v'} dy, \quad (2.15)$$

$$2St = \frac{6}{Re} + 3 \int_{-1}^1 y \overline{\theta'v'} dy, \quad (2.16)$$

where  $\overline{yu'v'}$  and  $\overline{y\theta'v'}$  represents the  $y$ -weighted Reynolds shear stress and convective heat flux, respectively. We define the resulting dissimilarity as

$$D \equiv 2St - C_f = 3 \int_{-1}^1 y \overline{(\theta' - u')v'} dy. \quad (2.17)$$

The wall-normal distributions of  $\overline{yu'v'}$ ,  $\overline{y\theta'v'}$ , and  $\overline{y(\theta' - u')v'}$  in the bottom half of the computational domain ( $-1 < y < 0$ ) for the reference point  $(\lambda_x, U_p) = (2\pi, 0.75)$  are shown in figure 3.14. Though both  $\overline{yu'v'}$  and  $\overline{y\theta'v'}$  are prominent between  $-1 < y < -0.3$ ,  $\overline{y\theta'v'}$  is

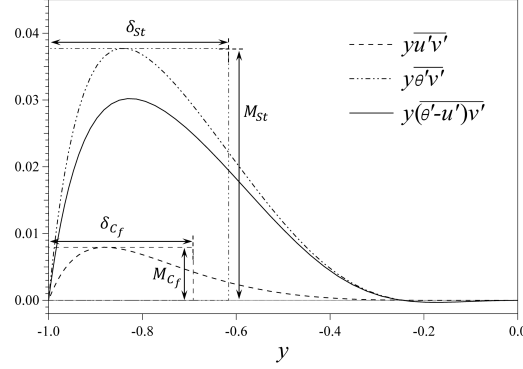


Figure 2.7 Wall-normal distributions of  $y\overline{u'v'}$ ,  $y\overline{\theta'v'}$ , and  $y(\overline{\theta' - u'})v'$  for  $(\lambda_x, U_p) = (2\pi, 0.75)$  at  $Re = 100$ .

more significant than  $y\overline{u'v'}$ . This explains the large positive dissimilarity generated for the reference point.

In figure 3.14, the profiles of  $y\overline{u'v'}$  and  $y\overline{\theta'v'}$  are characterized by a near-wall layer in which the Reynolds shear stress and the convective heat flux are induced by the wall input, and also their magnitudes. This motivates us to introduce the influential layer thickness  $\delta$  and the magnitude  $M$  as schematically shown in figure 3.14:

$$\int_{-1}^0 y\overline{u'v'} dy = \delta_{C_f} \times M_{C_f}, \quad (2.18)$$

$$\int_{-1}^0 y\overline{\theta'v'} dy = \delta_{St} \times M_{St}. \quad (2.19)$$

Here,  $M_{C_f}$  and  $M_{St}$  are the peak values of  $y\overline{u'v'}$  and  $y\overline{\theta'v'}$ , respectively, while  $\delta_{C_f}$  and  $\delta_{St}$  are determined so as to satisfy equations (2.18) and (2.19). Note that  $\delta_{C_f}$  and  $\delta_{St}$  are defined to be always positive, whereas  $M_{C_f}$  and  $M_{St}$  are signed magnitudes, so that they can be positive or negative depending on the integrals on the left-hand-side. Especially, for UTWs, the Reynolds shear stress becomes negative and so is  $M_{C_f}$ . The advantage of introducing  $\delta$  and  $M$  is that it can extract the influential layer thickness and the magnitude for an arbitrary wall-normal profile of  $y\overline{u'v'}$  and  $y\overline{\theta'v'}$ , while the product of  $\delta$  and  $M$  is proportional to the increase of wall friction or wall heat flux from their uncontrolled values as shown in equations (3.10) and (3.11).

Accordingly, the ratio of the increments of  $2St$  and  $C_f$  from their uncontrolled value ( $C_{f0} = 2St_0 = 6/Re$ ) can be expressed by the product of the ratios of  $\delta$  and  $M$  as follows:

$$\frac{2St - 6/Re}{C_f - 6/Re} = \frac{\int_{-1}^1 y \overline{\theta' v'} dy}{\int_{-1}^1 y \overline{u' v'} dy} = \left( \frac{\delta_{St}}{\delta_{C_f}} \right) \left( \frac{M_{St}}{M_{C_f}} \right). \quad (2.20)$$

Therefore, a natural question is which ratio ( $\delta_{St}/\delta_{C_f}$  or  $M_{St}/M_{C_f}$ ) has a larger impact to dissimilarity, and how they are correlated with the wave properties.

As for the influential layer thickness, [Mamori et al. \(2010\)](#) reported that it can be scaled by the Stokes layer thickness, which is determined by the temporal period of a traveling wave and the fluid viscosity, i.e.,  $\sqrt{\lambda_x / (|U_p| Re)}$ . In the present study, we extend their analysis to heat transfer as well. Hence,  $\delta_{C_f}$  and  $\delta_{St}$  are both normalized by the Stokes layer thickness as

$$\delta_{C_f}^N = \delta_{C_f} \sqrt{\frac{|U_p| Re}{\lambda_x}}, \quad (2.21)$$

$$\delta_{St}^N = \delta_{St} \sqrt{\frac{|U_p| Re}{\lambda_x}}. \quad (2.22)$$

The normalized influential layer thicknesses  $\delta_{C_f}^N$  and  $\delta_{St}^N$  are plotted as a function of  $U_p$  for the reference wavelength of  $\lambda_x = 2\pi$  in figure 2.8a. It is found that both  $\delta_{C_f}^N$  and  $\delta_{St}^N$  approach to unity for fast traveling waves, i.e.,  $U_p < -1.0$  or  $U_p > 1.5$ , indicating that they can be well scaled by the Stokes layer thickness. In contrast, inside  $-1.0 < U_p < 1.5$ , the deviation from the Stokes layer becomes prominent, and there are two reasons for it. First, the Stokes layer thickness becomes infinity at  $U_p = 0$ , while  $\delta_{C_f}$  and  $\delta_{St}$  are bounded by the domain size. Second, the presence of the critical layer effects for  $0 < U_p < 1.5$  further diffuses the influential layer toward the channel center by convection. Even though both  $\delta_{C_f}^N$  and  $\delta_{St}^N$  deviate from unity, they remain comparable around the reference phase speed of  $U_p = 0.75$ . This means that the dissimilarity between  $\delta_{C_f}$  and  $\delta_{St}$  are minor. Meanwhile, significant dissimilarity between the magnitudes of  $M_{St}$  and  $M_{C_f}$  can be found for  $0 < U_p < 1.5$  as shown in figure 2.8b. More specifically, for the reference point of  $(\lambda_x, U_p) = (2\pi, 0.75)$ ,  $\delta_{St}/\delta_{C_f} = 1.25$ , whereas  $M_{St}/M_{C_f} = 9.50$ . From equation (2.20), it is evident that it is not the ratio of the influence layer thickness  $\delta_{St}/\delta_{C_f}$  but the ratio of the magnitudes  $M_{St}/M_{C_f}$  that leads to dissimilarity. We note that the above-mentioned trend can be confirmed not only for the reference wavelength, but also for all the wavelengths considered in this study.



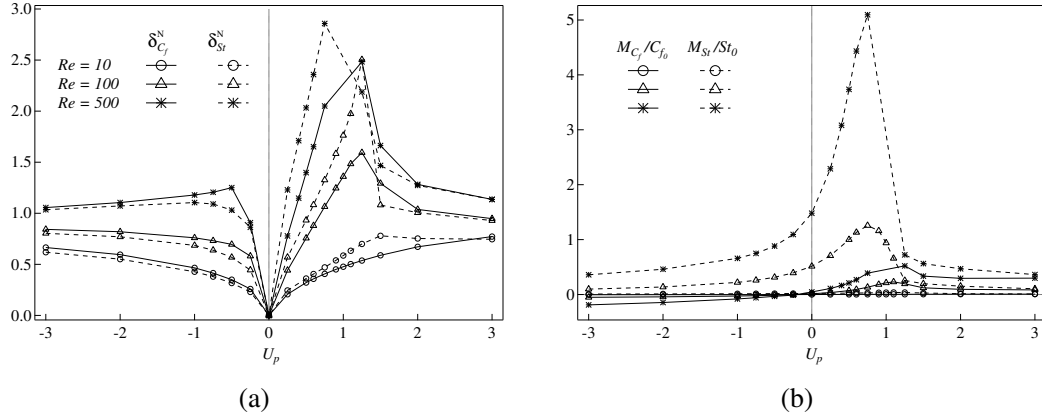


Figure 2.8 Variation of (a)  $\delta_{C_f}^N$  &  $\delta_{St}^N$  and (b)  $M_{C_f}/C_{f0}$  &  $M_{St}/St_0$  as a function of  $U_p$  for  $(\lambda_x, U_p) = (2\pi, 0.75)$  at different Reynolds numbers.

### 2.3.2 Phase analysis of velocity and thermal fields

As discussed in the end of § 2.1.3, in all the cases considered, the induced velocity and thermal fluctuations are always coherent to the applied traveling wave. Namely, all the fluctuations have the periodicity identical to  $\lambda_x$ , and move with the same velocity as the phase speed  $U_p$ . Therefore, we introduce a new coordinate  $\xi - y$  moving with the traveling wave, so that  $\xi = 0$  always corresponds to the location where the wall suction is maximum at the bottom wall. Accordingly, an arbitrary physical quantity  $f$  can be expressed in the new coordinate system as

$$f(x, y, t) = \langle f(\xi, y) \rangle, \quad (2.23)$$

where  $\langle f(\xi, y) \rangle$  is the phase-averaged quantity. The quantity  $\langle f(\xi, y) \rangle$  can be decomposed into a mean component  $\bar{f}$  and a coherent component  $\tilde{f}$ . As a result, equation (2.23) can be rewritten as

$$f(x, y, t) = \bar{f}(y) + \tilde{f}(\xi, y). \quad (2.24)$$

Shown in figure 2.9 are the contour plots of  $\tilde{\theta}$ ,  $\tilde{u}$ ,  $(\tilde{\theta} - \tilde{u})$ ,  $\tilde{v}$ ,  $\tilde{p}$ , and  $\langle y(\tilde{\theta} - \tilde{u})\tilde{v} \rangle$  in the  $\xi - y$  plane for the reference point at  $Re = 100$ . In order to explain the distribution of  $\tilde{\theta}$ , the phase-averaged velocity field  $(\langle u \rangle - U_p, \tilde{v})$  is also shown by vectors in figure 2.9a. Since the frame is moving with the applied travelling wave, the phase speed of  $U_p$  is subtracted from the phase-averaged streamwise velocity to show the relative velocity to the moving coordinate. We can find three characteristic features in the distribution of  $\tilde{\theta}$ . First, the down-welling motion due to wall suction around  $\xi = 0$  brings high-temperature fluid toward the wall resulting in positive  $\tilde{\theta}$  contours above  $\xi = 0$ . The opposite happens near the blowing regions

around  $\xi = \pm\lambda_x/2$ . Second, the wall movement at the speed of  $-U_p$  drags  $\tilde{\theta}$  upstream due to the viscous effect. Third, the convection outside the near wall region transports the temperature fluctuation  $\tilde{\theta}$  downstream.

Next, we consider  $\tilde{u}$  contours shown in figure 2.9b. Considering that the governing equations and boundary conditions are set similar for  $\tilde{\theta}$  and  $\tilde{u}$ , it is surprising that the distribution of  $\tilde{u}$  is totally different from that of  $\tilde{\theta}$ . The plot of  $(\tilde{\theta} - \tilde{u})$  shown in figure 2.9c highlights this. From figure 2.9d, it is confirmed that the coherent wall-normal velocity,  $\tilde{v}$ , is induced by wall blowing around  $\xi = \pm\lambda_x/2$  and wall suction around  $\xi = 0$ . Also, the control input creates a favourable pressure gradient around  $\xi = \pm\lambda_x/2$  and an adverse pressure gradient about  $\xi = 0$  as shown in figure 2.9e. This accelerates and decelerates only  $\tilde{u}$ , while such mechanisms are absent for the dynamics of  $\tilde{\theta}$ . Note that, in an incompressible fluid considered here, the pressure field instantaneously reacts to the velocity field so that the continuity constraint is satisfied. The present results indicate that this kinematic constrain is a primal reason for the dissimilarity between  $\tilde{\theta}$  and  $\tilde{u}$ . Finally, the contours of  $\langle y(\tilde{\theta} - \tilde{u})\tilde{v} \rangle$  are presented in figure 2.9f. This quantity is important since the integration of figure 2.9f in  $\xi$  reduces to  $y(\overline{\tilde{\theta} - \tilde{u}})\tilde{v} \equiv y(\overline{\theta' - u'})v'$  plotted in figure 3.14, and thereby represents the contribution to dissimilarity  $D$  given by equation (2.17).

One of key features in figure 2.9 is the strong negative correlation between  $(\tilde{\theta} - \tilde{u})$  and  $\tilde{v}$  near the wall (see figure 2.9c and 2.9d). Specifically, positive  $(\tilde{\theta} - \tilde{u})$  exists above the wall suction around  $\xi = 0$ . This allows to draw high temperature fluid from the wall with least momentum loss. Another characteristics is the presence of a spanwise roll which is caused by the downstream convection away from the wall and the upstream wall movement (see, the vector plot in figure 2.9a). Indeed, this secondary flow is most prominent for the reference point of  $(\lambda_x, U_p) = (2\pi, 0.75)$  considered here. The roller's height is comparable to that of channel half-height ( $l_{SR} \approx 0.70$ ), so that it contributes to mixing within the entire channel.

### 2.3.3 Budget analysis

The importance of the continuity constraint in causing dissimilarity can also be confirmed from the budget of the contribution to dissimilarity, *i.e.*,  $-(\tilde{\theta} - \tilde{u})\tilde{v}$  (refer appendix C for the

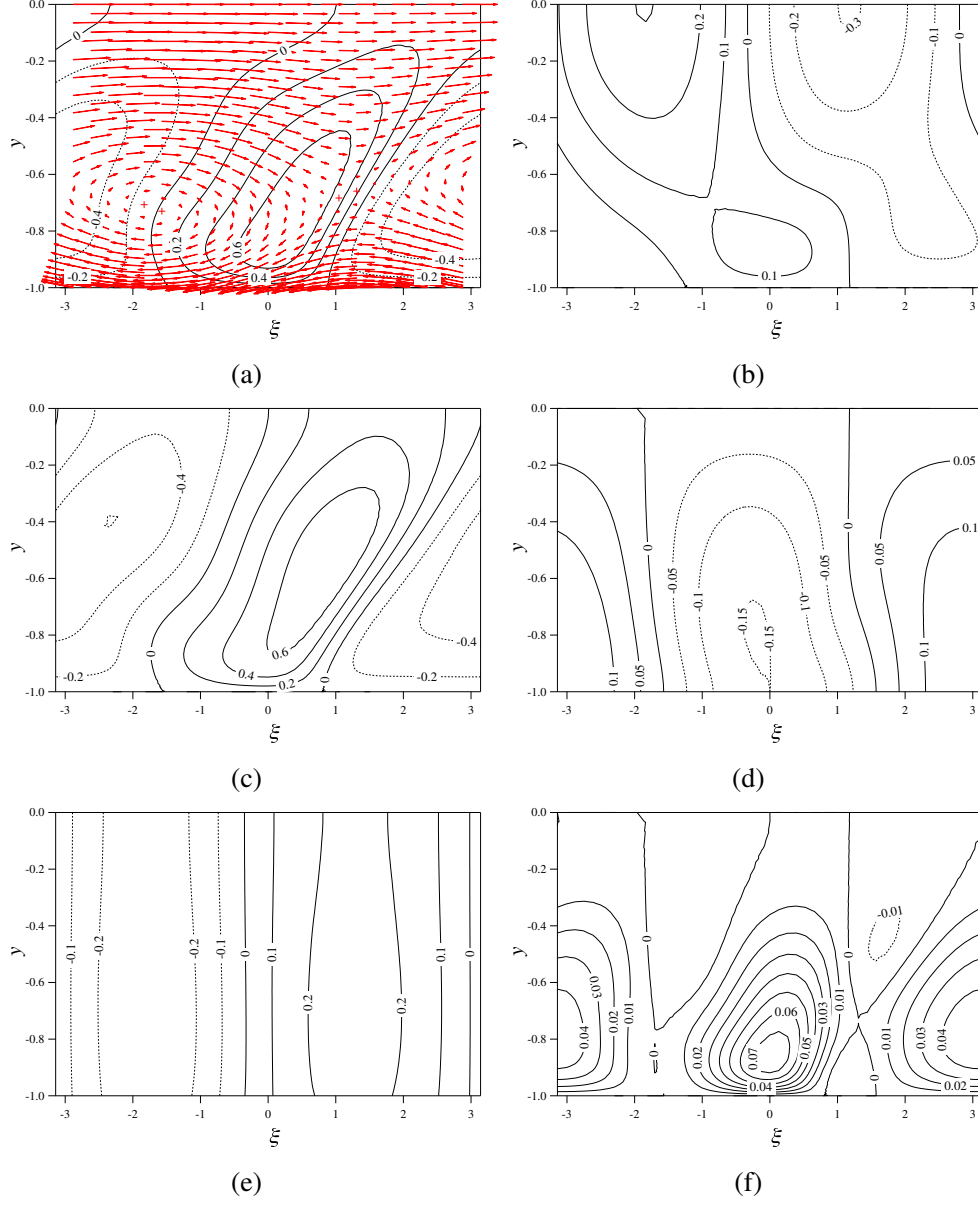


Figure 2.9 Contour plots of the coherent components: (a)  $\tilde{\theta}$ , (b)  $\tilde{u}$ , (c)  $(\tilde{\theta} - \tilde{u})$ , (d)  $\tilde{v}$ , (e)  $\tilde{p}$ , and (f)  $\langle y(\tilde{\theta} - \tilde{u})\tilde{v} \rangle$  as a function of  $(\xi, y)$  for  $(\lambda_x, U_p) = (2\pi, 0.75)$  at  $Re = 100$ . The arrows in the background of  $\tilde{\theta}$  are the vector field  $(\langle u \rangle - U_p, \tilde{v})$  scaled by a factor of 100.

detailed derivation):

$$\begin{aligned}
 0 = & \underbrace{\overline{\tilde{v}} \frac{\partial(\tilde{\theta} - \tilde{u})}{\partial y}}_{\text{production (P)}} \\
 & + \underbrace{\frac{\partial[\tilde{v}\tilde{v}(\tilde{\theta} - \tilde{u})]}{\partial y}}_{\text{turbulent diffusion (T}_D\text{)}} - \underbrace{\frac{1}{Re} \frac{\partial}{\partial y} \left[ \frac{\partial \tilde{v}(\tilde{\theta} - \tilde{u})}{\partial y} \right]}_{\text{viscous diffusion (V}_D\text{)}} \\
 & - \underbrace{\left[ -(\tilde{\theta} - \tilde{u}) \frac{\partial \tilde{p}}{\partial y} + \tilde{v} \frac{\partial \tilde{p}}{\partial x} \right]}_{\text{pressure-velocity-temperature correlation (}\Pi\text{)}} \\
 & + \underbrace{\frac{2}{Re} \frac{\partial \tilde{v}}{\partial x_j} \frac{\partial(\tilde{\theta} - \tilde{u})}{\partial x_j}}_{\text{dissipation (}\varepsilon\text{)}}. \tag{2.25}
 \end{aligned}$$

Each term in the budget equation is plotted in figure 2.10. Note that the integral of the turbulent diffusion  $T_D$  within the entire domain is exactly zero, while that of the viscous diffusion  $V_D$  is non-zero, since the viscous flux from the wall is non-zero in a controlled flow. Nonetheless,  $V_D$  is mostly negative, so that it does not contribute to dissimilar heat transfer enhancement. It is evident from figure 2.10 that the pressure-velocity-temperature correlation  $\Pi$  is the only dominant positive term in the region of  $-0.9 \lesssim y \lesssim -0.4$ . Indeed, this region agrees well with the region where  $y(\overline{\theta' - u'})\overline{v'}$  has a large positive value (see figure 3.14). As can be seen in equation (3.18),  $\Pi$  includes two terms. Among them, the second term is found to be dominant. This is clearly seen from the contour plot of  $\Pi$  and its two components shown in figure 2.11, where large positive values can be confirmed where the wall-normal velocity  $\tilde{v}$  and the streamwise pressure gradient  $\partial \tilde{p} / \partial x$  are negatively correlated (see also figure 2.9d and 2.9e). Again, the present budget analysis indicates that the streamwise pressure gradient induced by the continuity constrain on the velocity field, is a key for dissimilar heat transfer enhancement.

## 2.4 Conclusions

We carried out a series of direct numerical simulations of a fully developed laminar channel flow (LCF) subject to a traveling-wave like wall blowing and suction. By systematically

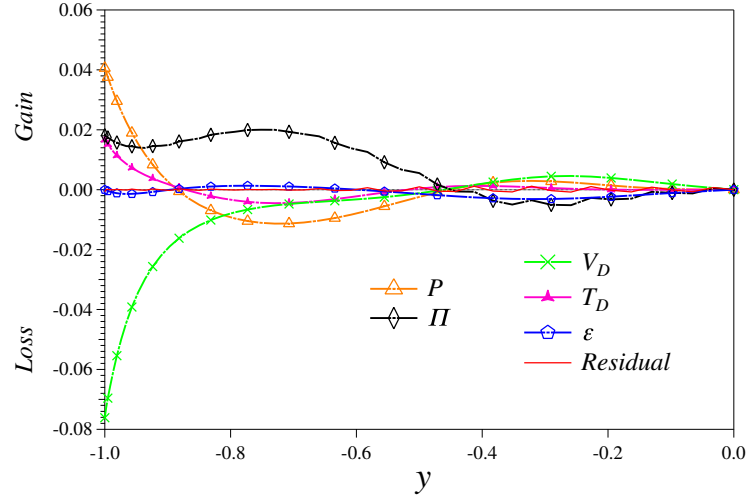


Figure 2.10 Terms in the budget equation of  $-(\theta' - u')v'$ :  $P$  = production;  $T_D$  &  $V_D$  = turbulent and molecular diffusion;  $\Pi$  = pressure-velocity-temperature correlation;  $\epsilon$  = molecular dissipation, for  $(\lambda_x, U_p) = (2\pi, 0.75)$  at  $Re = 100$ .

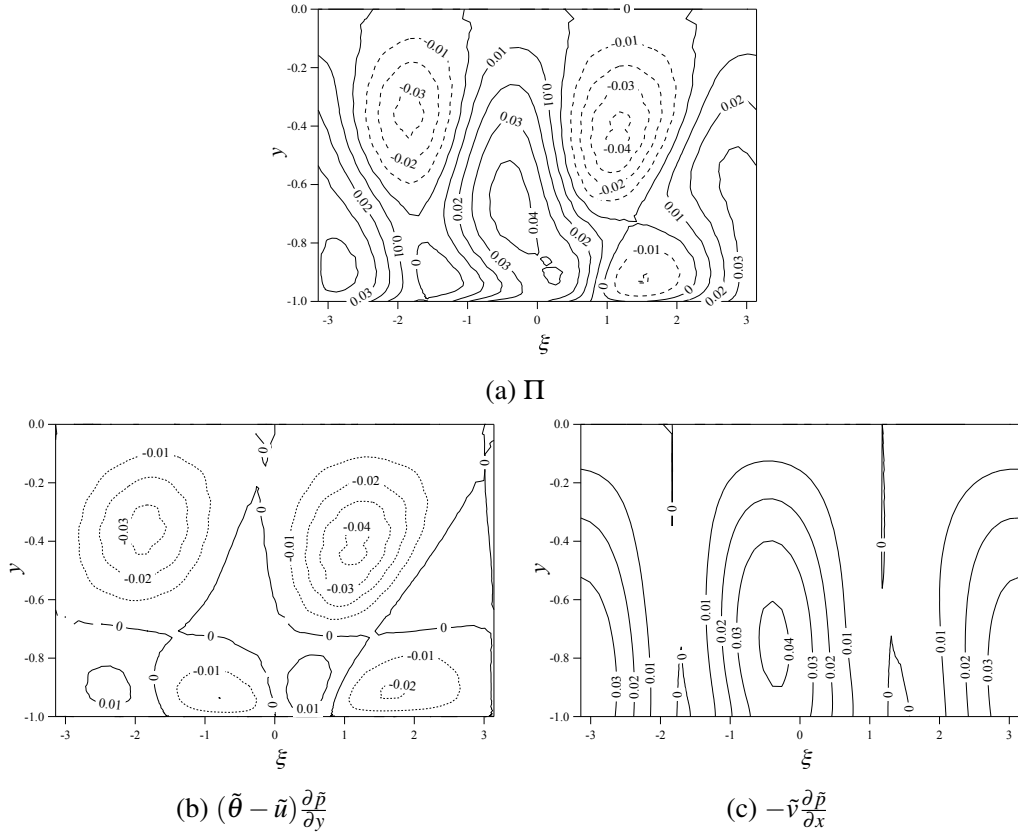


Figure 2.11 The  $\xi - y$  distribution of  $\Pi$  and its two constituent terms.

changing the phase speed  $U_p$ , the wavelength  $\lambda_x$  and the amplitude  $\phi_{rms}$  of a traveling wave, their impacts on the skin-friction coefficient  $C_f$ , the Stanton number  $St$ , and the analogy factor  $A(= 2St/C_f)$  are investigated at three different Reynolds numbers of  $Re = 10, 100$ , and  $500$ .

It is found that both  $C_f$  and  $St$  are enhanced substantially with downstream traveling waves (DTWs) with  $0 < U_p < 1.5$  due to the critical layer effect, in which the velocity and thermal fluctuations are amplified at a certain distance from the wall where the local mean velocity matches with the phase speed of an applied traveling wave. In addition, the enhancement of  $St$  is generally larger than that of  $C_f$ , so that the resultant analogy factor  $A$  becomes larger than unity. As reported in previous studies (Higashi et al., 2011), drag reduction and heat transfer enhancement are simultaneously achieved for a wide range of upstream traveling waves (UTWs) with  $U_p < 0$ . Due to the theoretical limit (Bewley, 2009; Fukagata et al., 2009), however, UTWs do not yield net energy saving for achieving a given flow rate. In contrast, DTWs remain effective for dissimilar heat transfer even when the power input for applying the control is taken into account. The present results also indicate that dissimilar heat transfer enhancement is most pronounced when the phase speed is around 75% of the bulk mean velocity and the wavelength is around three times the channel height. Comparison of the analogy factor performance from the present control input with that of the existing works, shown in figure 2.12 and 2.13, indicates the ability of the traveling-wave like wall blowing and suction as an effective control strategy for designing energy efficient thermo-fluid systems.

Fukagata-Iwamoto-Kasagi identity (Fukagata et al., 2002) for  $C_f$  and its extension to  $St$  (Hasegawa and Kasagi, 2011) show that the dissimilarity is caused by the difference in the Reynolds shear stress and the convective heat flux weighted by the distance from the channel center. For ease of analysis, we further decompose the weighted Reynolds shear stress and the weighted convective heat flux into the influential layer thickness ( $\delta_{C_f}$  and  $\delta_{St}$ ) and the magnitude ( $M_{C_f}$  and  $M_{St}$ ), respectively. It is found that both the influential layer thicknesses  $\delta_{C_f}$  and  $\delta_{St}$  for momentum and heat transfer are well correlated with the Stokes layer thickness for fast traveling waves, *i.e.*,  $U_p < -1.0$  or  $U_p > 1.5$ . For the optimal traveling wave at  $U_p = 0.75$ ,  $\delta_{C_f}$  and  $\delta_{St}$  are both larger than the Stokes layer thickness, but still their ratio remains close to unity, *i.e.*,  $\delta_{St}/\delta_{C_f} \sim 1$ . On the other hand, the ratio of their magnitudes,  $M_{St}/M_{C_f}$ , becomes as high as 10. This indicates that the larger thermal response within the influential layer thickness causes the dissimilarity.

In order to further discuss the mechanisms of the dissimilarity, phase analysis of the coherent velocity and thermal fields are conducted. It is shown that even though the govern-

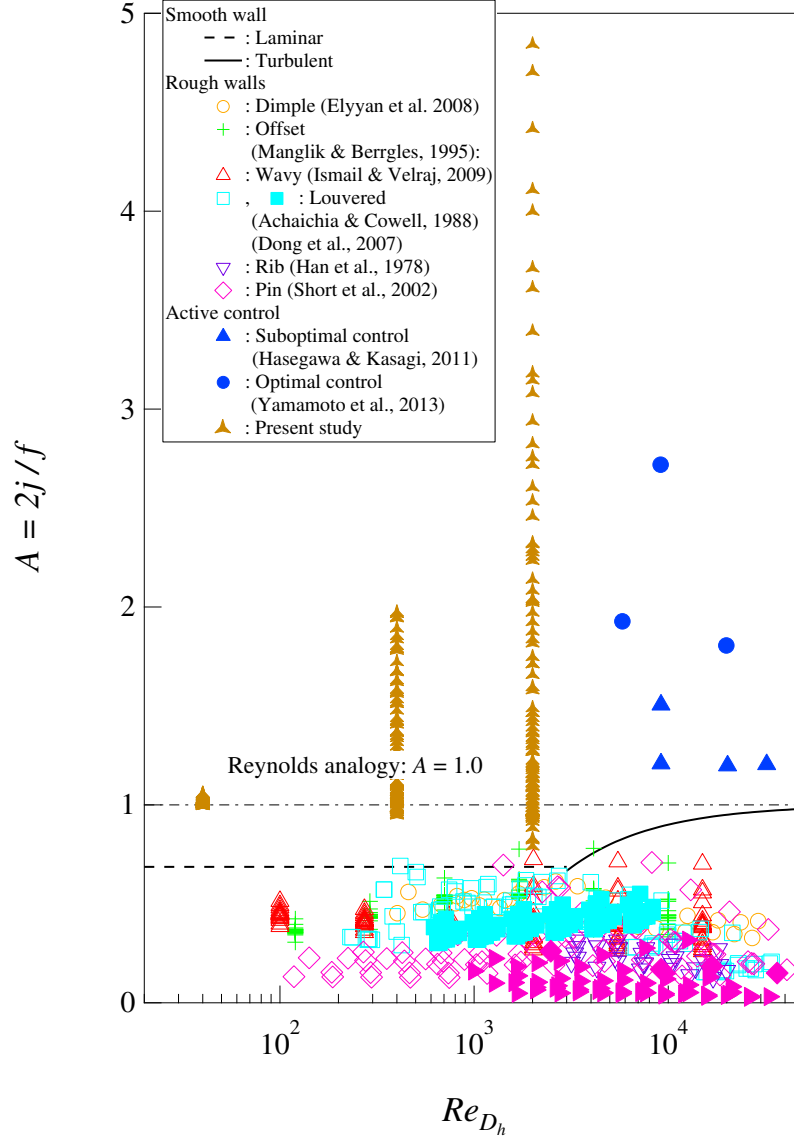


Figure 2.12 Analogy factor  $A$  as a function of  $Re_{D_h}$  for different heat transfer surfaces. The figure is same as that shown in 1.1 but with the data points included from the present study. Here  $Re_{D_h}$  is the Reynolds number based on the hydraulic diameter  $D_h$  which for a plain channel is given by  $D_h = 4\delta$ , where  $\delta$  is the half channel height. For laminar regime (dashed line), *i.e.*  $Re_{D_h} < 3000$ , a constant heat flux condition is assumed resulting in a constant value for  $A = 0.69$ . For the turbulent regime (solid line)  $C_f = 0.087Re_{D_h}^{-1/4}$  (Dean, 1978) and  $j = 0.024Re_{D_h}^{-1/5}Pr^{1/6}$  (Keys et al., 2005). For both laminar and turbulent regime  $Pr$  is set equal to one.

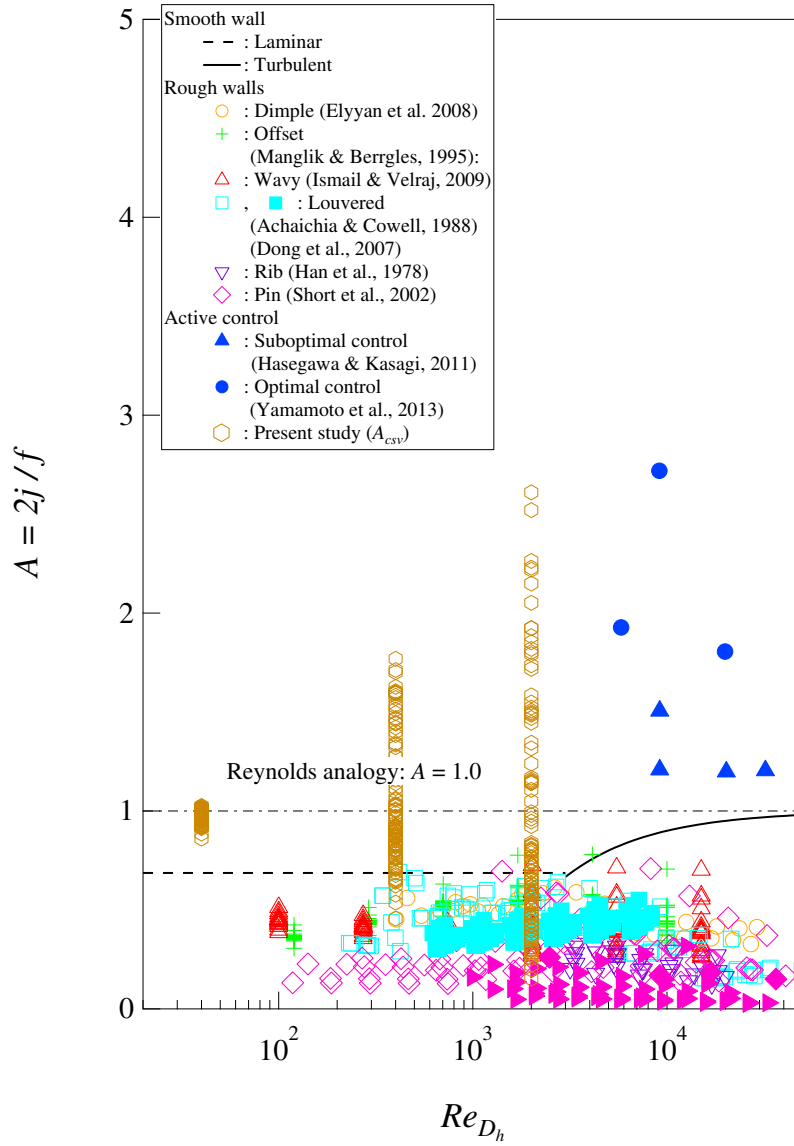


Figure 2.13 Same plot as in figure 2.12, except that  $A_{csv}$  is plotted instead of  $A$  from the present study.



ing equations and the boundary conditions for the streamwise velocity component and the temperature are made similar, their responses to an applied traveling wave are essentially different. Specifically, a pressure gradient induced by the wall input accelerates and decelerates only the streamwise velocity component, while the temperature is unaffected. The induced dissimilarity between the velocity and thermal fields is then carried by the spanwise roll, created near the wall, to result in strong dissimilarity between the wall heat flux and the skin friction. The budget of the difference between the Reynolds shear stress and the convective heat flux also supports the above observation. Namely, the correlation between the wall-normal velocity and the streamwise pressure gradient induced by the wall input is the dominant mechanisms of causing the dissimilarity. The results of the phase and budget analyses indicate that the continuity constraint on the velocity field and the resultant pressure fluctuation is the source of the dissimilarity.



# Chapter 3

## Turbulent channel flow

### 3.1 Numerical Methods and Conditions

#### 3.1.1 Governing equations

We consider a fully developed turbulent flow between two parallel plates. The schematic of the computational domain and the Cartesian coordinate system are shown in figure 3.1. The streamwise, wall-normal and spanwise directions are denoted by  $(x_1, x_2, x_3) = (x, y, z)$ , respectively, whereas the origin is located at the channel center. The corresponding velocity components are denoted by  $(u_1, u_2, u_3) = (u, v, w)$ . Like in the case of LCF discussed in chapter 2, we assume the fluid is incompressible, and the effects of buoyancy are negligible. Also, any changes in the physical and thermal properties of the fluid due to a temperature change are neglected. Consequently, the governing equations for the velocity and thermal fields are the following Navier-Stokes, continuity and passive scalar transport equations:

$$\frac{\partial u_i}{\partial t} + \frac{\partial (u_j u_i)}{\partial x_j} = -\frac{\partial p}{\partial x_i} + \frac{1}{Re} \frac{\partial^2 u_i}{\partial x_j \partial x_j}, \quad (3.1)$$

$$\frac{\partial u_i}{\partial x_i} = 0, \quad (3.2)$$

$$\frac{\partial \theta}{\partial t} + \frac{\partial (u_j \theta)}{\partial x_j} = \frac{1}{RePr} \frac{\partial^2 \theta}{\partial x_j \partial x_j} + Q, \quad (3.3)$$

where  $p$  and  $\theta$  denote static pressure and temperature, respectively. A heat source is expressed by  $Q$ , which is generally an arbitrary function of space and time. The above equations are non-dimensionalized by the bulk mean velocity  $U_b^*$ , the bulk mean temperature  $\theta_b^*$ , and the

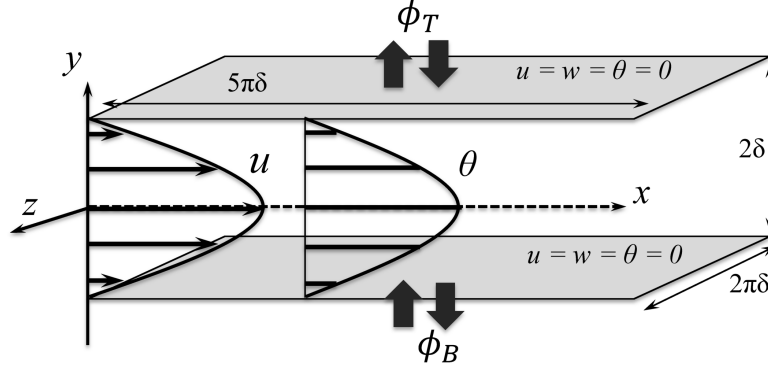


Figure 3.1 Schematic of the flow domain.

channel half height  $\delta^*$ , where a quantity with an asterisk represents a dimensional value. The bulk velocity and temperature,  $U_b^*$  and  $\theta_b^*$ , are both defined based on their volume average as follows:

$$U_b^* = \frac{1}{2\delta^*} \int_{-\delta^*}^{\delta^*} \overline{u^*} dy, \quad (3.4)$$

$$\theta_b^* = \frac{1}{2\delta^*} \int_{-\delta^*}^{\delta^*} \overline{\theta^*} dy. \quad (3.5)$$

The over-bar in (3.4) and (3.5) represents averaging over homogeneous directions  $x$  and  $z$ , and time  $t$ . We note that the above definition of  $\theta_b^*$  is different from the so-called mixing-cup temperature, which is defined based on the total enthalpy flux across a cross section. The advantage of the current definition (3.5) is that it has similar form to (3.4), so that they have exactly the same value when the velocity and temperature profiles are similar. It is known that the current definition of  $\theta_b^*$  slightly overestimates the increase rate of heat transfer due to control by around 5% (Hasegawa and Kasagi, 2011). As will be shown in § 3.2, the heat transfer is enhanced by about two times compared to the uncontrolled value for the optimal input, so that the effect of the different definitions of  $\theta_b^*$  remains minor, and does not change the present conclusions. The bulk Reynolds number  $Re$  and the Prandtl number  $Pr$  are respectively defined as  $Re = U_b^* \delta^* / \nu^*$  and  $Pr = \nu^* / \alpha^*$ . Here  $\nu^*$  represents the kinematic viscosity and  $\alpha^*$  is the thermal diffusivity of the fluid.

Following Hasegawa and Kasagi (2011) and Yamamoto et al. (2013), the governing equations and boundary conditions for streamwise velocity,  $u$ , and temperature,  $\theta$ , are made similar by introducing the following ideal conditions: First, the heat source term  $Q$  is assumed

to be uniform in space and is set equal to the mean pressure gradient driving the flow. Namely,

$$Q = -\frac{\partial \bar{p}}{\partial x}. \quad (3.6)$$

Second,  $Pr$  is set to be unity. Third,  $u = \theta = 0$  is imposed on the two walls, so that the boundary conditions for  $u$  and  $\theta$  are also similar. A no-slip condition is also employed for the spanwise velocity component  $w$  on the wall, while only the wall-normal velocity component on the wall is changed in time and space in order to realize a streamwise traveling wave as explained in § 3.1.3.

We note that the current configuration is considered to be the most difficult case to achieve dissimilarity, while it provides a unique opportunity to discuss the effect of the continuity constraint on dissimilarity between heat and momentum transfer, since all the other sources of dissimilarity are removed. All simulations in this study are conducted under a constant flow rate condition with  $Re = U_b^* \delta^* / \nu^* = 2293$ , which corresponds to the friction Reynolds number of  $Re_\tau = u_\tau^* \delta^* / \nu^* = 150$  for the uncontrolled flow. Here, the friction velocity is defined as  $u_\tau^* = \sqrt{\tau^* / \rho^*}$ , where  $\tau^*$  is the wall shear stress and  $\rho^*$  is the fluid density. Throughout the present manuscript, a quantity with the superscript of  $+$  represents a value in the wall unit based on the friction velocity in the uncontrolled flow. In order to keep the flow rate constant, the mean pressure gradient is adjusted every time step. This means that the uniform heat source term  $Q$  also changes in time due to equation (3.6). However, the temporal fluctuation of  $-\partial \bar{p} / \partial x$ , and thereby  $Q$ , is quite small, so that its effects on the control performances are negligible in the present configuration.

### 3.1.2 Numerical setup

In the present DNSs, a pseudo spectral method with Fourier expansion in  $x$  and  $z$  directions, and Chebyshev polynomials in  $y$  is used for spatial discretization. 3/2-rule is applied to remove aliasing errors. The primitive variables, i.e.  $u$ ,  $v$ ,  $w$  and  $p$ , are directly solved, while the pressure is decoupled from the Navier-Stokes equations (3.1) by the fractional step method (Kim and Moin, 1985). For temporal advancement, the second-order Adams-Bashforth method is applied for the convection terms, whereas the Crank-Nicolson method is used for the diffusion terms. The present code has been validated and applied to control and estimation problems of a fully developed turbulent channel flow in Hasegawa and Kasagi (2011) and Suzuki and Hasegawa (2017).

The dimensions of the computational domain in the streamwise, wall-normal, and spanwise directions are set to be  $(L_x, L_y, L_z) = (5\pi, 2, 2\pi)$ . The corresponding number of modes

in each direction is  $(N_x, N_y, N_z) = (128, 65, 128)$ . The present domain widths in  $x$  and  $z$  directions are twice the sizes used in Hasegawa and Kasagi (2011), while the grid resolution is kept unchanged in all three directions. It has been already shown that further grid refinement does not affect the properties of the optimal control inputs obtained from the suboptimal and optimal control theories (Hasegawa and Kasagi, 2011; Yamamoto et al., 2013). In the present study, however, we cover a wide range of the parameter space far away from the control inputs considered in the previous studies. For this reason, we perform grid convergence studies by doubling the grid resolutions in all three directions around the globally optimal control input and also for the largest wavelength, in which the wall friction is found to be maximum. It is confirmed that the further grid refinement has minor impacts on the control performances presented in the present study. Detailed results on the grid convergence study can be found in appendix A.2.

All simulations start from the same initial condition, which is a fully developed state without control. The time step is set to be  $\Delta t^+ = 0.045$  for all cases. After starting the simulation, the magnitude of the control input is linearly increased for the initial period of  $T^+ = 45$ , and kept constant for a subsequent period of  $T^+ = 2250$  in order to ensure that the flow reaches a fully developed state under the control. Note that a typical transient time of wall friction and wall heat flux after applying a control is found to be around  $T^+ \sim 500$  for traveling waves close to the optimal condition. After the controlled flow reaches a fully developed state, additional computation is conducted for  $T^+ = 4500$  in order to obtain the turbulence statistics which are presented in the following sections.

### 3.1.3 Control input

A sinusoidal traveling wave-like wall blowing and suction, which is uniform along the spanwise direction, is imposed as the control input. It can be described on the bottom wall at  $y = -1.0$  as

$$v_w = \phi \sin \left\{ \frac{2\pi}{\lambda_x} (x - U_p t) \right\}, \quad (3.7)$$

where,  $\phi$ ,  $\lambda_x$ , and  $U_p$  are the amplitude, wavelength, and phase-speed of the traveling wave, respectively. The subscript of  $w$  indicates the quantity on the bottom wall. Note that the control input is applied at the two walls in a varicose mode, since it was obtained in both the suboptimal and optimal control theories (Hasegawa and Kasagi, 2011; Yamamoto et al., 2013). Hence, the wall-normal velocity component at the top wall ( $y = 1.0$ ) is given by the same formula (3.7), but with the opposite sign. Although we focus on a varicose mode, the effects

of the phase-angle between the control inputs at the top and bottom walls are also investigated for several cases including at the global optimal point identified in the present study. We confirmed that the phase-angle hardly affects the resultant control performance (see appendix B.2 for more detailed results). The root-mean-square (RMS) value of the control input is set to be 5% of the bulk mean velocity, which is equivalent to that obtained from the optimal control theory by Yamamoto et al. (2013). It corresponds to the control input amplitude of  $\phi = 0.07$  or  $\phi^+ = 1.08$  in a wall unit. We also note that this amplitude is smaller than that considered in Higashi et al. (2011), where  $\phi^+$  is around 3.0. The range of the streamwise wavelength and the phase-speed considered in the present study are  $5\pi/32 \leq \lambda_x \leq 5\pi$  and  $-3.0 \leq U_p \leq 3.0$ , respectively. This corresponds to  $70 \lesssim \lambda_x^+ \lesssim 2300$  and  $-45 \lesssim U_p^+ \lesssim 45$  in wall units of the uncontrolled flow. 104 simulations are first conducted to cover the above mentioned parameter range, and then additional 36 cases are performed to identify the globally optimal set of the control parameters, so that the total number of simulations is  $104 + 36 = 140$ . The largest wavelength of  $\lambda_x = 5\pi$  considered in the study is equal to the streamwise dimension of the computational domain. Hence, we also carried out additional computations for  $\lambda = 5\pi$  at different phase-speeds with doubled streamwise domain size in order to confirm that the streamwise domain size does not affect the control performances.

### 3.1.4 Control performance indices

As discussed in § 2.1.4 the major performance indicators are the skin-friction coefficient  $C_f$  for drag, the Stanton number  $St$  for heat transfer, and the analogy factor  $A$  for the dissimilarity between momentum and heat transfer. In addition, we can define  $C_{f_{net}}$ ,  $C_{f_{csv}}$ ,  $A_{net}$ , and  $A_{csv}$  by considering the power required for the control (refer equations 2.13 and 2.14).

Even in TCF,  $A$  becomes unity when  $\bar{\theta}$  and  $\bar{u}$  have a similar profile. Indeed, it is almost unity for the present uncontrolled case, namely,  $A_0 = 2St_0/C_{f_0} \approx 1.0$ , where  $C_{f_0} = 8.58 \times 10^{-3}$  and  $St_0 = 4.30 \times 10^{-3}$ . Such a situation can be considered as the case where the Reynold's analogy holds perfectly.

## 3.2 Control Performances

### 3.2.1 Skin-friction coefficient

The skin-friction coefficient normalized by its uncontrolled value  $C_{f_0}$  is plotted as a function of  $U_p$  and  $\lambda_x$  in figure 3.2. All the combinations of  $\lambda_x$  and  $U_p$  for which DNSs are conducted

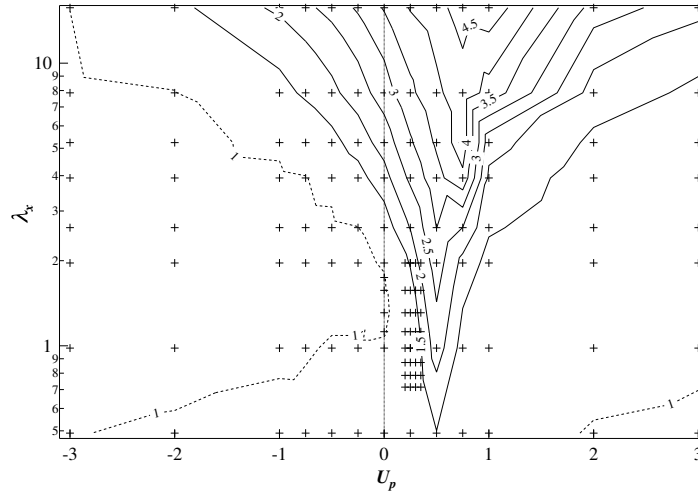


Figure 3.2 Normalized skin-friction coefficient  $C_f/C_{f_0}$ . Contours with a value less than or equal to one are shown by dashed lines.

are denoted by crosses. The contours with a value less than or equal to one are shown using dashed lines, and this applies to all the contour plots in the following sections. It is found that drag reduction is confirmed in a large area of  $U_p < 0$  (UTW), while prominent increase of drag is observed for  $U_p > 0$  (DTW), especially for  $0 < U_p < 1$ , and then the drag gradually reduces again with further increase in  $U_p$  above one. The drag reduction observed for  $U_p < 0$  can be mostly attributed to the streaming effect (Hoepffner and Fukagata, 2009), which drives the flow in the opposite direction to that of the applied traveling wave. For a steady wave, i.e.  $U_p = 0$ , drag reduction is also obtained in the limited range of  $1.12 < \lambda_x < 1.74$  with a maximum drag reduction of 2% at  $\lambda_x = 1.30$ . These results agree well with the previous findings by Quadrio et al. (2007), where drag reduction is obtained for a turbulent channel flow at  $Re_\tau = 180$  by a steady sinuous mode wave for  $0.55 < \lambda_x < 1.94$  with amplitude  $\phi^+ = 0.70$ . According to their prediction, a varicose mode with  $\lambda_x = 1.25$  and  $\phi^+ = 1.0$  would have resulted in a drag reduction of 2.20% approximately (see table 1 in their appendix).

Figure 3.2 shows that for any particular value of  $\lambda_x$  the maximum value of  $C_f$  occurs around  $U_p \approx 0.50$ , and it is in agreement with the results of Mamori et al. (2014). This sudden increase in the value of  $C_f$  around  $U_p \approx 0.50$  is attributed to the presence of a critical layer (Hoepffner and Fukagata, 2009; Mamori et al., 2010), which amplifies velocity fluctuations through the interaction between the mean velocity field and the control input (Maslowe, 1986). Similar drag increase is also reported for a streamwise traveling wave of spanwise



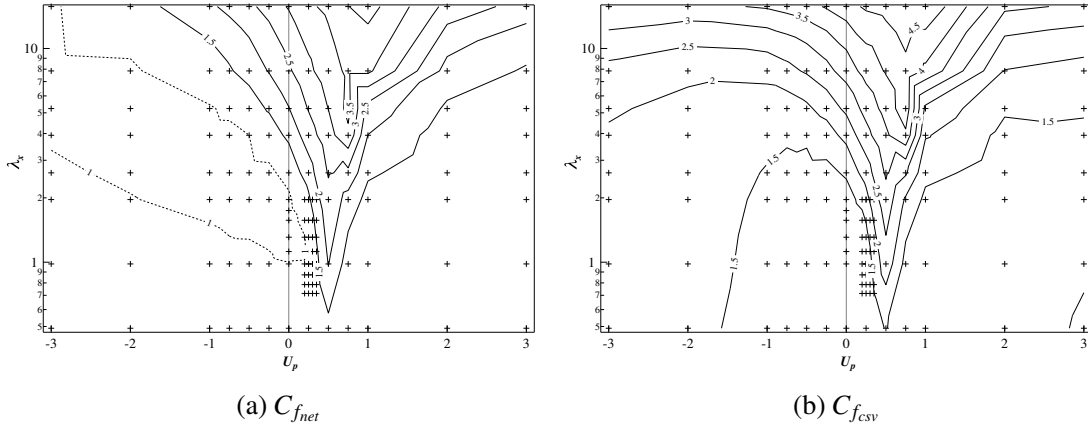


Figure 3.3 Skin-friction coefficient: (a)  $C_{f_{net}}/C_{f_0}$  and (b)  $C_{f_{csv}}/C_{f_0}$ . Contours with a value less than or equal to one are shown by dashed lines.

wall forcing at both internal and external surfaces (Quadrio et al., 2009; Zhao et al., 2019). In these studies, the maximum of  $C_f$  occurs around  $U_p^+ = 10$ , which is slightly higher than that obtained in the current study. This difference would be attributed to the difference in the direction of wall forcing.

It can be seen from figure 3.2 that DTW also leads to drag reduction, but is limited to a quite small region of  $U_p > 2.0$  and small  $\lambda_x$ . Mamori et al. (2014) reported that even relaminarization would happen when  $\phi^+ > 5$ ,  $U_p^+ > 75$ , and  $200 < \lambda_x^+ < 500$ . Since we consider a smaller magnitude for the control input  $\phi^+ = 1.08$ , we do not observe relaminarization, although the present ranges of  $\lambda_x$  and  $U_p$  are similar to those considered in Mamori et al. (2014).

The plots of  $C_{f_{net}}$  and  $C_{f_{csv}}$  normalized by their uncontrolled values are shown in figures 3.3a and 3.3b, respectively. In accordance with their respective definitions (refer 2.13)  $C_{f_{net}}$  can be either greater or smaller than  $C_f$  depending on the sign of the net energy expenditure for control, whereas  $C_{f_{csv}}$  will be always larger than  $C_f$ . After taking into account the power consumption for the control, the net energy saving is achieved only in a narrower region for  $C_{f_{net}}$ , and no energy saving is obtained in terms of  $C_{f_{csv}}$  for all the cases considered presently. The above results indicate that, in the present configuration, a net energy saving is not achieved via a streamwise traveling wave of wall blowing and suction, unless the energy recovery from the flow field through actuators is allowed.

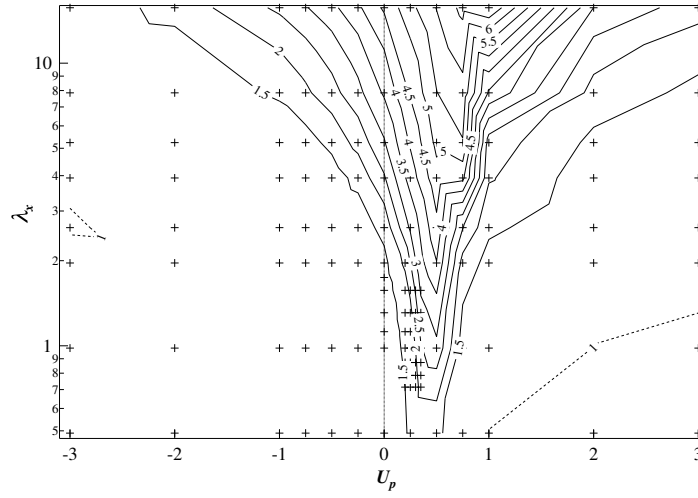


Figure 3.4 Normalized Stanton number  $St/St_0$ . Contours with a value less than or equal to one are shown by dashed lines.

### 3.2.2 Stanton number

The Stanton number normalized by its uncontrolled value  $St_0$  is plotted as a function of  $U_p$  and  $\lambda_x$  in figure 3.4. In general, the trend of  $St/St_0$  is quite similar to that of  $C_f/C_{f_0}$  shown in figure 3.2. However, there are two main differences. First, heat transfer enhancement is obtained for a wide region of UTW ( $U_p < 0$ ), where drag reduction is widely confirmed as shown in figure 3.2. Second, a similar peak of  $St/St_0$  is found around  $U_p \approx 0.50$ , while its value is larger than  $C_f/C_{f_0}$ . We also note that, unlike the contour plot of  $C_f/C_{f_0}$ , the region where heat transfer is reduced from the uncontrolled value is quite limited. This suggests that dissimilar heat transfer is achieved in a wide range of the parameter space.

### 3.2.3 Analogy factor

The iso-contours of  $A$  are plotted as a function of  $U_p$  and  $\lambda_x$  in figure 3.5. It is found that UTW achieves dissimilar control, i.e.  $A > 1$ , for the entire parameter set of  $(\lambda_x, U_p)$  considered in the present study. This confirms the findings of Higashi et al. (2011), in which they obtained dissimilar heat transfer enhancement using UTW for a turbulent channel flow at  $Re_\tau \approx 180$ .

In contrast, more significant enhancement of  $A$  is obtained for DTW with  $0 < U_p < 1$ . Specifically, the maximum value of the analogy factor,  $A = 1.69$ , is obtained at  $(\lambda_x, U_p) = (1.12, 0.30)$ . Hereafter, we regard this control input as the global optimum in order to distin-

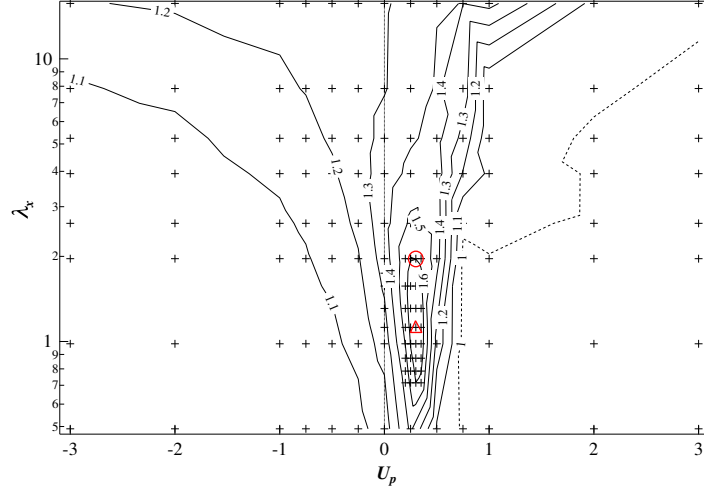


Figure 3.5 Analogy factor  $A$ . The red circle indicates the wave parameters  $(\lambda_x, U_p) = (1.96, 0.30)$  obtained from the optimal control theory (Yamamoto et al., 2013) and the red triangle indicates the global optimum of the wave parameters, i.e.,  $(\lambda_x, U_p) = (1.12, 0.30)$  obtained from the present DNSs. Contours with a value less than or equal to one are shown by dashed lines.

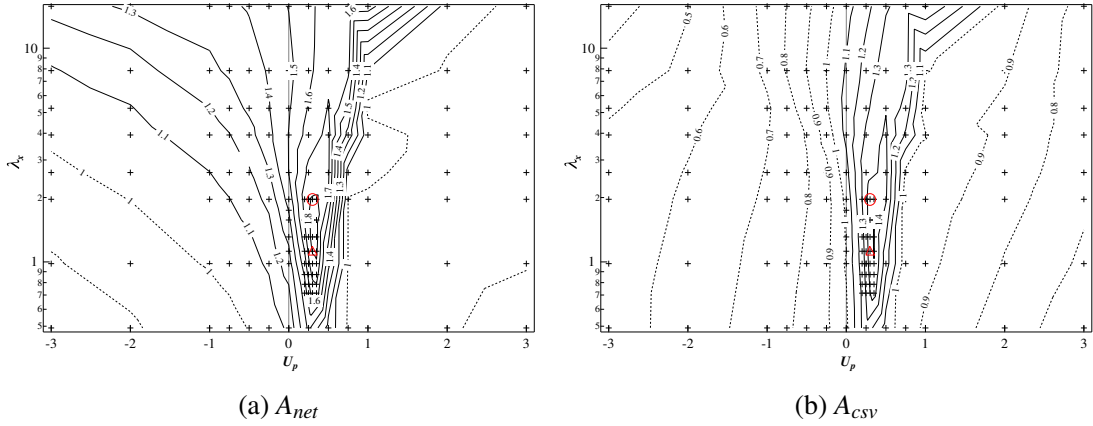


Figure 3.6 Analogy factor: (a)  $A_{net}$  and (b)  $A_{csv}$ . The circle indicates the wave parameters  $(\lambda_x, U_p) = (1.96, 0.30)$  obtained from the optimal control theory (Yamamoto et al., 2013) and the triangle indicates the global optimum of wave parameters  $(\lambda_x, U_p) = (1.12, 0.30)$  obtained from the present DNSs. Contours with a value less than or equal to one are shown by dashed lines.

$C_f/C_{f0}$	$C_{f_{net}}/C_{f0}$	$C_{f_{csv}}/C_{f0}$	$St/St_0$	$A$	$A_{net}$	$A_{csv}$
1.26	1.17	1.46	2.12	1.69	1.81	1.45

Table 3.1 Summary of the control performances for the globally optimal control input with  $(\lambda_x, U_p) = (1.12, 0.30)$ .

guish it from those obtained under the suboptimal and optimal control theories. Interestingly, these optimal wave parameters are quite close to  $(\lambda_x, U_p) = (1.96, 0.30)$  obtained via the optimal control theory by Yamamoto et al. (2013), where  $A = 1.55$  is achieved. Specifically, the optimal phase-speed obtained from the present parametric study and that from the optimal control theory (Yamamoto et al., 2013) are identical. The slight difference in the wavelength between the present global optimum and that obtained by the optimal control theory could be attributed to the limitation of the time horizon. In fact, in the case of the suboptimal control, where the time horizon is assumed to be vanishingly small, the wavelength of the resultant control input extends to the entire computational domain (Hasegawa and Kasagi, 2011). Hence, there exists a trend that the wavelength obtained by the optimal control theory tends to decrease with increasing the time horizon. Considering that the present parametric survey seeks the optimum for a sufficiently large time horizon, it is consistent that the globally optimal wavelength is slightly shorter than that obtained from the optimal control theory.

The contour plots of  $A_{net}$  and  $A_{csv}$  are presented in figure 3.6. Both figures clearly show that dissimilar control can be achieved even after taking into account the power required for applying the control. It is found that  $A_{net}$  and  $A_{csv}$  have their maximum values of 1.84 and 1.51 respectively at the same wave parameters of  $(\lambda_x, U_p) = (1.309, 0.35)$ . The global optimum of  $(\lambda_x, U_p)$  for  $A_{net}$  and  $A_{csv}$  are still close to those of  $A$ . This could be attributed to the fact that we consider a relatively small amplitude of the control input, so that the power consumption for control remains minor. The summary of control performances for the globally optimal control input is given in table 3.1. It should be noted that the maximum value of  $A_{net}$  is greater than that of  $A$ , since the net control power input  $\Pi$  becomes negative around the optimal condition. This suggests that actuators could work without external power input ideally, or the dissimilar control could be achieved by passive means such as a properly designed compliant surface which reacts to the fluid force and induces a traveling wave close to the globally optimal mode.

Even after excluding the energy recovery from the actuators, dissimilar heat transfer is still confirmed with the area of  $A_{csv} > 1$  shown in figure 3.6b. Compared with  $A$  shown

in figure 3.5, however,  $A_{csv}$  is significantly suppressed, especially for UTW. In the present configuration, there are a few cases where simultaneous drag reduction and heat transfer enhancement is achieved. Among them, a relatively large  $A$  is achieved for  $1.12 \leq \lambda_x \leq 1.75$  and  $U_p = 0$  at  $Re_\tau = 150$ . In these cases, however, the drag reduction rate achieved is less than 2%, and  $St$  is enhanced by only around 30%, so that the resultant  $A$  is limited to around 1.3 at most. In addition,  $C_{f_{csv}}/C_{f_0}$  is always larger than unity, so that they are not advantageous from an energetic viewpoint. In summary, figure 3.3b together with figure 3.6b reveal that, from the energetic point of view, UTW is no longer effective for neither drag reduction nor dissimilar control under the small amplitude of the control input considered in the present study.

### 3.2.4 Reynolds number effect and the scaling of the optimal wave parameters

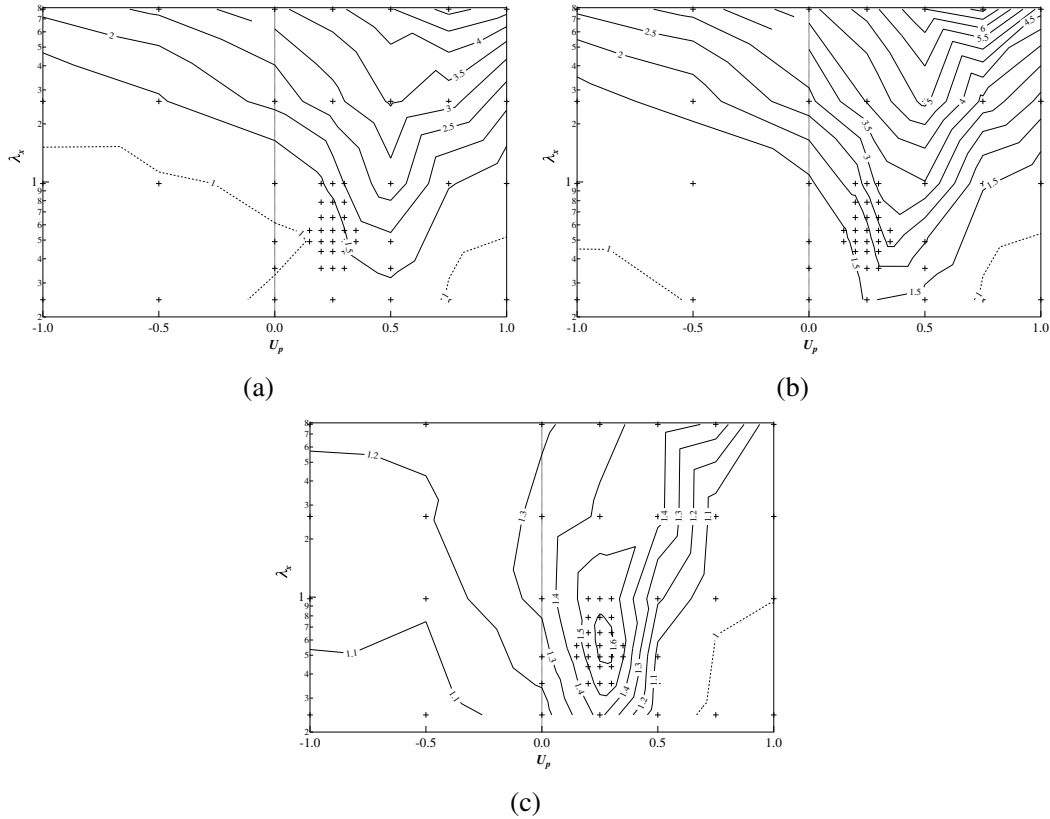


Figure 3.7 Contour plot of (a)  $C_f/C_{f_0}$ , (b)  $St/St_0$ , and (c)  $A$ , as a function of  $(\lambda_x, U_p)$  for  $Re_\tau = 300$ . Contours with a value less than or equal to one are shown by dashed lines.

Even though it is outside the scope of the present work to extensively investigate the Reynolds number effect on the optimal traveling wave parameters, we also conduct a parametric study at  $Re = 5055$ , which corresponds to  $Re_\tau = 300$  in the uncontrolled flow. The computational domain size, the numbers of spectral modes, the number of grid points in the physical space, and the grid spacing used are outlined in Table 3.2. The uncontrolled values of the skin-friction coefficient and the Stanton number for  $Re_\tau = 300$  are  $C_{f_0} = 7.03 \times 10^{-3}$  and  $St_0 = 3.57 \times 10^{-3}$ , respectively. The magnitude of the control input with respect to the bulk mean velocity is set to be  $\phi_{rms} = 0.05$ , which is the same as the cases for  $Re_\tau = 150$ .

Among the 56 cases,  $A$  has the maximum value of 1.62 at  $(\lambda_x, U_p) = (0.65, 0.25)$  as shown in figure 3.7. Evidently, the optimal wavelength is not scaled with the channel half-height (Remember that the global optimum for  $Re_\tau = 150$  is  $(\lambda_x, U_p) = (1.12, 0.3)$ ). Instead, the global optimum can be well scaled in the wall unit as summarized in Table 3.3. Figure 3.8 shows the contour plot of  $C_f/C_{f_0}$ ,  $St/St_0$ , and  $A$  as a function of  $(\lambda_x^+, U_p^+)$  for both  $Re_\tau = 150$  (black lines) and  $Re_\tau = 300$  (thick red lines). Good agreement between the respective contours of  $Re_\tau = 150$  and  $Re_\tau = 300$  suggests that the control performances are correlated with the wave properties in the wall units. It is worth noting that the analogy factor as high as 1.6 can be obtained for both  $Re_\tau = 150$  and  $Re_\tau = 300$  under the small amplitude of the control input considered in the present study.

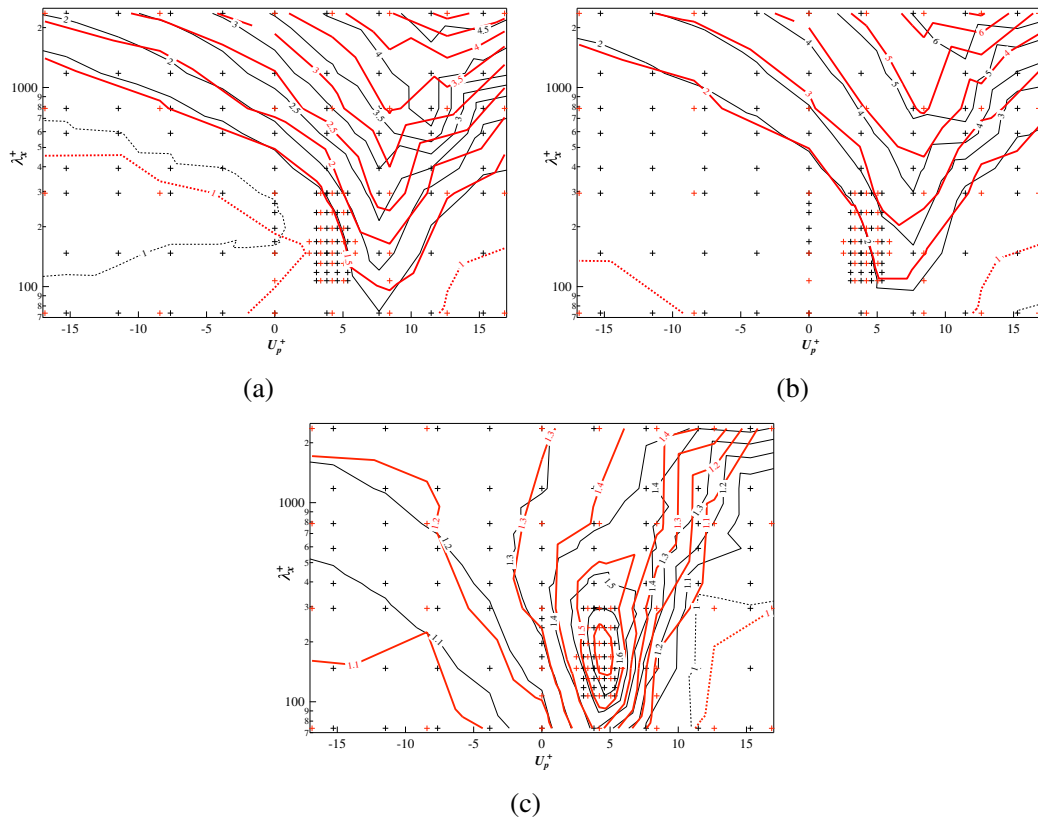


Figure 3.8 Contour plot of (a)  $C_f/C_{f0}$ , (b)  $St/St_0$ , and (c)  $A$ , as a function of  $(\lambda_x^+, U_p^+)$  for  $Re_\tau = 150$  (black lines) and  $Re_\tau = 300$  (thick red lines). Contours with a value less than or equal to one are shown by dashed lines.

	$(L_x, L_y, L_z)$	$(N_x, N_y, N_z)$	$(M_x, M_y, M_z)$	$(\Delta x^+, \Delta y_{min}^+, \Delta y_{max}^+, \Delta z^+)$	$\Delta t^+$
$Re_\tau = 150$	$(5\pi, 2, 2\pi)$	$(128, 64, 128)$	$(192, 97, 192)$	$(12.27, 0.08 - 9.82, 4.90)$	0.045
$Re_\tau = 300$	$(2.5\pi, 2, \pi)$	$(128, 128, 128)$	$(192, 193, 192)$	$(12.27, 0.04 - 4.91, 4.90)$	0.030

Table 3.2 Computational domain size, number of spectral modes, number of grid points and grid spacing in physical space, and the time-step used for  $Re_\tau = 150$  and 300, respectively.

	$(\lambda_x, U_p)$	$(\lambda_x^+, U_p^+)$	$(\lambda_{xc}^+, U_{pc}^+)$	$C_f/C_{f0}$	$St/St_0$	$A$
$Re_\tau = 150$ ( $Re_b = 2293$ )	$(1.12, 0.30)$	$(168.30, 4.59)$	$(188.79, 4.09)$	1.26	2.12	1.69
$Re_\tau = 300$ ( $Re_b = 5054$ )	$(0.65, 0.25)$	$(196.35, 4.21)$	$(220.90, 3.74)$	1.27	2.06	1.62

Table 3.3 Summary of the control performances for  $Re_\tau = 150$  and 300 at their respective optimal points. Here  $(\lambda_x^+, U_p^+)$  and  $(\lambda_{xc}^+, U_{pc}^+)$  respectively represents quantities normalised in wall units corresponding to the un-controlled and controlled flow.



Figures 3.9 and 3.10 show the comparison of the analogy factor performance from the present study with that of the existing works. Even though the present control input is able to generate a value greater than one for both  $A$  and  $A_{csv}$ , there is dip in both these values as the flow regime changes from laminar to turbulent. This indicates the untapped potential for the use of transitional flow regimes while designing energy efficient systems.

So far, we have seen that DTW is particularly effective in achieving dissimilar heat transfer enhancement. In the following sections, we focus on the globally optimal traveling wave of  $(\lambda_x, U_p) = (1.12, 0.30)$  at  $Re_\tau = 150$ , and discuss its control mechanisms in detail by applying triple decomposition to the velocity and thermal fields and clarifying the contributions to the dissimilarity from each component.

### 3.3 Mechanisms of Dissimilarity

#### 3.3.1 Triple decomposition

Since the present control applies a streamwise traveling wave of wall blowing and suction, the resultant fluctuating velocity and thermal fields can be considered as the superposition of the coherent fluctuation which travels downstream with the control input and the residual incoherent motions. Following the triple decomposition of Hussain and Reynolds (1970), an arbitrary quantity  $f$  can be decomposed as

$$f(x, y, z, t) = \langle f(\xi, y) \rangle + f''(x, y, z, t), \quad (3.8)$$

where  $\langle f \rangle$  and  $f''$  are termed as phase-averaged and random components of  $f$ , respectively. Here  $\xi$ , where  $\xi = x - U_p t + \lambda_x/4$ , represents the streamwise coordinate that is traveling at the same speed as the control input so that  $\xi = 0$  always corresponds to the location where the wall suction becomes maximum. The phase-averaged component  $\langle f \rangle$  can be further decomposed into mean component  $\bar{f}$ , which is an averaged quantity in  $x$  and  $z$  directions and also time  $t$ , and coherent component  $\tilde{f}$ . As a result, equation (3.8) can be rewritten as

$$f(x, y, z, t) = \bar{f}(y) + \tilde{f}(\xi, y) + f''(x, y, z, t). \quad (3.9)$$

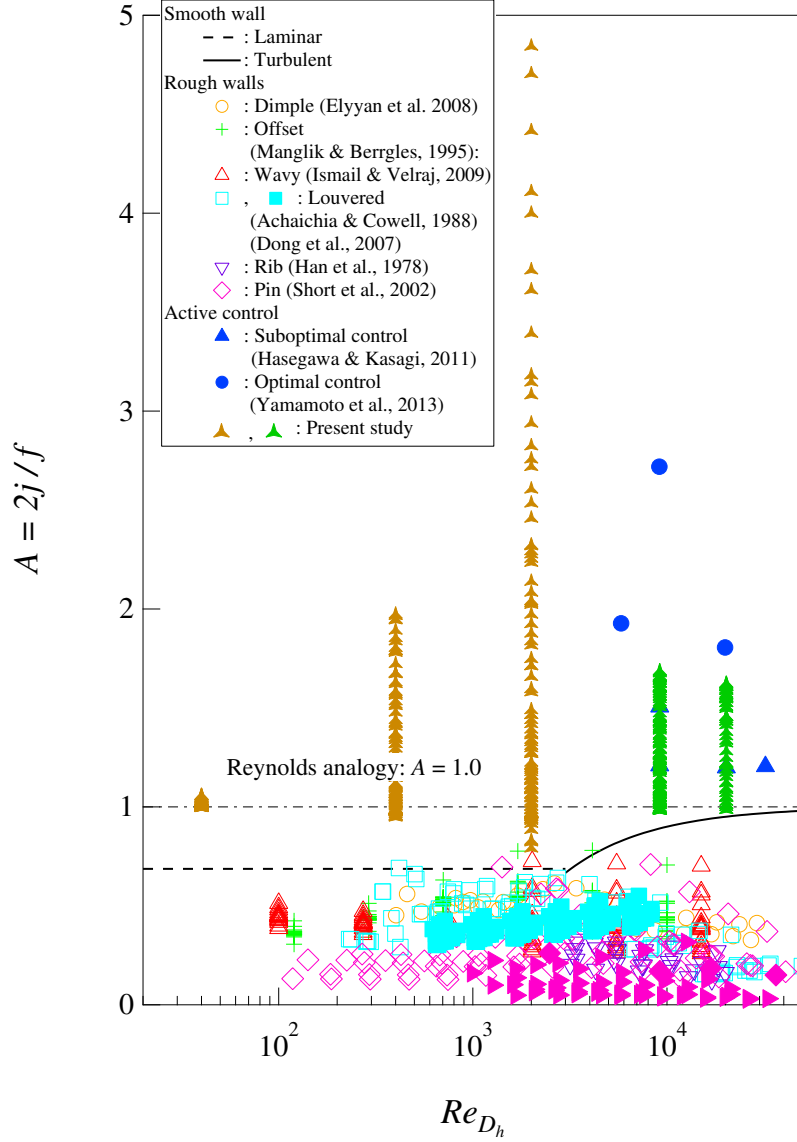


Figure 3.9 Analogy factor  $A$  as a function of  $Re_{D_h}$  for different heat transfer surfaces. The figure is same as that shown in 1.1 but with the data points included from the present study. Here  $Re_{D_h}$  is the Reynolds number based on the hydraulic diameter  $D_h$  which for a plain channel is given by  $D_h = 4\delta$ , where  $\delta$  is the half channel height. For laminar regime (dashed line), *i.e.*  $Re_{D_h} < 3000$ , a constant heat flux condition is assumed resulting in a constant value for  $A = 0.69$ . For the turbulent regime (solid line)  $C_f = 0.087Re_{D_h}^{-1/4}$  (Dean, 1978) and  $j = 0.024Re_{D_h}^{-1/5}Pr^{1/6}$  (Keys et al., 2005). For both laminar and turbulent regime  $Pr$  is set equal to one.

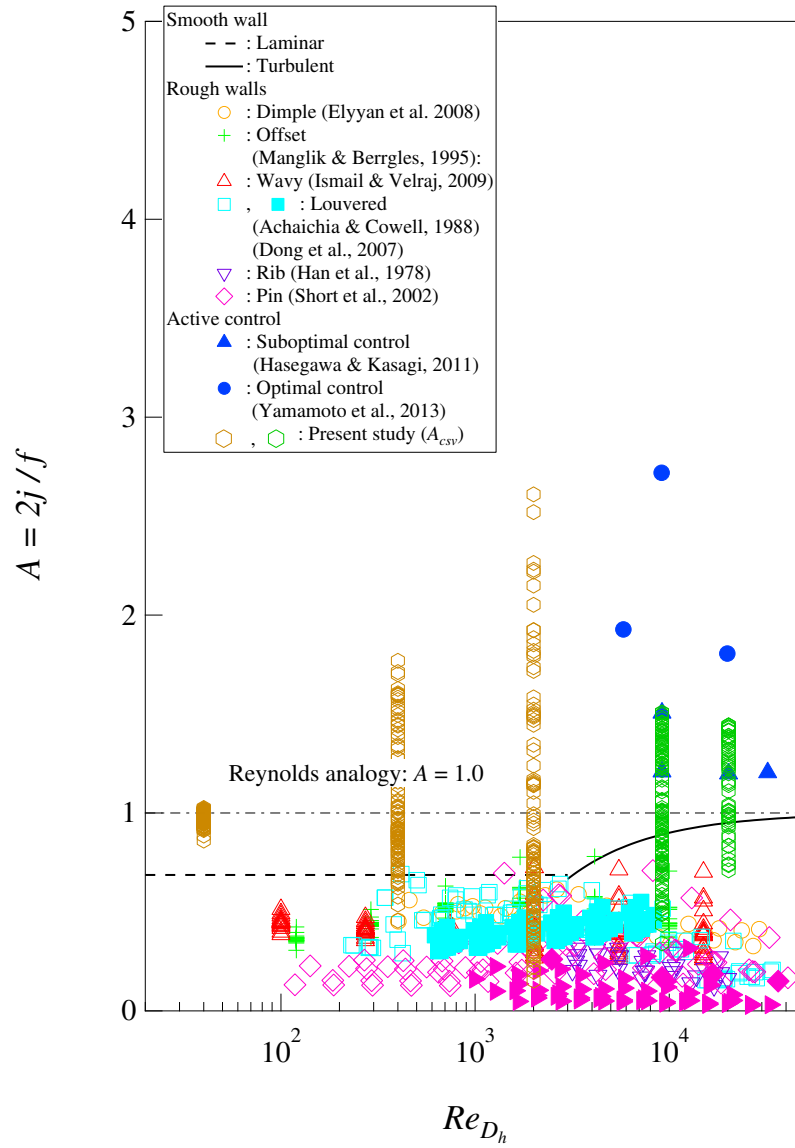


Figure 3.10 Same plot as in figure 3.9, except that  $A_{CSV}$  is plotted instead of  $A$  from the present study.

Consequently, the velocity and temperature fields can be decomposed into mean, coherent and random components as shown below:

$$u_i = \bar{u}_i + \tilde{u}_i + u_i'',$$

$$\theta = \bar{\theta} + \tilde{\theta} + \theta''.$$

### 3.3.2 Decomposition into coherent and random contributions

#### FIK identity

The FIK-identity (Fukagata et al., 2002) is useful to distinguish between the laminar and turbulent contributions to  $C_f$ , and can be written under a constant flow rate as

$$C_f^{FIK} = \frac{6}{Re} + 3 \int_{-1}^1 y \overline{u'v'} dy. \quad (3.10)$$

Here, the two terms on the RHS quantify the contributions from the laminar and turbulent components, respectively. Similarly,  $St$  can be decomposed as (Hasegawa and Kasagi, 2011)

$$2St^{FIK} = \frac{6}{Re} + 3 \int_{-1}^1 y \overline{\theta'v'} dy. \quad (3.11)$$

Since the first terms in equations (3.10) and (3.11) are identical and constant, the dissimilarity between  $C_f$  and  $St$  should result from the difference between the turbulence contributions appearing as the second terms on the RHS of equations (3.10) and (3.11). In figures 3.11(a) and 3.11(b), the values of  $C_f$  and  $St$  estimated from FIK-identity equations (3.10) and (3.11), i.e.  $C_f^{FIK}$  and  $St^{FIK}$ , are compared with those obtained from direct integration of wall shear stress and wall heat flux as given by equations (1.1) and (1.2) for all the cases considered. It is evident that all the points fall in close proximity of the diagonal line for both  $C_f$  and  $St$ . More specifically, the discrepancy between the values obtained from the two approaches is typically in the order of 0.1 % for  $C_f$ , while it is slightly larger (around 0.5 %) for  $St$ . Excellent agreement in figures 3.11(a) and 3.11(b) confirms that all the controlled flows have already reached fully developed states, and the present integration time is sufficient. Hereafter, the superscript of  $FIK$  will be omitted, since the discrepancy between  $C_f$  and  $C_f^{FIK}$ , and that between  $St$  and  $St^{FIK}$  are negligibly small in comparison to their changes due to the applied control (see figures 3.2 and 3.4).

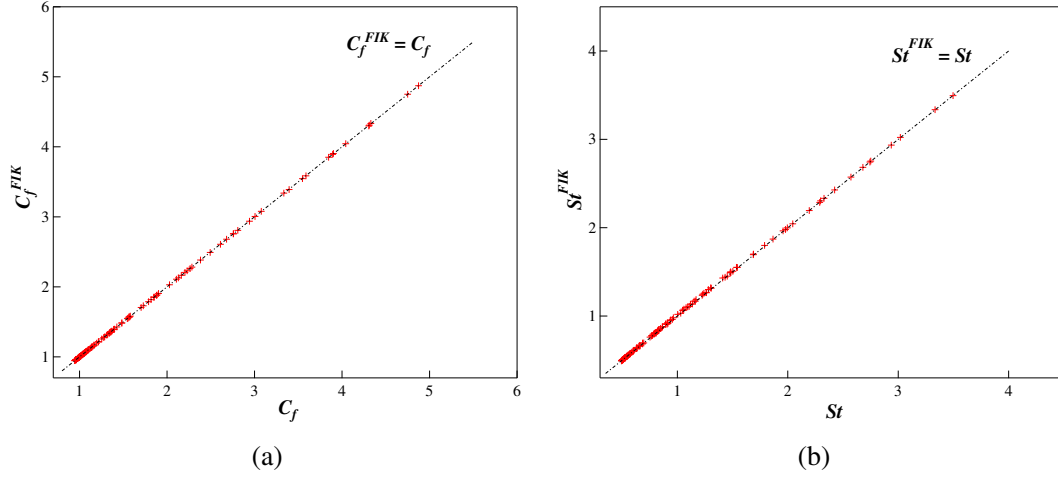


Figure 3.11 Comparison of  $C_f$  and  $St$  estimated from FIK-identity equations (3.10) and (3.11) with those obtained from direct integration of wall shear stress and wall heat flux given by equations (1.1) and (1.2) for all 140 cases considered in the present DNSs.

### Decomposition of turbulent contribution

Decomposing the turbulent fluctuations in equations (3.10) and (3.11) into their coherent and random components, we obtain

$$\begin{aligned}
 C_f &= \frac{6}{Re} + 3 \int_{-1}^1 y \bar{u} \bar{v} dy + 3 \int_{-1}^1 y \overline{u'' v''} dy \\
 &= C_f^L + C_f^C + C_f^R,
 \end{aligned} \tag{3.12}$$

$$\begin{aligned}
 2St &= \frac{6}{Re} + 3 \int_{-1}^1 y \bar{\theta} \bar{v} dy + 3 \int_{-1}^1 y \overline{\theta'' v''} dy \\
 &= St^L + St^C + St^R.
 \end{aligned} \tag{3.13}$$

Here, the superscripts  $L$ ,  $C$ , and  $R$  represent the laminar, coherent, and random contributions, respectively. In equations (3.12) and (3.13), the laminar contributions are identical to those appear as the first terms in equations (3.10) and (3.11), while the second turbulence contribution is decomposed into coherent and random contributions. It should be noted that the coherent contributions in the uncontrolled flow are null, i.e.  $C_{f_0}^C = St_0^C = 0$ .

For ease of analyses,  $C_f$  and  $St$  are normalized with their respective values for the uncontrolled flow. After dividing by  $C_{f0}$  and rearranging the terms, equation (3.12) leads to

$$\begin{aligned}\frac{C_f}{C_{f0}} &= 1 + \frac{C_f^C - C_{f0}^C}{C_{f0}} + \frac{C_f^R - C_{f0}^R}{C_{f0}} \\ &= 1 + \frac{\Delta C_f^C}{C_{f0}} + \frac{\Delta C_f^R}{C_{f0}}.\end{aligned}\quad (3.14)$$

Here  $\Delta C_f^C$  and  $\Delta C_f^R$  represent the variations of  $C_f^C$  and  $C_f^R$  from the uncontrolled values. Namely,  $\Delta C_f^C = C_f^C - C_{f0}^C = C_f^C$  and  $\Delta C_f^R = C_f^R - C_{f0}^R$ . Similarly, equation (3.13) can be rewritten as

$$\begin{aligned}\frac{St}{St_0} &= 1 + \frac{St^C - St_0^C}{St_0} + \frac{St^R - St_0^R}{St_0} \\ &= 1 + \frac{\Delta St^C}{St_0} + \frac{\Delta St^R}{St_0},\end{aligned}\quad (3.15)$$

where  $\Delta St^C = St^C - St_0^C = St^C$  and  $\Delta St^R = St^R - St_0^R$ . The advantage of the above expressions equations (3.14) and (3.15) is that the distributions shown in figures 3.2 and 3.4 are expressed as the sum of the coherent and random contributions.

The contour plots of the four terms:  $\Delta C_f^C/C_{f0}$ ,  $\Delta C_f^R/C_{f0}$ ,  $\Delta St^C/St_0$ , and  $\Delta St^R/St_0$ , are plotted as functions of  $U_p$  and  $\lambda_x$  in figure 3.12. Both the coherent and random contributions have large positive values in the region of  $0 < U_p < 1.0$ , implying that a wave traveling at a similar velocity to the bulk velocity causes resonance effects, so that both contributions are enhanced. The coherent contribution to  $C_f$  shown in figure 3.12(a) shows negative values in a wide area of  $U_p < 0$ , whereas it is positive for  $U_p > 0$ . This corresponds to the streaming effect, which drives a net flow in the opposite direction of the traveling wave. Meanwhile, the random contribution in figure 3.12(b) shows relatively small negative values for both upstream and downstream traveling waves. The suppression of the random contribution due to downstream traveling waves can be explained by the stabilizing effect (Lieu et al., 2010).

The coherent and random contributions to  $St/St_0$  shown in figures 3.12(c) and 3.12(d) have generally similar trends to the corresponding contributions of  $C_f/C_{f0}$  shown in figure 3.12(a) and 3.12(b), respectively. However, the negative regions observed in figures 3.12(a) and 3.12(b) are diminished in figures 3.12(c) and 3.12(d). Especially, the negative region of  $\Delta C_f^C/C_{f0}$  for  $U_p \leq 0$  in figure 3.12(a) totally disappears in figure 3.12(c), indicating that the streaming effect which causes drag reduction always results in heat transfer augmentation.

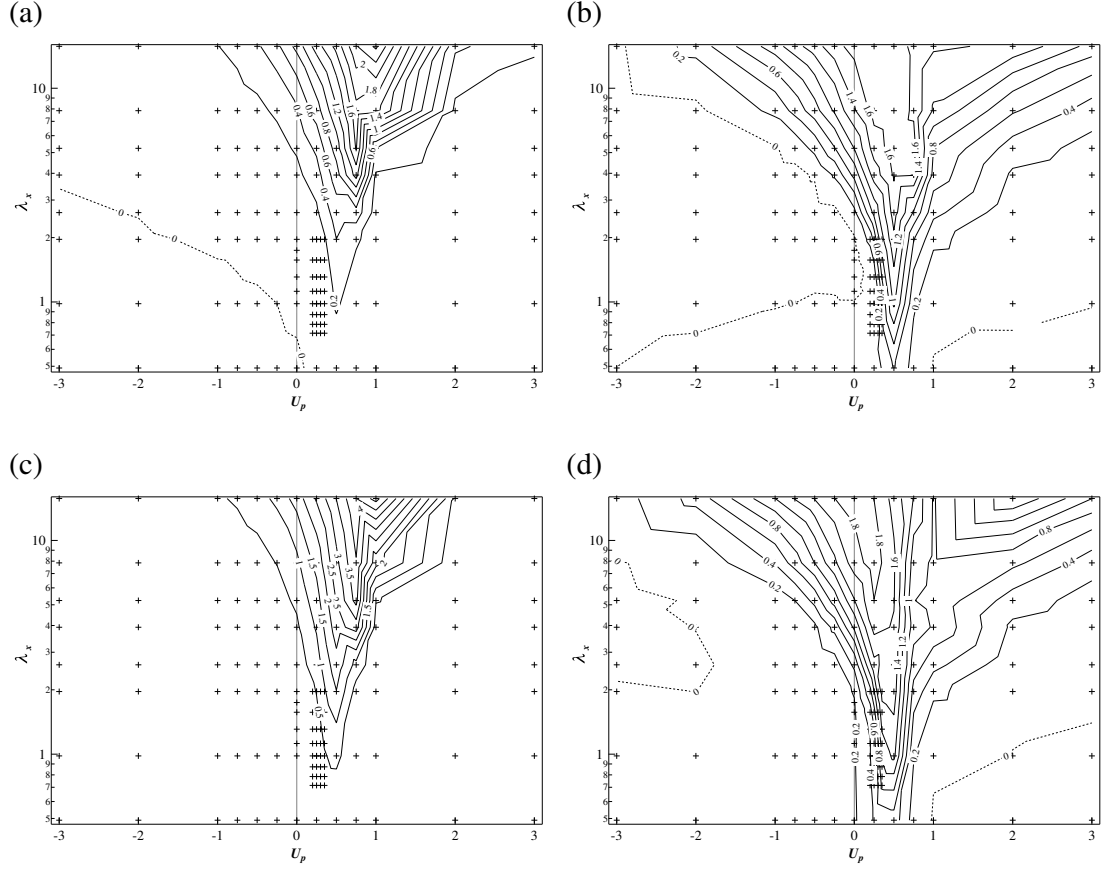


Figure 3.12 Contour plots of (a)  $\Delta C_f^C / C_{f0}$ , (b)  $\Delta C_f^R / C_{f0}$ , (c)  $\Delta St^C / St_0$ , and (d)  $\Delta St^R / St_0$  as functions of  $\lambda_x$  and  $U_p$ . Contours with a value less than or equal to 0 are shown using dashed lines.

Meanwhile, the negative regions of  $\Delta C_f^R / C_{f0}$  and  $\Delta St^R / St_0$  in figure 3.12(b) and 3.12(d) are similar. This suggests that the stabilizing effect of DTW suppresses both skin-friction drag and heat transfer similarly. Finally, although the contour plots for coherent and random contributions to  $St$  and  $C_f$  are similar in the region of  $0 < U_p < 1.0$ , the two contributions to  $St$  is generally larger than those to  $C_f$ , and this causes large dissimilarity as will be shown in the next subsection.

### Dissimilarity

In order to quantify the contributions of the coherent and random components to the dissimilarity, we introduce the following quantity  $D$  by subtracting equation (3.12) from equation

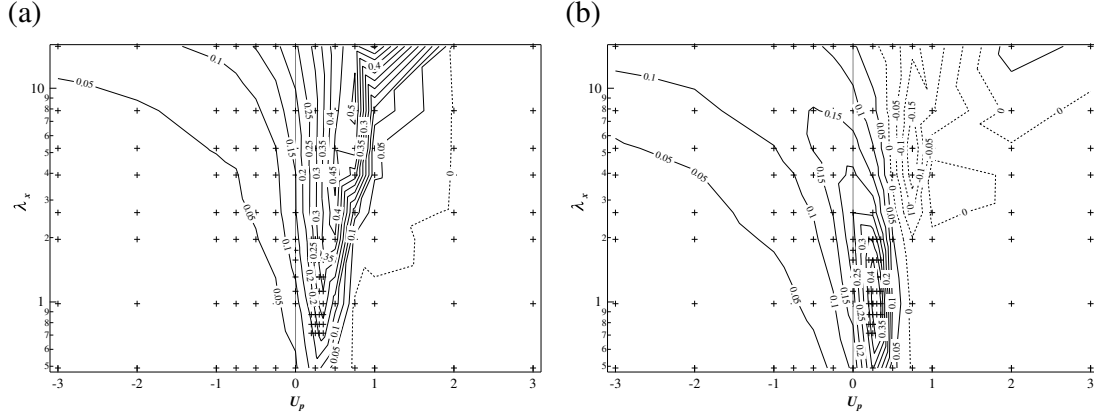


Figure 3.13 Contributions of (a) coherent and (b) random components to the analogy factor. Contours with a value less than or equal to 0 are shown using dashed lines.

(3.13):

$$\begin{aligned}
 D \equiv 2St - C_f &= 3 \int_{-1}^1 y \tilde{v} (\tilde{\theta} - \tilde{u}) dy + 3 \int_{-1}^1 y v'' (\theta'' - u'') dy \\
 &= D^C + D^R.
 \end{aligned} \tag{3.16}$$

Accordingly, the analogy factor  $A$  is related to  $D$  as follows

$$\begin{aligned}
 A &= 1 + \frac{D}{C_f} \\
 &= 1 + \frac{D^C}{C_f} + \frac{D^R}{C_f},
 \end{aligned} \tag{3.17}$$

where  $D^C/C_f$  and  $D^R/C_f$  represent the contributions of the coherent and random components to the dissimilarity, and are shown in figures 3.13(a) and 3.13(b), respectively. From figure 3.13(a), it can be confirmed that the coherent contribution becomes large for  $0 < U_p < 1.0$  and increases with increasing  $\lambda_x$ . In contrast, the random contribution shown in figure 3.13(b) has a positive peak at  $(\lambda_x, U_p) = (1.31, 0.35)$ , and this location is closer to the global optimum  $(\lambda_x, U_p) = (1.12, 0.30)$  for  $A$  shown in figure 3.5.

At the globally optimal condition for  $A$ , i.e.  $(\lambda_x, U_p) = (1.12, 0.30)$ , the coherent contribution  $D^C$  accounts only for 38% of the total dissimilarity  $D$ , whereas the rest of the 62% comes from the random component  $D^R$ . This is surprising considering the fact that the present control directly induces the coherent fluctuation, whereas the random fluctuation



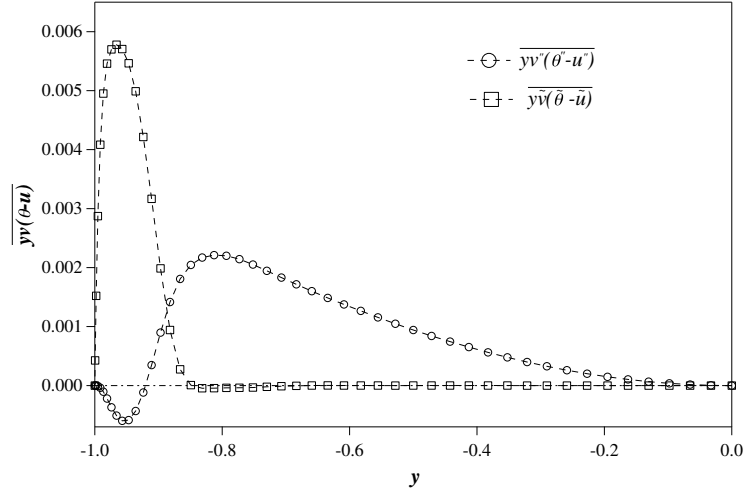


Figure 3.14 Wall-normal distributions of the integrands of the coherent and random contributions to dissimilarity (refer equation (3.16)).

feels the control input only through the interaction with the induced coherent fluctuation. The present results indicate that such indirect effects on the random component cause significant dissimilarity.

To understand the mechanism of dissimilarity in detail, we focus on the global optimal combination of  $(\lambda_x, U_p) = (1.12, 0.30)$  for further analyses. As the first step, the integrands in equation (3.16), i.e.  $y\tilde{v}(\tilde{\theta} - \tilde{u})$  and  $yv''(\theta'' - u'')$ , are plotted as a function of  $y$  for the lower half of the channel in figure 3.14. The coherent component has a positive contribution only for  $|y| \gtrsim 0.80$ . This means that the direct influence of the control input is confined to a region close to the wall. On the other hand, the random component has a negative contribution near the wall ( $|y| \gtrsim 0.90$ ) and a positive contribution away from the wall  $|y| \lesssim 0.90$ . In the following sections, we discuss the origins of the coherent and random contributions in more detail.

### 3.3.3 Coherent contribution for the globally optimal control input

The 2D distribution of the coherent contribution to dissimilarity, i.e.  $\langle y\tilde{v}(\tilde{\theta} - \tilde{u}) \rangle$ , in the  $\xi - y$  plane, is shown in figure 3.15. Note that integration of figure 3.15 in  $\xi$  direction exactly reduces to the  $y$ -distribution of the coherent contribution, i.e.  $y\tilde{v}(\tilde{\theta} - \tilde{u})$ , shown in figure 3.14. Figure 3.15 confirms that the coherent contribution is confined in the region close to the wall, but now its distribution in  $\xi$  and its phase relationship with the control input can be clearly

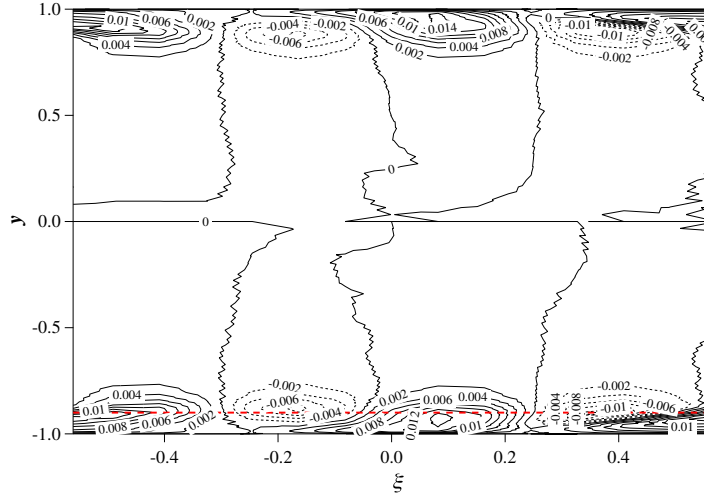


Figure 3.15  $\xi - y$  distribution of coherent contribution  $\langle y\tilde{v}(\tilde{\theta} - \tilde{u}) \rangle$ . The red dashed line indicates the location of  $y = -0.90$ , where the coherent contribution has a positive peak. Contours with a value less than 0 are shown using dashed lines.

observed. A large positive contribution within  $\Delta y = 0.1$  from the wall (indicated by the region below the red line) is consistent with figure 3.14. Although large positive and negative values exist slightly away from the wall ( $|y| < 0.90$ ) in figure 3.15, they almost cancel out each other so that their net contribution is nearly zero (see, figure 3.14). Closer look at the near wall region ( $|y| > 0.9$ ) reveals that the positive contours are distorted upstream, i.e., in the negative  $\xi$  direction. We remind that the current reference frame  $\xi - y$  is moving with the downstream traveling wave of  $U_p = 0.3$ , and therefore the wall is moving in the negative  $\xi$  direction in the current frame. As a result, the positive contours induced around the suction region ( $\xi \sim 0$ ) is dragged below the negative contours upstream. This results in the dominant positive peak in the coherent contribution shown in figure 3.14.

The contour plot of the coherent components:  $\tilde{u}$ ,  $\tilde{\theta}$ ,  $\tilde{v}$ ,  $\tilde{p}$ , and  $(\tilde{\theta} - \tilde{u})$ , in the  $\xi - y$  plane, are plotted in figure 3.16. Even though the governing equations and boundary conditions are similar, the contour plot of  $\tilde{\theta}$  and  $\tilde{u}$  are quite different as can be seen from figures 3.16(a) and 3.16(b). To highlight this, their difference  $(\tilde{\theta} - \tilde{u})$  is plotted in figure 3.16(c). Note that multiplying  $(\tilde{\theta} - \tilde{u})$  with  $\tilde{v}$  in figure 3.16(d) and  $y$  reproduces the contours of  $y\tilde{v}(\tilde{\theta} - \tilde{u})$  shown in figure 3.15.

In order to explain the distribution of  $\tilde{\theta}$  shown in figure 3.16(a), an enlarged view of  $\tilde{\theta}$  with phase-averaged velocity field,  $(\langle u \rangle - U_p, \tilde{v})$ , is shown in figure 3.17 for the near wall region. Since the frame is moving with the applied traveling wave, we subtract the phase-

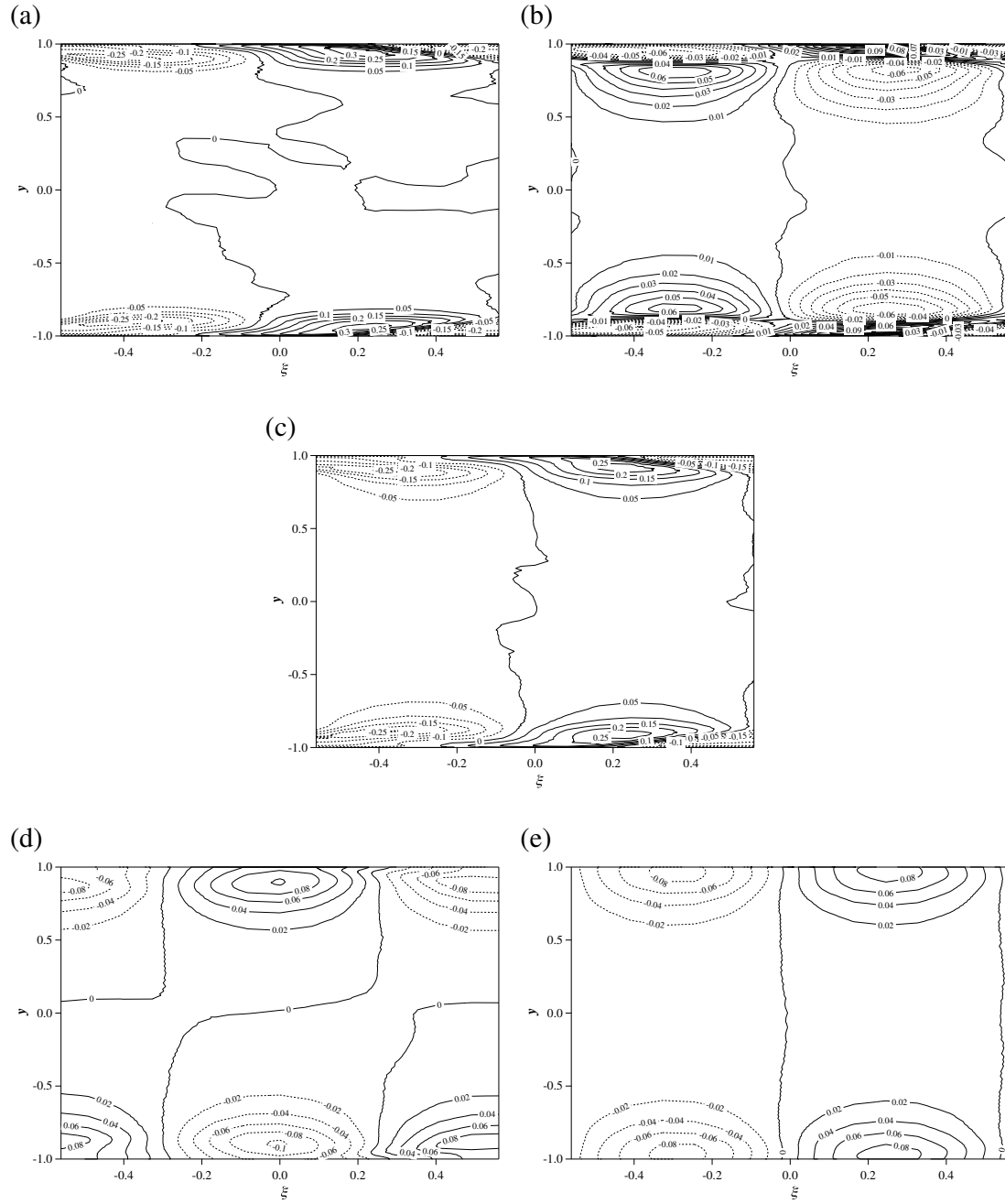


Figure 3.16 Contour plots of the coherent components: (a)  $\tilde{\theta}$ , (b)  $\tilde{u}$ , (c)  $\tilde{\theta} - \tilde{u}$ , (d)  $\tilde{v}$ , and (e)  $\tilde{p}$ . Contours with a value less than 0 are shown using dashed lines.

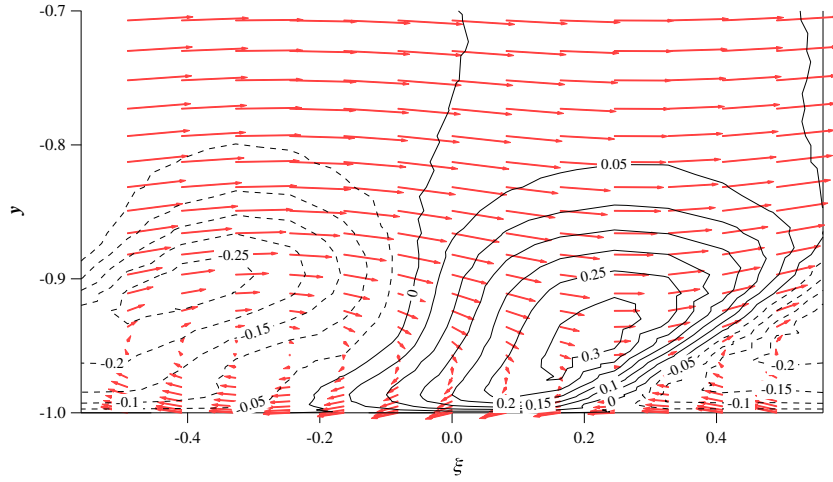


Figure 3.17 Enlarged view of  $\tilde{\theta}$  in the near wall region. The vectors show the phase-averaged velocity field  $(\langle u \rangle - 0.30, \tilde{v})$ . Contours with a value less than 0 are shown using dashed lines.

speed from the phase-averaged streamwise velocity to show the relative velocity. We can identify three characteristic features in figure 3.17. First, in the near-wall region of  $|y| > 0.90$ , the downwelling motion due to wall suction around  $\xi = 0$  brings high-temperature fluid toward the wall, resulting in positive  $\tilde{\theta}$  contours, and the opposite happens near the blowing regions around  $\xi = \pm 0.56$ . Second, the convection outside the near wall region,  $|y| < 0.90$  transports the temperature fluctuation  $\tilde{\theta}$  downstream. Third, the wall movement at the speed of  $-U_p$  drag  $\tilde{\theta}$  upstream due to the viscous effect in the near-wall region of  $|y| > 0.90$ .

Next, we consider the contour plot of  $\tilde{u}$  is shown in figure 3.16(b). Although  $\tilde{u}$  is similar to  $\tilde{\theta}$  shown in figure 3.16(a) in the vicinity from the wall, it shows large fluctuations with the opposite sign away from the wall. This distinct difference between  $\tilde{\theta}$  and  $\tilde{u}$  can be explained by the pressure gradient term present only in the governing equation for  $\tilde{u}$  (see equations (C.4) and (C.5) in Appendix C). The wall blowing around  $\xi = \pm 0.56$  causes a favourable pressure gradient, whereas the wall suction around  $\xi = 0$  results in an adverse pressure gradient (see figure 3.16(e)). The induced coherent pressure gradient only affects the dynamics of  $\tilde{u}$ , and therefore creates significant dissimilarity between  $\tilde{\theta}$  and  $\tilde{u}$ . The current results indicate that the coherent contribution is caused by the combined effects of the following two mechanisms. First, the continuity constraint, i.e., the pressure fluctuation, modifies only the dynamics of  $\tilde{u}$ , so that it causes the dissimilarity between  $\tilde{\theta}$  and  $\tilde{u}$ . Second, the induced dissimilarity  $(\tilde{\theta} - \tilde{u})$  is dragged into the near-wall region due to fluid viscosity, and this generates the coherent contribution,  $\langle y\tilde{v}(\tilde{\theta} - \tilde{u}) \rangle$ , through interaction with  $\tilde{v}$  induced by the control input.

The above two mechanisms become further apparent from the budget of the coherent contribution, i.e.,  $-\tilde{v}(\tilde{\theta} - \tilde{u})$ , (see equation (C.16) and its detailed derivation in appendix C.2):

$$\begin{aligned}
0 = & \underbrace{\frac{\overline{\tilde{v}^2} \partial(\tilde{\theta} - \tilde{u})}{\partial y}}_{P_C} \underbrace{- \overline{u_j'' v''} \frac{\partial(\tilde{\theta} - \tilde{u})}{\partial x_j}}_{P_{C1_C}} \underbrace{- \overline{\{u_j''(\theta'' - u'')\}} \frac{\partial \tilde{v}}{\partial x_j}}_{P_{C2_C}} \\
& + \underbrace{\frac{\partial}{\partial y} \left[ (\tilde{\theta} - \tilde{u}) \overline{v'' v''} + \tilde{v} \overline{v'' (\theta'' - u'')} \right]}_{T_{D_C}} \underbrace{- \frac{1}{Re} \frac{\partial}{\partial y} \left[ \frac{\partial \tilde{v}(\tilde{\theta} - \tilde{u})}{\partial y} \right]}_{V_{D_C}} \\
& - \underbrace{\left\{ -(\tilde{\theta} - \tilde{u}) \frac{\partial \tilde{p}}{\partial y} + \tilde{v} \frac{\partial \tilde{p}}{\partial x} \right\}}_{\Pi_C} \\
& + \underbrace{\frac{2}{Re} \frac{\partial \tilde{v}}{\partial x_j} \frac{\partial(\tilde{\theta} - \tilde{u})}{\partial x_j}}_{\varepsilon_C}.
\end{aligned} \tag{3.18}$$

The first three terms in the first line on the RHS represent the production (termed as  $P_C$ ,  $P_{C1_C}$ , and  $P_{C2_C}$ ). The second line corresponds to turbulent and molecular diffusion (denoted as  $T_{D_C}$  and  $V_{D_C}$ ), whereas the third line is the correlation between velocity/temperature fluctuation and pressure gradient ( $\Pi_C$ ). The final term represents the molecular dissipation ( $\varepsilon_C$ ). Here, the subscript  $C$  indicates the budget terms of the coherent contribution. It will be shown that the last two production terms (i.e.  $P_{C1_C}$  and  $P_{C2_C}$ ) also appear in the budget equation of the random contribution, i.e.  $-\overline{v''(\theta'' - u'')}$ , but with the opposite sign (see equation (3.19)). Therefore, they represent the exchange between the coherent and random contributions and are referred to as the coupling terms hereafter.

Each term in the budget equation for  $-\tilde{v}\tilde{u}$ ,  $-\tilde{v}\tilde{\theta}$ , and  $-\tilde{v}(\tilde{\theta} - \tilde{u})$  is plotted in figure 3.18. The plot of  $-\tilde{v}(\tilde{\theta} - \tilde{u})$  shown in figure 3.18c indicates that  $\Pi_C$  and  $P_C$  act as the dominant positive and negative terms in the near wall region,  $-0.97 < y < -0.90$ , respectively. Here, we remind that the pressure fluctuation is a primary factor causing dissimilarity in the coherent field. This can be confirmed by a dominant positive value of  $\Pi_C$  in the near-wall region,  $y < -0.90$ , where the coherent contribution becomes significant (see, figure 3.14). Slightly away from the wall beyond  $y = -0.90$ ,  $\Pi_C$  and  $P_C$  are still dominant, but change their signs. Further away from the wall ( $y \gtrsim -0.80$ ), all budget terms decay and this also agrees with the decay of the coherent contribution in figure 3.14. In the immediate

vicinity from the wall, *i.e.*  $y < -0.97$  ( $y^+ < 5$ ), the contribution from the molecular diffusion becomes significant; in fact for  $y^+ < 5$  the positive contribution from  $\Pi_C$ ,  $P_C$ , and  $T_{D_C}$  are balanced solely by  $V_{D_C}$ . So, even though viscous dissipation is minor through out the channel, viscosity plays a crucial role in the dissimilar heat transfer process very close to the wall. Finally, we note that the coupling terms, *i.e.*,  $P_{C1_C}$ , and  $P_{C2_C}$ , are generally quite small within the entire region, suggesting that the direct interaction between the coherent and random components is relatively weak.

### 3.3.4 Random contribution for the globally optimal control input

In figure 3.14, there exist two distinct peaks in the plot of random contribution to dissimilarity, *i.e.*  $yv''(\theta'' - u'')$ , close to the wall. One positive peak at  $y_p = -0.81$  ( $y^+ = 28.08$  from the bottom wall) and one negative peak at  $y_n = -0.96$  ( $y^+ = 6.47$ ). In order to understand its generation mechanisms, we consider the following budget equation for  $-\overline{v''(\theta'' - u'')}$  (see equation (C.17) and its detailed derivation in appendix C.3):

$$\begin{aligned}
 0 = & \underbrace{\overline{v''^2 \frac{\partial(\tilde{\theta} - \tilde{u})}{\partial y}}}_{P_R} + \underbrace{\overline{u_j'' v'' \frac{\partial(\tilde{\theta} - \tilde{u})}{\partial x_j}}}_{P_{C1_R}} + \underbrace{\overline{u_j'' (\theta'' - u'') \frac{\partial \tilde{v}}{\partial x_j}}}_{P_{C2_R}} \\
 & + \underbrace{\frac{\partial}{\partial y} \left[ \overline{\tilde{v} \{v''(\theta'' - u'')\}} + \overline{v'' v'' (\theta'' - u'')} \right]}_{T_{D_R}} + \underbrace{\frac{1}{Re} \frac{\partial}{\partial y} \left[ \overline{\frac{\partial v'' (\theta'' - u'')}{\partial y}} \right]}_{V_{D_R}} \\
 & - \underbrace{\left\{ -(\theta'' - u'') \frac{\partial p''}{\partial y} + v'' \frac{\partial p''}{\partial x} \right\}}_{\Pi_R} \\
 & + \underbrace{\frac{2}{Re} \frac{\partial v''}{\partial x_j} \frac{\partial (\theta'' - u'')}{\partial x_j}}_{\varepsilon_R}. \tag{3.19}
 \end{aligned}$$

Similar to equation (3.18), the first three terms, *i.e.*,  $P_R$ ,  $P_{C1_R}$ , and  $P_{C2_R}$ , in the first line on the RHS represent the production. The second line corresponds to turbulent and molecular diffusion (denoted as  $T_{D_R}$  and  $V_{D_R}$ ), whereas the third line is the correlation between velocity/temperature fluctuation and pressure gradient ( $\Pi_R$ ). The final term represents the molecular dissipation ( $\varepsilon_R$ ). Here, the subscript  $R$  indicates the budget terms of the random contribution.

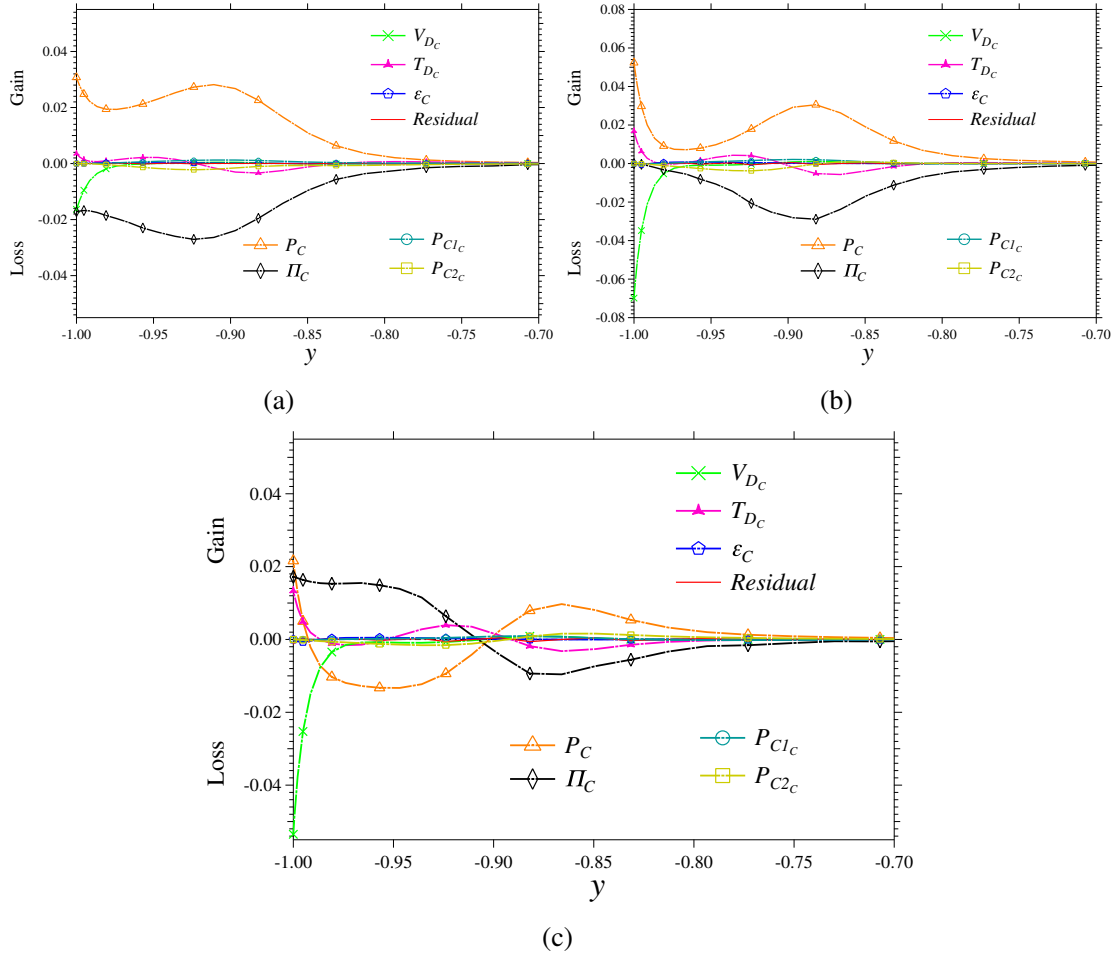


Figure 3.18 Terms in the budget equation for (a)  $-\tilde{v}\tilde{u}$ , (b)  $-\tilde{v}\tilde{\theta}$ , and (c)  $-\tilde{v}(\tilde{\theta} - \tilde{u})$ .  $P_c$  = production;  $P_{C1_c}$  &  $P_{C2_c}$  = coupling terms;  $T_{D_c}$  &  $V_{D_c}$  = turbulent and molecular diffusion;  $\Pi_c$  = correlation between velocity/temperature fluctuation and pressure gradient;  $\epsilon_c$  = molecular dissipation.

In figure 3.19, all the budget terms in equation (3.19) are plotted along with that of  $-\overline{v''u''}$  and  $-\overline{v''\theta''}$ . The term  $P_R$  represents a source term through the interaction of the mean component with the random component, and is found to be the most dominant term. Also, their positive and negative peaks agree well with those observed in the profile of the random contribution (see, figure 3.14). Since  $\overline{v''^2}$  is always positive, the sign of  $P_R$  is determined by the sign of  $d(\bar{\theta} - \bar{u})/dy$ . The variation of  $d(\bar{\theta} - \bar{u})/dy$  along the lower half of the channel is plotted in figure 3.20. It is found that the profile of  $d(\bar{\theta} - \bar{u})/dy$  changes its sign between the peak locations  $y_p$  and  $y_n$ , and this explains why the sign of the random contribution changes in figure 3.14. It should be noted that the mechanisms of the random contribution is in contrast to those of the coherent contribution, where the correlation term between velocity/temperature and pressure gradient,  $\Pi_C$ , is dominant.

As mentioned in the previous subsection, the coupling terms  $P_{C1_R}$  and  $P_{C2_R}$  have exactly the same form as  $P_{C1_C}$  and  $P_{C2_C}$  in equation (3.18) but with opposite signs, indicating that they represent direct interaction between the coherent and random contributions. In general, they have minor contributions throughout the domain as shown in figure 3.19. It should be noted, however, that they have the opposite sign to  $P_R$ , indicating that the random contribution generated by  $P_R$  are transported to the coherent contribution through  $P_{C1_R}$  and  $P_{C2_R}$ .

The distribution of  $\langle y(\theta''v'' - u''v'') \rangle$  in the  $\xi - y$  plane is shown in figure 3.21. The integration of the plotted quantity in  $\xi$  gives the distribution of the random contribution as a function of  $y$  presented in figure 3.14. The red dash-dotted and blue dashed lines corresponds to the negative and positive peaks of the random contribution, i.e.,  $y = y_n$  and  $y_p$  near the bottom wall, respectively. Strong negative contours are confirmed around  $y = y_n$ , where  $yv''(\theta'' - u'')$  shown in figure 3.14 also has a negative peak. The negative contours are particularly concentrated around the suction region, i.e.  $\xi \sim 0$ . Meanwhile, positive contours exist slightly away from the wall above wall blowing region ( $\xi \sim \pm 0.56$ ), and this location also agrees with the positive peak location of the random contribution shown in figure 3.14.

For further analyses of the random contribution, we express the momentum and heat transfer of the random fields with the eddy viscosity and diffusivity, i.e.  $E_v''$  and  $E_d''$ , which are respectively defined as

$$\langle -v''u'' \rangle = E_v'' \frac{\partial \langle u \rangle}{\partial y}, \quad (3.20)$$

$$\langle -v''\theta'' \rangle = E_d'' \frac{\partial \langle \theta \rangle}{\partial y}, \quad (3.21)$$



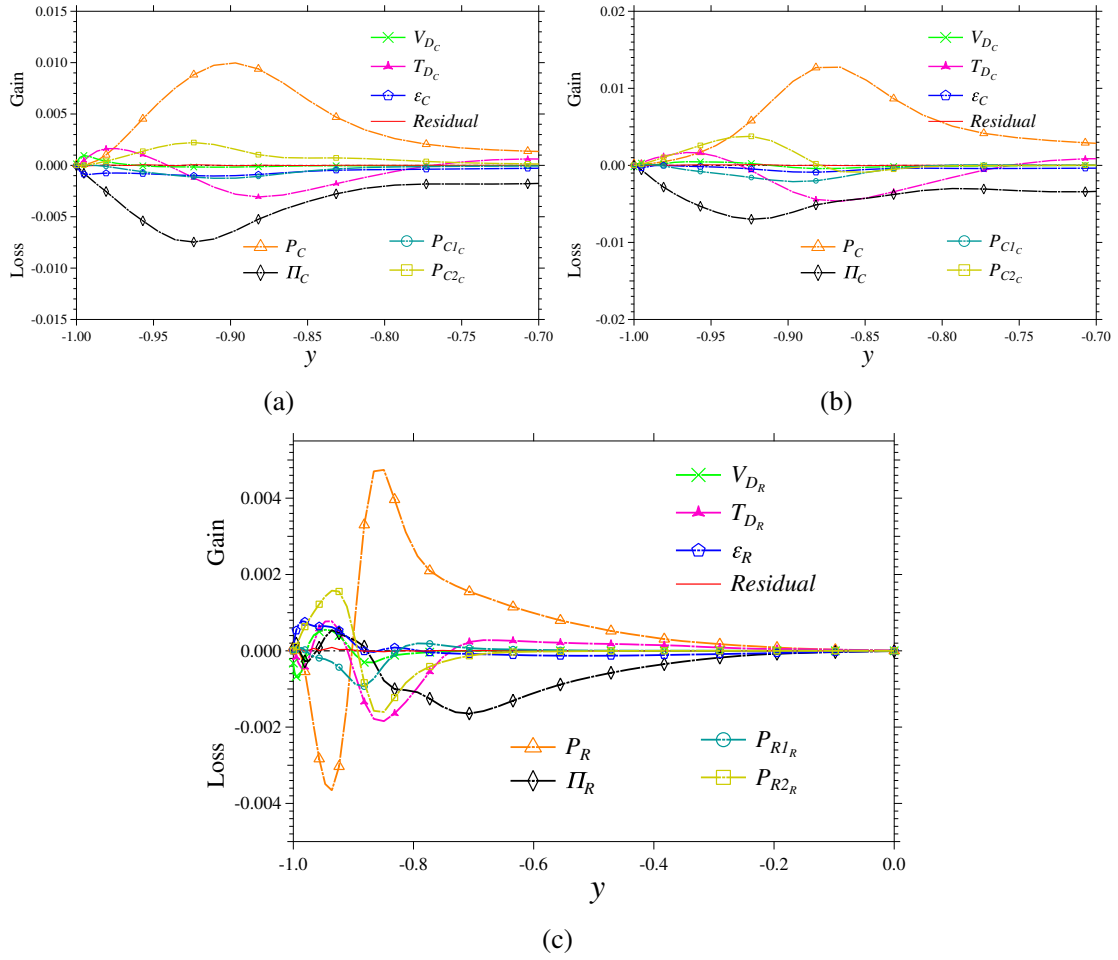


Figure 3.19 Terms in the budget equation for (a)  $-\overline{v''u''}$ , (b)  $-\overline{v''\theta''}$ , and (c)  $-\overline{v''(\theta'' - u'')}$ .  $P_R$  = production;  $P_{C1R}$  &  $P_{C2R}$  = coupling terms;  $T_{D_R}$  &  $V_{D_R}$  = turbulent and molecular diffusion;  $\Pi_R$  = correlation between velocity/temperature fluctuation and pressure gradient;  $\epsilon_R$  = molecular dissipation.

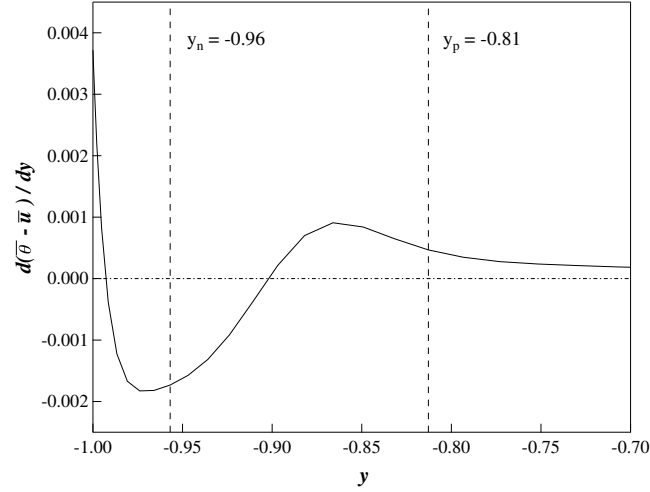


Figure 3.20 Gradient of the difference between the mean temperature and velocity along the lower half of the channel.  $y_p = -0.96$  and  $y_n = -0.81$  correspond to the locations where the random contribution to dissimilarity have positive and negative peaks, respectively

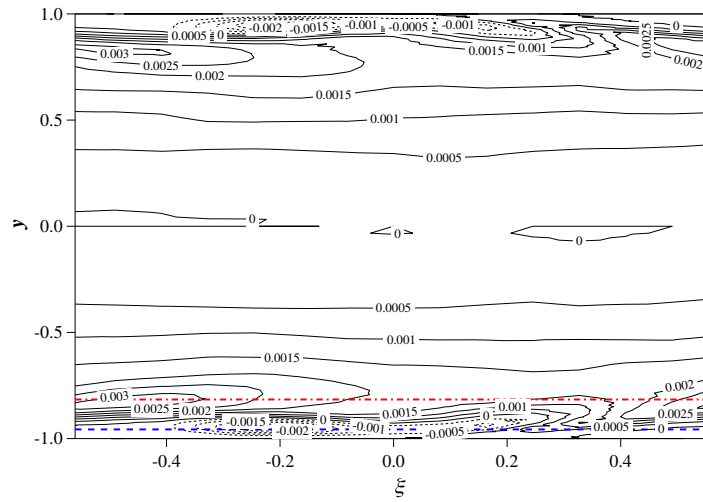


Figure 3.21  $\xi - y$  distribution of the random contribution  $\langle y(\theta''v'' - u''v'') \rangle$ . The dash-dotted line (red) and dashed (blue) line represent the location of  $y_p = -0.81$  and  $y_n = -0.96$  where the random contribution to dissimilarity have positive and negative peaks, respectively. Contours with a value less than 0 are shown using dashed lines.

where  $E_v''$  and  $E_d''$  are functions of  $\xi$  and  $y$ . Accordingly, the random contribution can be rewritten as

$$\begin{aligned}\langle -v''(\theta'' - u'') \rangle &= \left( E_d'' \frac{\partial \langle \theta \rangle}{\partial y} - E_v'' \frac{\partial \langle u \rangle}{\partial y} \right), \\ &= E_v'' \frac{\partial \langle u \rangle}{\partial y} \left( \frac{E_d''}{E_v''} \frac{\partial \langle \theta \rangle}{\partial y} / \frac{\partial \langle u \rangle}{\partial y} - 1 \right), \\ &= E_v'' \frac{\partial \langle u \rangle}{\partial y} \left( Pr_t''^{-1} S - 1 \right),\end{aligned}\tag{3.22}$$

where the turbulent Prandtl number for the random field is defined as

$$Pr_t'' = \frac{E_v''}{E_d''},\tag{3.23}$$

and the ratio of the wall-normal gradients of the phase-averaged velocity and temperature fields is given by

$$S = \frac{d\langle \theta \rangle / dy}{d\langle u \rangle / dy}.\tag{3.24}$$

If the analogy between the velocity and thermal fields holds well, it is expected that both  $S$  and  $Pr_t''$  are close to unity. In such a case, equation (3.22) indicates that the random contribution should also vanish. Meanwhile, when either  $S$  or  $Pr_t''$  deviates from unity, the random contribution becomes non-zero. In figures 3.22(a) and 3.22(b),  $S$  and  $Pr_t''^{-1}$  are plotted in the  $\xi - y$  plane, respectively. Again, the vertical locations of  $y_n$  and  $y_p$  are depicted by the dash-dotted red line and the dashed blue line, respectively. From the comparison of figures 3.22(a) and 3.22(b), the concentrated negative and positive contours in figure 3.21 are strongly correlated with  $S$  rather than  $Pr_t''^{-1}$ . Considering the definition of  $S$  given in (3.24), the random contribution is mainly caused by the dissimilarity between the phase-averaged velocity and temperature fields. If one refers to the coherent contribution discussed in § 3.3.3 to the direct effect, the random contribution can be viewed as the indirect effect, since it is associated with the changes in the phase-averaged fields.

An instantaneous snapshot of the bottom half of the channel in the  $y - z$  plane at  $\xi = 0$  is shown in figure 3.23. An enlarged view of near-wall region is shown in the bottom figure. The colour represents the the random contribution  $yv''(\theta'' - u'')$ , and the random velocity vectors are also shown with arrows. The statistical features shown so far can also be confirmed in an instantaneous field. Specifically, the random component tends to have negative values

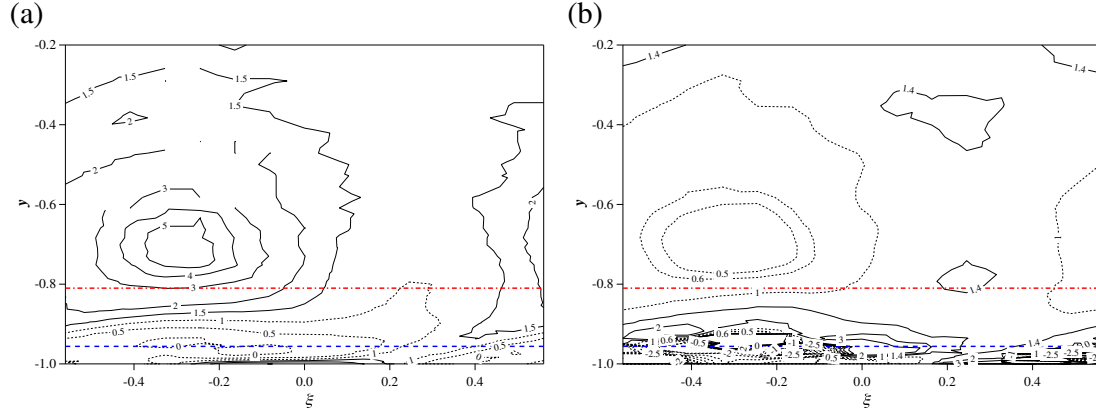


Figure 3.22 a) The ratio of the wall-normal gradients of the phase-averaged temperature and velocity fields,  $S$ , and b) the inverse of the turbulent Prandtl number for the random component,  $(Pr_t'')^{-1}$ . The red dash-dotted and blue dashed lines represent the locations of  $y_p = -0.81$  and  $y_n = -0.96$  where the random contribution to dissimilarity have positive and negative peaks, respectively. Contours with a value less than or equal to 1 are shown using dashed lines.

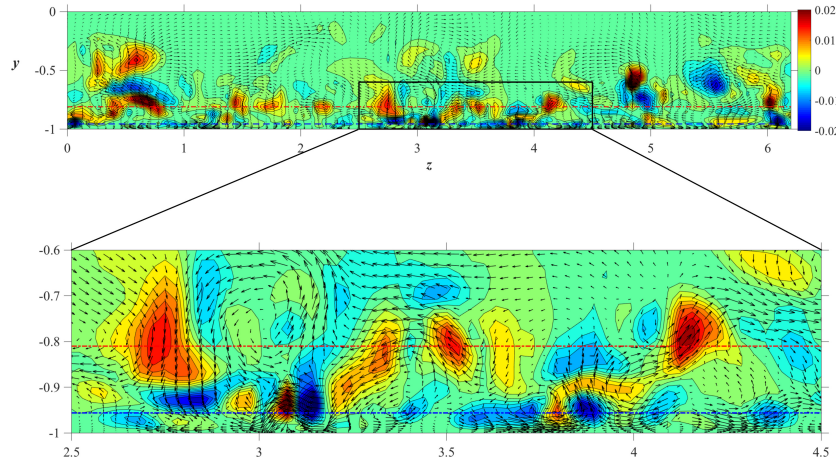


Figure 3.23 Instantaneous distribution of the random contribution  $yv''(\theta'' - u'')$  in the bottom half of the channel at  $\xi = 0$ . The enlarged view of the near-wall region is shown in the bottom figure. The vectors show the random velocity components  $(v'', w'')$ . The red dash-dotted and blue dashed lines represent the locations of  $y_p = -0.81$  and  $y_n = -0.96$  where the random contribution to dissimilarity have positive and negative peaks, respectively.

around the blue horizontal line which corresponds to the negative peak location of the random contribution shown in figure 3.14, whereas positive regions occur relatively away from the wall and they distribute around the red line corresponding to the positive peak location in figure 3.14. These negative and positive random contributions are mostly associated with either strong downwelling or upwelling motions. This is again consistent with the first production term in the budget equation (C.17) of the random contributions.

### 3.3.5 Visualization of the turbulence structures

In order to discuss the relationship between near-wall turbulent structures and the coherent and random contributions, instantaneous flow fields in the uncontrolled and controlled flows are shown in figure 3.24. Here, the  $Q$  criterion defined as  $Q = -\partial u_i / \partial x_j \partial u_j / \partial x_i$  (Hunt et al., 1988) is used to visualize vortex cores.

Comparison between the top and bottom figures of figure 3.24 reveals two distinct features of the controlled flow. First, there exist spanwise rollers which is directly induced by wall blowing/suction. The spanwise rolls exist below  $y^+ = 15$ , and agree well with the coherent flow field drawn by vectors in figure 3.17. Second, above the spanwise rollers, there exists quasi-streamwise vortices similar to those in the uncontrolled flow, but with finer length-scale. As far as we observed the temporal evolution of the turbulent structures, there is no clear evidence that the coherent spanwise rolls and the quasi-streamwise interact directly. Rather, the quasi-streamwise vortices emerge and breakdown almost in a irrelevant manner to the spanwise rolls. Spanwise two-point correlations of the random velocity fluctuations  $u''$  and  $v''$  indicate that the spanwise distances of the negative peaks are almost unchanged when they are normalized by the wall unit based on the actual wall shear. These results suggest that the modification of near-wall turbulent structures due to the globally optimal control input is mainly caused by the change of averaged wall shear, rather than the direct interaction between the coherent and random fields. This is also consistent with the budget analyses in the previous subsections.

Quasi-streamwise vortices induce  $v''$ , and therefore produce the random contribution through  $P_R = \overline{v''^2} \partial (\bar{\theta} - \bar{u}) / \partial y$  according to the budget equation (3.19) for the random contribution. It can be confirmed in figure 3.25, where the iso-surfaces of the positive and negative random contributions are drawn by red and blue together with the iso-surface of  $Q^+$  shown by white. It can be confirmed that the random contributions wrap around quasi-streamwise vortices. Positive random contributions (red) are prominent away from the wall, whereas negative contributions (blue) are clustering around the legs of quasi-streamwise

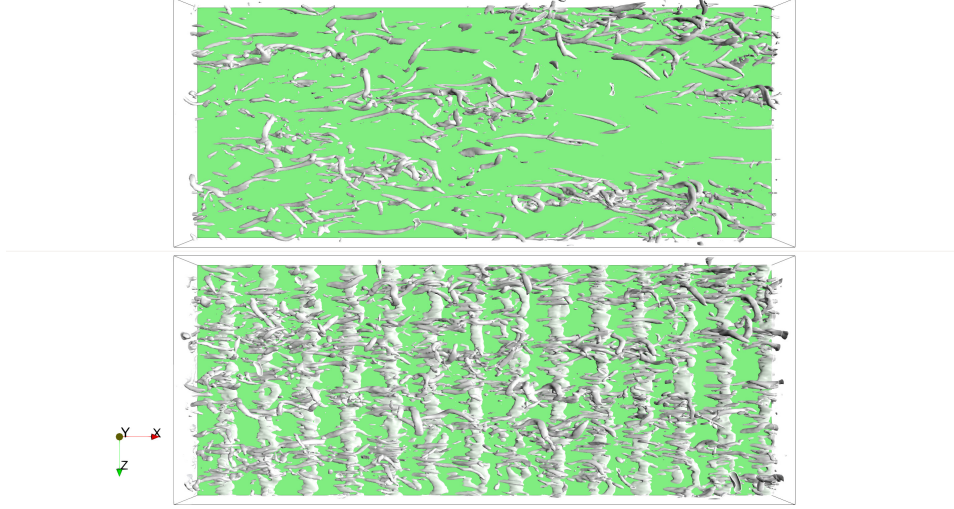


Figure 3.24 Top view of the isosurfaces of  $Q^+ = -0.03$  for the uncontrolled (*top*) and controlled (*bottom*) (for the optimal case) channel flow at  $Re_\tau = 150$ .

vortices near the wall. These results are consistent with the positive and negative peaks in the profile of the random contribution shown in figure 3.14 and also the two-dimensional visualization shown in figure 3.23.

### 3.4 Discussions

The present results indicate that the performance of dissimilar control is determined as a result of the complex responses of coherent and random fields to the traveling wave-like wall blowing and suction. Considering the complexity of the phenomena, it is rather surprising that the optimal control theory predicted the global optimal parameters of the traveling wave fairly well.

One possible reason for its success is that there exist no multiple local maxima in the analogy factor within the parameter range considered in the present study as shown in figure 3.5. Since the optimal control theory iteratively optimizes a control input based on the local gradient of a given cost functional, the resultant control input could be stuck in a local minimum. Hence, the presence of a single minimum/maximum is necessary for a gradient-based optimization to predict the global optimum. Nonetheless, it does not always guarantee the success. As described in chapter 1, the optimal control theory takes into account future flow dynamics within only a limited time horizon ( $T^+ \approx 100$ ), which is much smaller than a period required for a flow field to reach another equilibrium state under a certain control

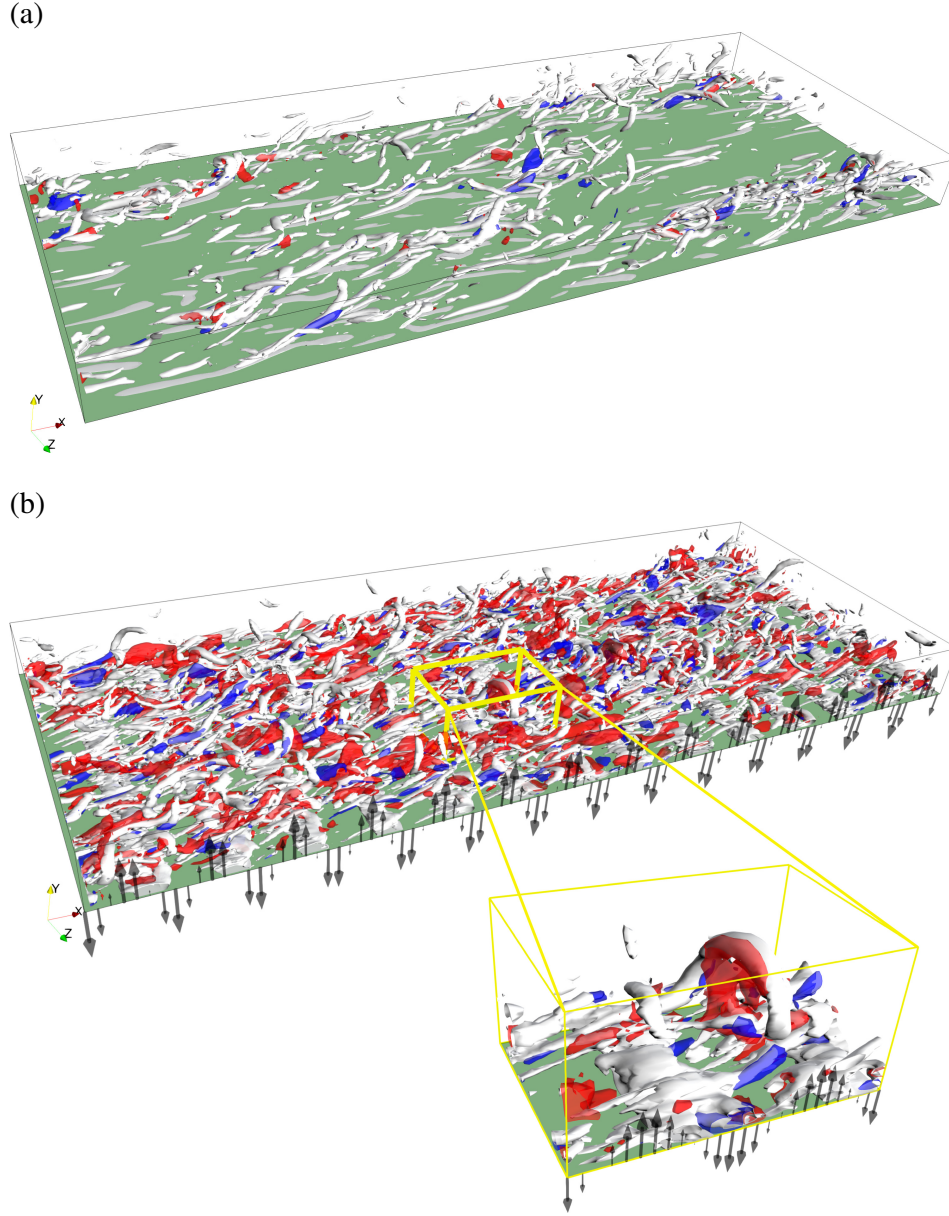


Figure 3.25 Isosurfaces of  $Q^+ = 0.03$  (white),  $yv''(\theta'' - u'') = 0.01$  (red), and  $yv''(\theta'' - u'') = -0.01$  (blue) for the bottom half of (a) uncontrolled flow and (b) controlled flow with the globally optimal input at  $Re_\tau = 150$ . The arrows in the controlled case represents wall blowing and suction which is uniform in the spanwise direction.



input. In order to fill the temporal gap, a time-division technique is commonly used. Namely, once the control input converges in a given time horizon, the time horizon is advanced in time and new optimization procedures are conducted (Bewley et al., 2001; Yamamoto et al., 2013). These processes will be repeated until multiple time horizons cover a sufficiently long period, so that the controlled flow eventually reaches to a statistically equilibrium state.

A key feature of the present control input is a traveling wave-like property. When observed from a frame moving with the applied control input, the resultant phase-averaged velocity and thermal fields become steady as shown in § 3.3. Therefore, as far as the phase-averaged velocity and thermal fields are concerned, the problem reduces to the optimization of a steady flow. In such a case, even though each time horizon is relatively short, it could be possible that the control input eventually approaches to the global optimum by sequentially repeating the optimization procedure for a long period.

Meanwhile, the coherent velocity and thermal fields are not solely determined by the control input, but also interact with the random field as can be seen in the governing equations for the coherent field (see equations (C.4)–(C.6)). Such non-linear interactions are generally slow processes, so that a sufficiently long time horizon should be necessary in order to correctly take into account their effects in the optimization procedures. In addition, the present DNS results indicate that the random contribution to dissimilarity is more significant than that due to the coherent contribution. These facts suggest that predicting the globally optimal mode by the optimal control theory should be quite challenging.

According to the present results in § 3.3.5, however, the random contribution to dissimilar heat transfer enhancement is mostly caused by the dissimilarity between the phase-averaged velocity and thermal fields (more specifically, the ratio of their wall-normal gradients,  $S$ ) rather than the variation of the turbulent Prandtl number. This means that the local similarity between momentum and heat transfer still holds well even in the controlled flow, and the distributions of the phase-averaged velocity and thermal fields govern not only the coherent contribution, but also the random contribution. This could be a reason why the optimal control theory with a limited time horizon still provides a good prediction of the globally optimal traveling wave properties.

The above discussions motivate us to propose a simple approach where only the phase-averaged velocity and thermal fields are directly solved, while the effects of the random field are represented by eddy viscosity and eddy diffusivity models. In order to demonstrate such a possibility, we consider the following equations for the phase-averaged velocity and thermal fields:

$$\frac{\partial \langle u_i \rangle}{\partial x_i} = 0, \quad (3.25a)$$



$$\frac{\partial \langle u_i \rangle}{\partial t} + \frac{\partial (\langle u_j \rangle \langle u_i \rangle)}{\partial x_j} = -\frac{\partial \langle p \rangle}{\partial x_i} + \frac{\partial}{\partial x_j} \left\{ \left( \frac{1}{Re} + E_v'' \right) \left( \frac{\partial \langle u_i \rangle}{\partial x_j} + \frac{\partial \langle u_j \rangle}{\partial x_i} \right) \right\}, \quad (3.25b)$$

$$\frac{\partial \langle \theta \rangle}{\partial t} + \frac{\partial (\langle u_j \rangle \langle \theta \rangle)}{\partial x_j} = Q + \frac{\partial}{\partial x_j} \left\{ \left( \frac{1}{Pe} + E_d'' \right) \frac{\partial \langle \theta \rangle}{\partial x_j} \right\}. \quad (3.25c)$$

Equation (3.25) can be considered as the unsteady Reynolds-averaged Navier-Stokes (URANS) equations for the phase-averaged velocity and thermal fields. In general,  $E_v$  and  $E_d$  in equation (3.25) are functions of space and their distributions depend on an applied control input. Meanwhile, according to the finding in the previous section, the impact of the turbulent Prandtl number on dissimilar heat transfer is relatively weak. Therefore, we assume that  $E_v$  and  $E_d$  are unchanged from the uncontrolled values, and only functions of  $y$ . The vertical profiles of  $E_v$  and  $E_d$  assumed in the present URANS are shown in figure 3.26. The advantage of the present approach is that the profiles of  $E_v$  and  $E_d$  in the uncontrolled flow are relatively easy to obtain.

The URANS equations are numerically solved in a two-dimensional  $\xi - y$  domain. An energy-conservative second-order central difference scheme is used for the spatial discretization and low-storage third-order Runge-Kutta/Crank-Nicolson scheme for the time integration (Kametani and Fukagata, 2011). The streamwise length of the domain is changed accordingly so as to accommodate one wavelength of the control input, whereas the wall-normal length is kept constant and equal to 2. The number of grid points employed in the streamwise and wall-normal directions are  $(N_x, N_y) = (20, 96)$ . The Reynolds and Peclet numbers are set to be identical to those in the present DNS, namely,  $Re = Pe = 2293$ . Since the current URANS only solves the phase-averaged velocity and thermal fields in the two-dimensional domain, it is much cheaper than conducting unsteady three-dimensional DNS.

The contour plot of the analogy factor obtained from the URANS is shown in figure 3.27. A direct comparison with figure 3.5 reveals that the overall trend of the present DNS is well captured by the URANS calculation. Specifically, URANS predicts a large peak around  $U_p = 0.3$  and this agrees well with the present DNS results. Meanwhile, in URANS, the analogy factor increases with increasing the wavelength, so that no global maximum of  $A$  is found. This trend of overestimating the wavelength is also found in the control inputs obtained from the suboptimal and optimal control theories as mentioned before. The present results suggest that inaccurate evaluation of the random contribution overestimates the wavelength of the optimal traveling wave. Although these discrepancies exist, we should rather emphasized that the present URANS succeeds in predicting the overall trend of  $A$  despite its simplicity.

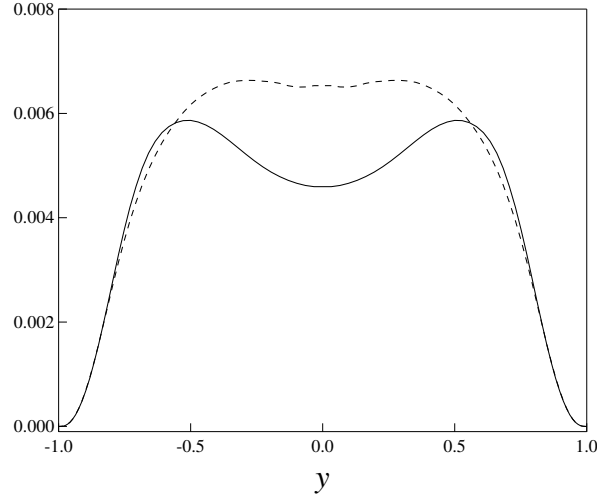


Figure 3.26 Wall-normal distributions of the eddy viscosity  $E_{v0}$  (solid line) and eddy diffusivity  $E_{d0}$  (dashed line) for the uncontrolled flow.

The normalized skin-friction coefficient and Stanton number obtained from the URANS are also shown in figures 3.28 and 3.29. Their strong similarity to those obtained from DNS shown in figures 3.2 and 3.4 are also confirmed. In both DNS and URANS, the values of  $C_f/C_{f0}$  and  $St/St_0$  increases with  $\lambda_x$ . Also, for any particular value of  $\lambda_x$ , the maximum value for  $C_f/C_{f0}$  and  $St/St_0$  occurs between  $0 < U_p < 1.0$  where the critical layer amplifies the fluctuations. Meanwhile, the URANS commonly underestimates both  $C_f/C_{f0}$  and  $St/St_0$ , and this is mainly attributed to the fact that our current eddy viscosity and eddy diffusivity models are assumed to be kept unchanged from the uncontrolled values regardless of an applied control. Indeed, according to the DNS results, both  $E_v''$  and  $E_d''$  are increased when the globally optimal traveling wave is applied (not shown here). Even in such a situation, however, their ratio, i.e., the turbulent Prandtl number, does not deviate from unity significantly, so that hardly contributes to dissimilarity as shown in equation (3.22). As a result, the present URANS can still capture the overall trend of  $A$ .

### 3.5 Conclusions

We conducted a series of DNS of a fully developed channel flow subject to traveling wave-like wall blowing and suction at the bulk Reynolds number of  $Re = 2293$  in order to clarify its impact on the dissimilarity between turbulent momentum and heat transfer. While keeping the wave amplitude constant as 5% of the bulk mean velocity, the wavelength and phase-

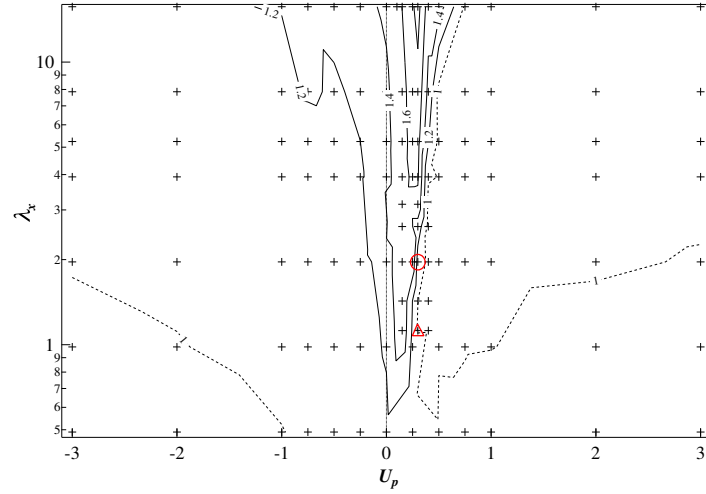


Figure 3.27 Analogy factor  $A$  obtained from URANS simulations. The circle and triangle indicates the control input obtained from the optimal control theory (Yamamoto et al., 2013) and the global optimum obtained in the present DNS, respectively. Contours with a value less than or equal to 1 are shown using dashed lines.

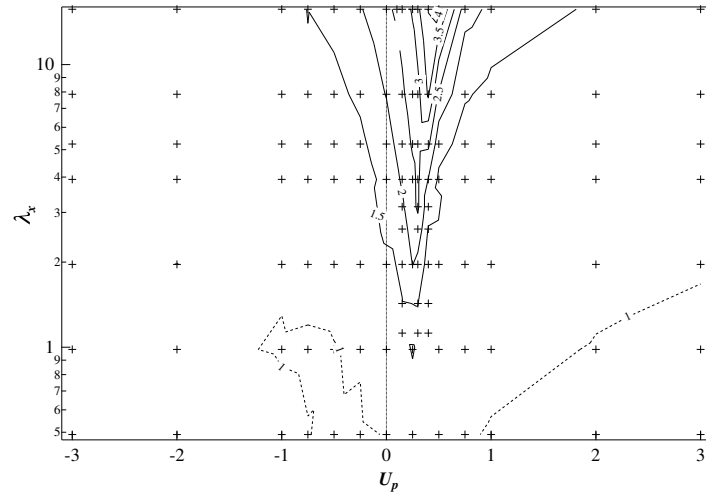


Figure 3.28 Contour plot of  $C_f/C_{f_0}$  obtained from URANS. Contours with a value less than or equal to 1 are shown using dashed lines.

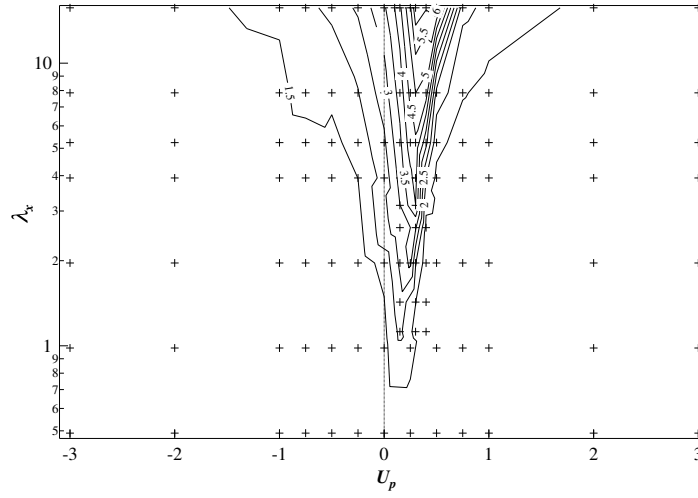


Figure 3.29 Contour plot of  $St/St_0$  obtained from URANS.

speed of the traveling wave were systematically changed in a wide parameter range, i.e.  $5\pi/32 \leq \lambda_x \leq 5\pi$ , and  $-3.0 \leq U_p \leq 3.0$ . As a result, the global optimum of the traveling wave properties for maximising the analogy factor were identified as  $(\lambda_x, U_p) = (1.12, 0.30)$ . Interestingly, they are quite close to  $(\lambda_x, U_p) = (1.96, 0.30)$ , which had been obtained from the optimal control theory under the identical flow configuration by Yamamoto et al. (2013). Another set of parametric survey at the higher Reynolds number of  $Re = 5055$  suggests that the globally optimal control input is well scaled by the wall unit, and the resultant control performance is almost independent of the Reynolds number. However, clarifying the proper scaling of the globally optimal traveling wave and the resultant control performances requires more detailed and careful investigations at further higher Reynolds numbers. This is left for future work.

In order to clarify the mechanisms of dissimilar heat transfer enhancement, the instantaneous velocity and thermal fields were decomposed into mean, coherent, and random components. Based on the FIK identity for the skin-friction coefficient and the Stanton number, the contributions of the coherent and random components to the dissimilarity were quantitatively evaluated. It was found that the random contribution accounts for around 62% of the total contribution, whereas the coherent contribution remains relatively minor. Considering that the response of the random field to the applied control input should generally be a slow process, it is surprising that the optimal control theory taking into account only short-term dynamics can predict the globally optimal control mode.

Further detailed analyses revealed that the dissimilarity in the coherent velocity and thermal fields are caused by the fundamental difference between the divergence-free velocity vector and the conservative scalar. Specifically, the applied wall blowing and suction produce the coherent pressure fluctuation, which modifies the velocity field, while the temperature field is unaffected due to the assumption of a passive scalar. It is found that the generated dissimilarity between  $\tilde{u}$  and  $\tilde{\theta}$  is dragged into the near-wall region due to wall suction, and results in the prominent peak of the coherent contribution to dissimilar heat transfer enhancement. The above results are also supported by the budget analysis of the coherent contribution, which highlights the importance of the pressure fluctuation through the correlation term of velocity/temperature and pressure gradient. Considering the mechanisms of the coherent contributions are mostly linear and therefore rapid processes, their control could be possible within the framework of the optimal control theory.

In contrast, the response of the random field to the applied control input should generally be a slower process, since it is determined as a result of the non-linear interaction with the coherent field. According to the present budget analysis, however, the contribution of the random field to dissimilar heat transfer enhancement is mostly caused by the dissimilarity in the wall-normal gradient of the phase-averaged velocity and thermal field,  $S$ , rather than the dissimilarity in the turbulent Prandtl number,  $Pr_t''$ . This indicates that the local similarity between turbulent heat and momentum transfer holds fairly well even in the controlled flow. Flow visualization indicates that the interaction between the coherent and random field is weak, and modification of near-wall turbulent structures are mostly caused by the change in the mean wall shear due to the applied control input. This motivated us to propose a simple URANS approach in which only the phase-averaged velocity and thermal fields are solved, whereas the effects of the random field are modeled by simple eddy viscosity and diffusivity models. It was shown that the URANS can capture the general trends of  $A$ ,  $C_f$  and  $St$ .

In summary, the success of the optimal control theory is mainly attributed to two facts: First, there exists a single local maximum of the analogy factor within the wide parameter range considered in the present study. This helps a gradient-based method to reach the global maximum. Secondly, the slow processes of the random field does not significantly contribute to dissimilarity, whereas both coherent and random contributions are mainly governed by the distributions of the phase-averaged velocity and thermal fields.



# Chapter 4

## Conclusions

The present thesis studied the fundamental difference in response of velocity and temperature fields to an active control input in the form of traveling wave-like wall blowing and suction, in fully developed laminar and turbulent channel flows. By considering the generation mechanism of dissimilarity between the velocity and temperature fields, we then proposed a passive method, using porous media, for generating such dissimilar effects. The conclusions drawn from each chapter are summarised below.

In chapter 2, the results from a series of direct numerical simulations (DNSs) of a fully developed laminar channel flow (LCF) subjected to traveling wave-like wall blowing and suction are presented. By systematically changing the phase speed  $U_p$ , the wavelength  $\lambda_x$ , and the amplitude  $\phi_{rms}$  of the traveling wave, their impacts on the skin-friction coefficient  $C_f$ , the Stanton number  $St$ , and the analogy factor  $A (= 2St/C_f)$  are investigated at three different Reynolds numbers of  $Re = 10, 100$ , and  $500$ . From the  $\lambda_x - U_p$  maps of  $C_f$ ,  $St$ , and  $A$  their maximum values are found to occur between  $0 < U_p < 1.5$ . This happens due to the critical layer effect due to which the velocity and thermal fluctuations are amplified at a certain distance from the wall where the local mean velocity matches with the phase speed of the applied traveling wave. We found that dissimilar heat transfer enhancement ( $A > 1$ ) can be achieved using both upstream ( $U_p < 0$ ) and down stream ( $U_p > 0$ ) traveling waves. However, from energetic point of view, *i.e.* after taking into account the energy required for the control input, it is advantageous to employ downstream traveling waves (DTWs) compared to the upstream traveling waves (UTWs). It is found that dissimilar heat transfer enhancement is most pronounced when the phase speed is around 75% of the bulk mean velocity and the wavelength is around three times the channel height.

The similarity between the Stokes second problem and the present flow configuration lead to the modeling of increase in momentum and heat transfer in terms of influence layer thickness ( $\delta_{C_f}$  and  $\delta_{St}$ ) and the magnitude ( $M_{C_f}$  and  $M_{St}$ ). It is found that the influential layer thicknesses for both momentum and heat transfer, *i.e.*  $\delta_{C_f}$  and  $\delta_{St}$ , are well correlated with the Stokes layer thickness for fast traveling waves, *i.e.*,  $U_p < -1.0$  or  $U_p > 1.5$ . For the optimal traveling wave at  $(\lambda_x, U_p) = (2\pi, 0.75)$ ,  $\delta_{C_f}$  and  $\delta_{St}$  are both larger than the Stokes layer thickness, but their ratio still remains close to unity, *i.e.*,  $\delta_{St}/\delta_{C_f} \sim 1$ . On the other hand, the ratio of their magnitudes,  $M_{St}/M_{C_f}$ , becomes as high as 5 indicating that the larger thermal response within the influential layer thickness causes the dissimilarity.

In order to further discuss the mechanisms of the dissimilarity, phase analysis of the coherent velocity and thermal fields are conducted. It is shown that even though the governing equations and the boundary conditions for the streamwise velocity component and the temperature are made similar, their responses to applied traveling wave-like wall blowing and suction are essentially different. Specifically, the pressure gradient induced by the wall input accelerates and decelerates only the streamwise velocity component, while the temperature is unaffected. The induced dissimilarity between velocity and thermal fields is then carried by the spanwise roll created near the wall to result in strong dissimilarity between the wall heat flux and the skin friction. The budget of the difference between the Reynolds shear stress and the convective scalar flux also supports the above observation. Namely, the correlation between the wall-normal velocity component and the streamwise pressure gradient induced by the wall input is the dominant mechanism causing the dissimilarity. The results of the phase and budget analyses indicate that the continuity constraint on the velocity field, and the resultant pressure fluctuation, is the source of the dissimilarity.

In chapter 3, we extended our analysis to turbulent channel flow (TCF). Through a series of DNSs performed at  $Re = 2293$ , we studied the dissimilar response of velocity and temperature fields subjected to traveling wave-like wall blowing and suction. As a result, the global optimum of the traveling wave properties for maximising  $A$  were identified as  $(\lambda_x, U_p) = (1.12, 0.30)$ . Another set of parametric survey at the higher Reynolds number of  $Re = 5055$  suggests that, unlike in the case of laminar flow, the globally optimal control input under turbulent regime is well scaled by the wall unit, and the resultant control performance is almost independent of the Reynolds number.

In addition to the coherent contribution the dissimilar heat transfer in TCF also consists of random contribution, due to the inherent chaotic nature of the turbulent flows. Based on the Fukagata-Iwamoto-Kasagi identity (FIK-identity) for  $C_f$  and  $St$ , the contributions of the coherent and random components to the dissimilarity were quantitatively evaluated. It was



found that, at the optimal point, the random contribution accounts for around 62% of the total contribution, whereas the coherent contribution remains relatively minor. The origin of coherent contribution follow almost similar route as that observed in LCF. Specifically, the applied wall blowing and suction produce the coherent pressure fluctuation, which modifies the velocity field, while the temperature field is unaffected due to the assumption of a passive scalar. It is found that the generated dissimilarity between the coherent streamwise velocity and the coherent temperature is dragged into the near-wall region due to wall suction, and results in the prominent peak of the coherent contribution to dissimilar heat transfer enhancement. The above results are also supported by the budget analysis of the coherent contribution, which highlights the importance of the pressure fluctuation through the correlation term of velocity/temperature and pressure gradient.

The analysis on random contribution, however, indicates the strong correlation between the random and the mean components. The contribution of the random field to dissimilar heat transfer enhancement is mostly caused by the dissimilarity in the wall-normal gradient of the phase-averaged velocity and thermal field, rather than the dissimilarity in the turbulent Prandtl number. This indicates that the local similarity between turbulent heat and momentum transfer holds fairly well even in the controlled flow. Thus the mechanism of coherent and random contribution in TCF are different. The budget analysis and flow visualization indicates that the interaction between the coherent and random fields is weak. It is also found that the modification of near-wall turbulent structures is mostly caused by the change in the mean wall shear due to the applied control input. This motivated us to propose a simple unsteady Reynolds-averaged Navier–Stokes (URANS) approach in which only the phase-averaged velocity and thermal fields are solved, whereas the effects of the random field are modeled by simple eddy viscosity and diffusivity models. It was shown that the URANS can capture the general trends for the performance indices  $C_f$ ,  $St$ , and  $A$ .

In chapter 4, we explored the possibility for using porous media as a passive mechanism for generating traveling wave-like wall blowing and suction. However, the absence of traveling wave from the leading edge of the plate lead to a value less than one for the analogy factor. Hence a source of disturbance is introduced upstream of the porous media. It is found that by fine tuning the porous and geometric parameters, dissimilar heat transfer enhancement can be achieved using porous media.

In summary, the thesis details the underlying difference between momentum and heat transfer in a channel flow subjected to a control input in the form of a traveling wave-like wall blowing and suction. The results indicate that even under the most stringent scenario, where the governing equations and the boundary conditions for the streamwise velocity and

temperature have a similar form, dissimilar heat transfer enhancement can be achieved. The proposed idea for generating traveling wave-like wall blowing and suction using porous media is original, and the porous materials serve as a potential future candidate in the designing of superior energy efficient thermo-fluid devices.

# References

- Achaichia, A. and Cowell, T. A. (1988). Heat transfer and pressure drop characteristics of flat tube and louvered plate fin surfaces. *Exp. Therm. Fluid Sci.*, 1:147–157.
- Antonia, R. A., Abe, H., and Kawamura, H. (2009). Analogy between velocity and scalar fields in a turbulent channel flow. *J. Fluid Mech.*, 628:241–268.
- Antonia, R. A., Krishnamoorthy, L. V., and Fulachier, L. (1988). Correlation between the longitudinal velocity fluctuation and temperature fluctuation in the near-wall region of a turbulent boundary layer. *Int. J. Heat Mass Transf.*, 31:723–730.
- Araya, G., Leonardi, S., and Castillo, L. (2008). Numerical assessment of local forcing on the heat transfer in a turbulent channel flow. *Phys. Fluids*, 20:085105.
- Bewley, T. R. (2009). A fundamental limit on the balance of power in a transpiration-controlled channel flow. *J. Fluid Mech.*, 632:443–446.
- Bewley, T. R., Moin, P., and Temam, R. (2001). DNS-based predictive control of turbulence: an optimal benchmark for feedback algorithms. *J. Fluid Mech.*, 447:179–225.
- Bons, J. P. (2002).  $St$  and  $C_f$  augmentation for real turbine roughness with elevated freestream turbulence. *J. Turbomach.*, 124:632–644.
- Boomsma, K., Poulikakos, D., and Zwick, F. (2003). Metal foams as compact high performance heat exchangers. *Mech. Mater.*, 35:1161–1176.
- Bremhorst, K. and Bullock, K. J. (1970). Spectral measurements of temperature and longitudinal velocity fluctuations in fully developed pipe flow. *Int. J. Heat Mass Tran.*, 13:1313–1329.
- Breugem, W., Boersma, B., and Uittenbogaard, R. (2006). The influence of wall permeability on turbulent channel flow. *J. Fluid Mech.*, 562:35–72.
- Chandesris, M., D’Hueppe, A., Mathieu, B., Jamet, D., and Goyeau, B. (2013). Direct numerical simulation of turbulent heat transfer in a fluid-porous domain. *Phys. Fluids*, 25:125110.
- Chilton, T. H. and Colburn, A. P. (1934). Mass-transfer coefficients, prediction from data on heat transfer and fluid friction. *Ind. Engng Chem.*, 26:1183–1187.
- Choi, H., Moin, P., and Kim, J. (1994). Active turbulence control for drag reduction in wall-bounded flows. *J. Fluid Mech.*, 262:75–110.

- Dahmen, W., Müller, S., Rom, M., Schweikert, S., Selzer, M., and Wolfersdorf, J. V. (2015). Numerical boundary layer investigations of transpiration-cooled turbulent channel flow. *Mech. Mater.*, 86:90–100.
- de Segura, G. G., Sharma, A., and García-Mayoral, R. (2018). Turbulent drag reduction using anisotropic permeable substrates. *Flow Turbul. Combust.*, 100:995–1014.
- Dean, R. D. (1978). Reynolds number dependence of skin friction and other bulk flow variables in two-dimensional rectangular duct flow. *ASME J. Fluids Eng.*, 100:215–222.
- Dong, J., Chen, J., Chen, Z., Zhang, W., and Zhou, Y. (2007). Heat transfer and pressure drop correlations for the multi-louvered fin compact heat exchangers. *Energ. Convers. Manage.*, 48:1506–1515.
- Elyyan, M. A., Rozati, A., and Tafti, D. K. (2008). Investigation of dimpled fins for heat transfer enhancement in compact heat exchangers. *Int. J. Heat Mass Transf.*, 51:11–12.
- Fiebig, M. (1995). Embedded vortices in internal flow: heat transfer and pressure loss enhancement. *Int. J. Heat Fluid Fl.*, 16:376–388.
- Fiedler, H. E. (1975). Transport of heat across a plane turbulent mixing layer. *Adv. Geophys.*, 18:93–109.
- Finnigan, J. (2000). Turbulence in plant canopies. *Annu. Rev. Fluid Mech.*, 32:519–571.
- Floryan, J. M. and Zandi, S. (2019). Reduction of pressure losses and increase of mixing in laminar flows through channels with long-wavelength vibrations. *J. Fluid Mech.*, 864:670–707.
- Forooghi, P., Weidenlener, A., Magagnato, F., Boehm, B., Kubach, H., Koch, T., and Frohnäpfel, B. (2018). DNS of momentum and heat transfer over rough surfaces based on realistic combustion chamber deposit geometries. *Int. J. Heat Fluid Fl.*, 69:83–94.
- Foures, D. P. G., Caulfield, C. P., and Schmid, P. J. (2014). Optimal mixing in two-dimensional plane Poiseuille flow at finite Péclet number. *J. Fluid Mech.*, 748:241–277.
- Fukagata, K., Iwamoto, K., and Kasagi, N. (2002). Contribution of Reynolds stress distribution to the skin friction in wall-bounded flow. *Phys. Fluids*, 14:L73–L76.
- Fukagata, K., Sugiyama, K., and Kasagi, N. (2009). On the lower bound of net driving power in controlled duct flows. *Physica D: Nonlinear Phenomena*, 238:1082–1086.
- García-Mayoral, R. and Jiménez, J. (2011). Drag reduction by riblets. *Phil. Trans. R. Soc. A*, 369:1412–1427.
- Han, J. C., Glicksman, L. R., and , W. M. R. (1978). An investigation of heat transfer and friction for rib-roughened surfaces. *Int. J. Heat Mass Transf.*, 21:1143–1156.
- Hasegawa, Y. and Kasagi, N. (2011). Dissimilar control of momentum and heat transfer in a fully developed turbulent channel flow. *J. Fluid Mech.*, 683:57–93.
- Hassanzadeh, P., Chini, G. P., and Doering, C. R. (2014). Wall to wall optimal transport. *J. Fluid Mech.*, 751:627–662.

- Hewitt, D. R. (2014). High Rayleigh number convection in a porous medium. PhD thesis, University of Cambridge.
- Hewitt, D. R., Neufeld, J. A., and Lister, J. R. (2012). Ultimate regime of high Rayleigh number convection in a porous medium. *Phys. Rev. Lett.*, 108:224503.
- Higashi, K., Mamori, H., and Fukagata, K. (2011). Simultaneous control of friction drag reduction and heat transfer augmentation by traveling wave-like blowing/suction. *Comput. Thermal Scien.*, 3:521–530.
- Hoepffner, J. and Fukagata, K. (2009). Pumping or drag reduction? *J. Fluid Mech.*, 635:171–187.
- Howell, J. R., Hall, M. J., and Ellzey, J. L. (1996). Combustion of hydrocarbon fuels within porous inert media. *Mech. Mater.*, 22:121–145.
- Hunt, J. C. R., Wray, A., and Moin, P. (1988). Eddies, stream, and convergence zones in turbulent flows. In *Center for Turbulence Research, Proceedings of the Summer Program*, pages 193–208. Stanford University.
- Hussain, A. K. M. F. and Reynolds, W. C. (1970). The mechanics of an organized wave in turbulent shear flow. *J. Fluid Mech.*, 41:241–258.
- Inaoka, K., Yamamoto, J., and Suzuki, K. (1999). Dissimilarity between heat transfer and momentum transfer in a disturbed turbulent boundary layer with insertion of a rod - modeling and numerical simulation. *Int. J. Heat Fluid Fl.*, 20:290–301.
- Ingham, D. B. and Pop, I. (1998). *Transport phenomena in porous media I*. Elsevier.
- Ingham, D. B. and Pop, I. (2002). *Transport phenomena in porous media II*. Elsevier.
- Ingham, D. B. and Pop, I. (2005). *Transport phenomena in porous media III*. Elsevier.
- Ismail, L. and Velraj, R. (2009). Studies on fanning friction (f) and Colburn (j) factors of offset and wavy fins compact plate fin heat exchanger-a CFD approach. *Num. Heat Transfer, Part A: Applications*, 56:987–1005.
- Jimenez, J., Uhlmann, M., Pinelli, A., and Kawahara, G. (2001). Turbulent shear flow over active and passive porous surfaces. *J. Fluid Mech.*, 442:89–117.
- Kametani, Y. and Fukagata, K. (2011). Direct numerical simulation of spatially developing turbulent boundary layers with uniform blowing or suction. *J. Fluid Mech.*, 681:154–172.
- Kasagi, N., Hasegawa, Y., Fukagata, K., and Iwamoto, K. (2012). Control of turbulent transport: Less friction and more heat transfer. *Trans. ASME: J. Heat Transfer*, 134:031009.
- Kestin, J. and Richardson, P. D. (1963). Heat transfer across turbulent, incompressible boundary layers. *Int. J. Heat Mass Tran.*, 6:147–189.
- Keys, W., Crawford, M. E., and Weigand, B. (2005). *Convective Heat and Mass Transfer*. McGraw-Hill.

- Khadra, K., Angot, P., Parneix, S., and Caltagirone, J. P. (2000). Fictitious domain approach for numerical modelling of Navier–Stokes equations. *Int. J. Numer. Methods Fluids*, 34:651–684.
- Kim, J. and Moin, P. (1985). Application of a fractional-step method to incompressible Navier–Stokes equations. *J. Comput. Phys*, 59:308–323.
- Koganezawa, S., Mitsuishi, A., Shimura, T., Iwamoto, K., Mamori, H., and Murata, A. (2019). Pathline analysis of traveling wavy blowing and suction control in turbulent pipe flow for drag reduction. *Int. J. Heat Fluid Fl.*, 77:388–401.
- Kong, H., H. Choi, and Lee, J. S. (2001). Dissimilarity between the velocity and temperature fields in a perturbed turbulent thermal boundary layer. *Phys. Fluids*, 13:1466–1479.
- Lee, C., Min, T., and Kim, J. (2008). Stability of a channel flow subject to wall blowing and suction in the form of a traveling wave. *Phys. Fluids*, 20:101513.
- Lieu, B. K., Moarref, R., and Jovanović, M. R. (2010). Controlling the onset of turbulence by streamwise travelling waves. Part 2. Direct numerical simulation. *J. Fluid Mech.*, 663:100–119.
- Mamori, H., Fukagata, K., and Hoepffner, J. (2010). Phase relationship in laminar channel flow controlled by traveling wave-like blowing or suction. *Phys. rev. E*, 81:046304.
- Mamori, H., Iwamoto, K., and Murata, A. (2014). Effect of the parameters of traveling waves created by blowing and suction on the relaminarization phenomena in fully developed turbulent channel flow. *Phys. Fluids*, 26:015101.
- Manglik, R. M. and Bergles, A. E. (1995). Heat transfer and pressure drop correlations for the rectangular offset strip fin compact heat exchanger. *Exp. therm. fluid*, 10:171–180.
- Maslowe, S. A. (1986). Critical layers in shear flows. *Annu. Rev. Fluid Mech.*, 18:405–432.
- Matsubara, K., Miura, T., and Ohta, H. (2015). Transport dissimilarity in turbulent channel flow disturbed by rib protrusion with aspect ratio up to 64. *Int. J. Heat Mass Transf.*, 86:113–123.
- Min, T., Kang, S. M., Speyer, J. L., and Kim, J. (2006). Sustained sub-laminar drag in a fully developed turbulent channel flow. *J. Fluid Mech.*, 558:309–318.
- Mittal, R. and Iaccarino, G. (2005). Immersed boundary methods. *Annu. Rev. Fluid Mech.*, 37:239–261.
- Moarref, R. and Jovanović, M. R. (2010). Controlling the onset of turbulence by streamwise travelling waves. Part 1. Receptivity analysis. *J. Fluid Mech.*, 663:70–99.
- Motoki, S., Kawahara, G., and Shimizu, M. (2018). Optimal heat transfer enhancement in plane Couette flow. *J. Fluid Mech.*, 835:1157–1198.
- Nepf, H. M. (2012). Flow and transport in regions with aquatic vegetation. *Annu. Rev. Fluid Mech.*, 44:123–142.

- Nield, D. A. and Bejan, A. (2006). *Convection in porous media*. Springer.
- Nishiyama, Y., Kuwata, Y., and Suga, K. (2020). Direct numerical simulation of turbulent heat transfer over fully resolved anisotropic porous structures. *Int. J. Heat Fluid Fl.*, 81:108515.
- Ogino, K., Mamori, H., Fukushima, N., Fukudome, K., and Yamamoto, M. (2019). Direct numerical simulation of Taylor-Couette turbulent flow controlled by a traveling wave-like blowing and suction. *Int. J. Heat Fluid Fl.*, 80:108463.
- Pasinato, H. D. (2011). Velocity and temperature dissimilarity in fully developed turbulent channel and plane Couette flows. *Int. J. Heat Fluid Fl.*, 32:11–25.
- Quadrio, M., Floryan, J. M., and Luchini, P. (2007). Effect of streamwise-periodic wall transpiration on turbulent friction drag. *J. Fluid Mech.*, 576:425–444.
- Quadrio, M., Ricco, P., and Viotti, C. (2009). Streamwise-travelling waves of spanwise wall velocity for turbulent drag reduction. *J. Fluid Mech.*, 627:161–178.
- Reynolds, O. (1874). On the extent and action of the heating surface for steam boilers. *Proc. Lit. Phil. Soc. Manchester*, 14:7–12.
- Rosti, M. E., Brandt, L., and Pinelli, A. (2018). Turbulent channel flow over an anisotropic porous wall-drag increase and reduction. *J. Fluid Mech.*, 842,:381–394.
- Stalio, E. and Nobile, E. (2003). Direct numerical simulation of heat transfer over riblets. *Int. J. Heat Fluid Fl.*, 24:356–371.
- Suga, K. and Kuwata, Y. (2017). Direct numerical simulation of turbulence over anisotropic porous media. *J. Fluid Mech.*, 831:41–71.
- Suga, K., Okazaki, Y., Ho, U., and Kuwata, Y. (2018). Anisotropic wall permeability effects on turbulent channel flows. *J. Fluid Mech.*, 855:983–1016.
- Suzuki, H., Suzuki, K., and Sato, T. (1988). Dissimilarity between heat and momentum transfer in a turbulent boundary layer disturbed by a cylinder. *Int. J. Heat Mass Transf.*, 31:259–265.
- Suzuki, T. and Hasegawa, Y. (2017). Estimation of turbulent channel flow at  $Re_\tau = 100$  based on the wall measurement using a simple sequential approach. *J. Fluid Mech.*, 830:760–796.
- Wang, Z., Mathai, V., and Sun, C. (2019). Self-sustained biphasic catalytic particle turbulence. *Nat. Commun.*, 10:1–7.
- Wood, B. D., He, X., and Apte, S. (2020). Modeling turbulent flows in porous media. *Annu. Rev. Fluid Mech.*, 52:171–203.
- Woodcock, J. D., Sader, J. E., and Marusic, I. (2012). Induced flow due to blowing and suction flow control: an analysis of transpiration. *J. Fluid Mech.*, 690:366–398.
- Yamamoto, A., Hasegawa, Y., and Kasagi, N. (2013). Optimal control of dissimilar heat and momentum transfer in a fully developed turbulent channel flow. *J. Fluid Mech.*, 733:189–220.

- Yu, B. and Kawaguchi, Y. (2005). DNS of fully developed turbulent heat transfer of a viscoelastic drag-reducing flow. *Int. J. Heat Mass Transf.*, 48:4569–4578.
- Zhao, M. X., Huang, W. X., and Xu, C. X. (2019). Drag reduction in turbulent flows along a cylinder by streamwise-travelling waves of circumferential wall velocity. *J. Fluid Mech.*, 862:75–98.
- Zhou, A., Klewicki, J., and Pirozzoli, S. (2019). Properties of the scalar variance transport equation in turbulent channel flow. *Phys. Rev. Fluids*, 4:024606.



# Appendix A

## Grid resolution effect

### A.1 Laminar channel flow

To check the effect of grid resolution, additional simulations are run for the highest Reynolds number considered in the laminar channel flow, *i.e.*  $Re = 500$ , and for the reference phase speed of  $U_p = 0.75$ . These additional simulation are run by doubling the number of spectral nodes  $(N_x, N_y)$  from  $(64, 65)$  to  $(128, 129)$ . Results plotted in figure A.1 reveals the adequacy of the current number of spectral nodes for conducting the simulations. For the reference point of  $(\lambda_x, U_p) = (2\pi, 0.75)$  maximum error in  $C_f$ ,  $St$ , and  $A$  are found to be 0.0%, 0.07%, and 0.07%, respectively.

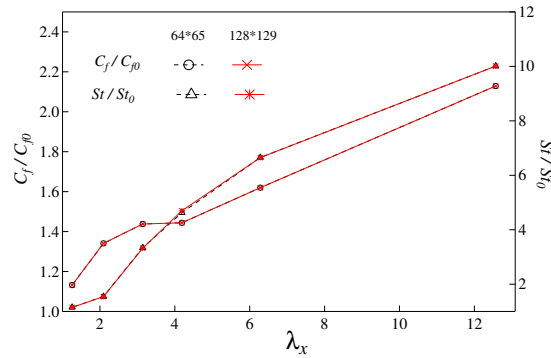


Figure A.1 Effect of grid resolution on the performance indices for the reference phase speed of  $U_p = 0.75$  at  $Re = 500$ .

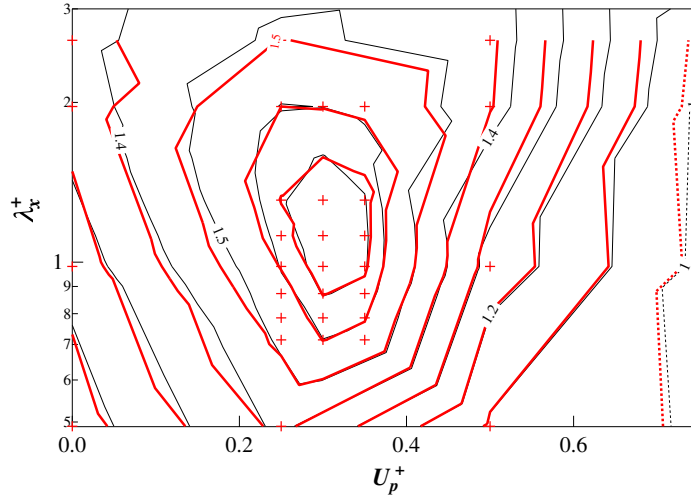


Figure A.2 Contour plot of  $A$  around the optimal point  $(\lambda_x, U_p) = (5\pi/14, 0.30)$ . The black contours represent Case O and thick red contours represent Case 1 (refer Table A.1). The  $+$  indicates the 35 cases for which the additional simulations are carried out.

	$(L_x, L_y, L_z)$	$(N_x, N_y, N_z)$	$(M_x, M_y, M_z)$	$(\Delta x^+, \Delta y_{min}^+ - \Delta y_{max}^+, \Delta z^+)$
Case O	$(5\pi, 2, 2\pi)$	$(128, 64, 128)$	$(192, 97, 192)$	$(12.27, 0.08 - 9.82, 4.90)$
Case 1	$(2.5\pi, 2, \pi)$	$(128, 96, 128)$	$(192, 145, 192)$	$(6.14, 0.04 - 6.54, 2.45)$
Case 2	$(5\pi, 2, \pi)$	$(256, 96, 128)$	$(384, 145, 192)$	$(6.14, 0.04 - 6.54, 2.45)$

Table A.1 Computational domain size, number of spectral modes, number of grid points in the physical space, and grid spacing used for the grid resolution check.

## A.2 Turbulent channel flow

Grid independence around the optimal location  $(\lambda_x, U_p) = (1.12, 0.30)$  is checked by performing 35 additional simulations (termed Case 1) with increased grid resolution (refer Table A.1) compared to the original parametric study (termed Case O). It is found that the location of the globally optimal point and surrounding contours remain almost unchanged as is evident from the contour plot of  $A$  shown in figure A.2. More specifically, the difference in the values of  $C_f$ ,  $St$ , and  $A$  at the global optimal point are found to be 0.87%, 0.85%, and 0.06%, respectively.

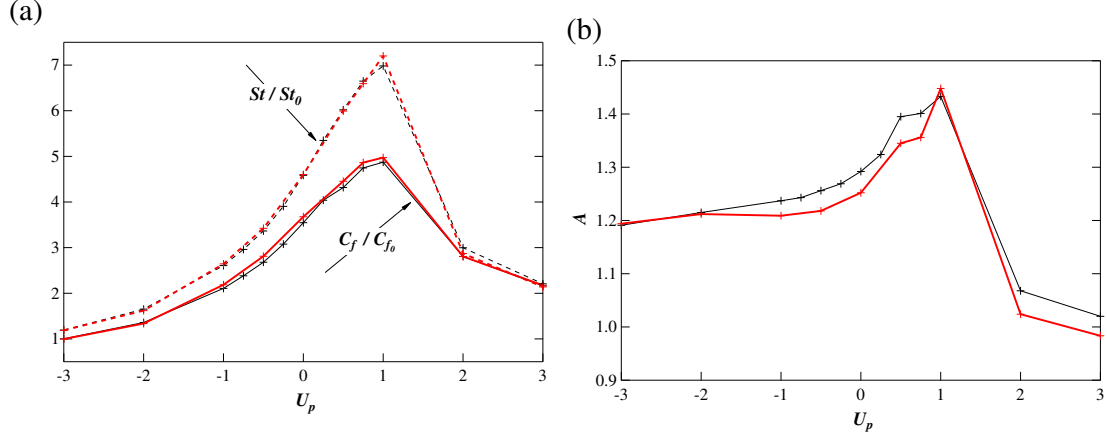


Figure A.3 Variation of (a)  $C_f/C_{f_0}$  and  $St/St_0$  and (b)  $A$  as a function of  $U_p$  for  $\lambda_x = 5\pi$ . The black lines represent Case - O and thick red lines represent Case - 2 (refer Table A.1). The + indicates the 10 cases for which the additional simulations are carried out.

For any given  $U_p$ , the value of  $C_f/C_{f_0}$  increases with increase in  $\lambda_x$ , and for  $(\lambda_x, U_p) = (5\pi, 0.50)$ , the friction Reynolds number for the controlled case almost gets doubled. Therefore, additional grid convergence study is carried out for  $\lambda_x = 5\pi$  with systematically changing  $U_p$  (Case 2 in Table A.1). The changes in the control performance indices due to the grid refinement were found to be at most 4.93%, 4.20%, and 4.12% for the values of  $C_f$ ,  $St$ , and  $A$ , respectively. These changes are generally sufficiently small in comparison to the changes due to the application of the control, and do not change the present conclusions.



## Appendix B

# Effects of phase-angle between the top and bottom wall control input

### B.1 Laminar channel flow

For the optimal point of  $(\lambda_x, U_p) = (2\pi, 0.75)$  at  $Re = 100$ , the phase-angle between the control input at the top and bottom wall is systematically changed from 0 to  $\pi$ , *i.e.* from sinuous to varicose mode, to check the effect of phase-angle on the performance indices. These simulations are performed after keeping the dimensions of the computational domain, the numbers of spectral modes, and the grid spacing in all the directions the same as that of the original parametric simulations. From the plots of  $C_f/C_{f0}$ ,  $St/St_0$ , and  $A$ , shown in figure B.1, it can be concluded that the varicose mode is the most effective mode for achieving dissimilar heat transfer enhancement in a laminar channel flow. The effectiveness of varicose mode with regard to drag reduction aspect have previously been reported by Mamori et al. (2010) and Woodcock et al. (2012).

### B.2 Turbulent channel flow

For the turbulent channel flow at  $Re_\tau = 150$ , the phase-angle between the control input at the top and bottom wall is systematically changed from 0 to  $\pi$ , *i.e.* from sinuous to varicose mode, for the global optimal point  $(\lambda_x, U_p) = (5\pi/14, 0.30)$ . It is known that, when wall blowing and suction is applied, the immediate response of the flow can be given by the inviscid potential flow, where the pressure fluctuation penetrates into the fluid region

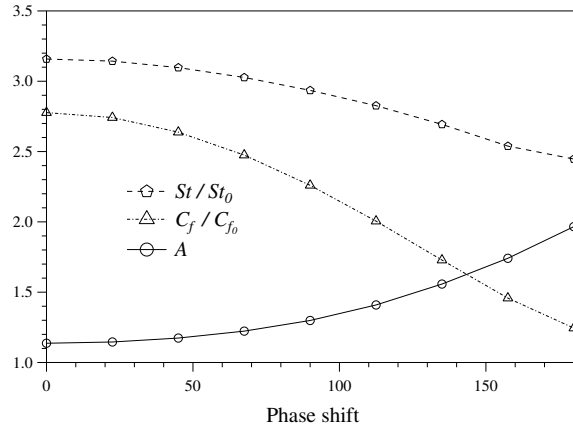


Figure B.1 Effect of phase-angle on the performance indices for the optimal point of  $(\lambda_x, U_p) = (2\pi, 0.75)$  at  $Re = 100$ . The phase-angles equal to zero and 180 degree correspond to sinuous and varicose modes, respectively.

within a length-scale similar to the wavelength of wall blowing/suction. For the global optimal point,  $\lambda_x \approx 1.1$ , so that the effects of wall blowing and suction only reach at the channel center. For this reason, we also conduct another parametric survey for a longer wavelength at  $(\lambda_x, U_p) = (5\pi/4, 0.30)$ . In the latter case,  $\lambda_x \approx 4.0$ , so that it is sufficient to have interaction between the top and bottom walls. The dimensions of the computational domain, the numbers of spectral modes, and the grid spacing in all the directions are the same as that of the original parametric simulations. The results are plotted in figure B.2. From the plots of  $C_f/C_{f_0}$ ,  $St/St_0$ , and  $A$ , it can be concluded that the phase-angle hardly affects the control performances, unlike the case of laminar channel flow.

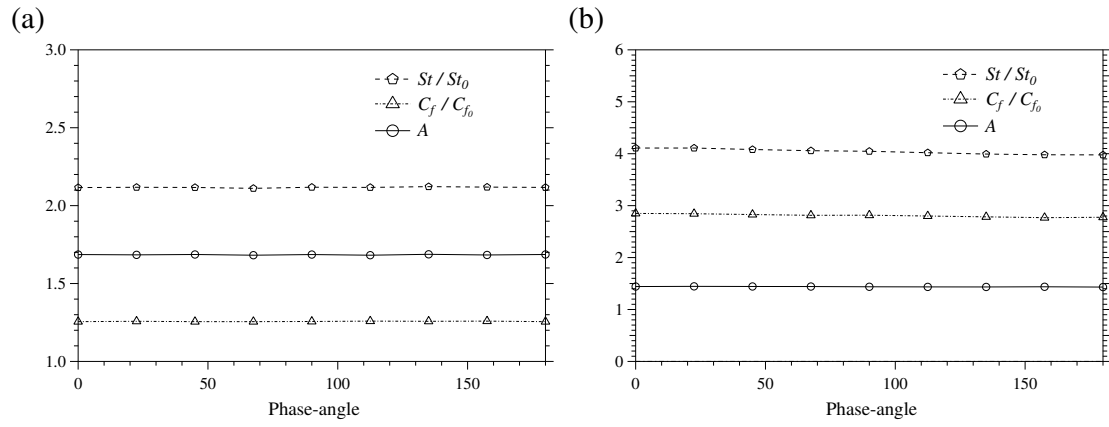


Figure B.2  $C_f/C_{f_0}$ ,  $St/St_0$ , and  $A$  as a function of phase-angle between the top and bottom wall for (a) the globally optimal point  $(\lambda_x, U_p) = (5\pi/14, 0.30)$  and (b)  $(\lambda_x, U_p) = (5\pi/4, 0.30)$ .





# Appendix C

## Budget equations

### C.1 Governing equations for the coherent and random components

#### C.1.1 Derivation of the governing equations for the coherent components

The governing equation for the mean temperature field is obtained from equation (2.3) by taking average along the homogeneous directions  $x$  and  $z$ , and also along time  $t$ :

$$\frac{\partial \bar{\theta}}{\partial t} + \frac{\partial \overline{(u_j \theta)}}{\partial x_j} = \bar{Q} + \frac{1}{Pe} \frac{\partial^2 \bar{\theta}}{\partial x_j \partial x_j}. \quad (\text{C.1})$$

On applying phase-averaging to equation (2.3), the governing equation for the phase-averaged temperature field follows as

$$\frac{\partial \langle \theta \rangle}{\partial t} + \frac{\partial \langle (u_j \theta) \rangle}{\partial x_j} = \langle Q \rangle + \frac{1}{Pe} \frac{\partial^2 \langle \theta \rangle}{\partial x_j \partial x_j}. \quad (\text{C.2})$$

Subtracting equation (C.1) from equation (C.2) the governing equation for the coherent temperature field is obtained:

$$\frac{\partial \tilde{\theta}}{\partial t} + \frac{\partial \widetilde{(u_j \theta)}}{\partial x_j} = \tilde{Q} + \frac{1}{Pe} \frac{\partial^2 \tilde{\theta}}{\partial x_j \partial x_j}. \quad (\text{C.3})$$

Using the relation  $\widetilde{fg} = \langle fg \rangle - \overline{fg} = \bar{f}\tilde{g} + \tilde{f}\bar{g} + \widetilde{\tilde{f}\tilde{g}} + \widetilde{f''g''}$  (for any arbitrary quantity  $f$  and  $g$ ) equation (C.3) can be rearranged as

$$\frac{\partial \tilde{\theta}}{\partial t} + \bar{u}_j \frac{\partial \tilde{\theta}}{\partial x_j} = -\tilde{u}_j \frac{\partial \tilde{\theta}}{\partial x_j} - \frac{\partial \left( \tilde{u}_j \tilde{\theta} + \bar{u}_j'' \tilde{\theta}'' \right)}{\partial x_j} + \tilde{Q} + \frac{1}{Pe} \frac{\partial^2 \tilde{\theta}}{\partial x_j \partial x_j}. \quad (\text{C.4})$$

Similarly, the governing equations for the streamwise and wall-normal coherent velocity components, *i.e.*  $\tilde{u}$  and  $\tilde{v}$ , can be derived as follows:

$$\frac{\partial \tilde{u}}{\partial t} + \bar{u}_j \frac{\partial \tilde{u}}{\partial x_j} = -\tilde{u}_j \frac{\partial \tilde{u}}{\partial x_j} - \frac{\partial \left( \tilde{u}_j \tilde{u} + \bar{u}_j'' \tilde{u}'' \right)}{\partial x_j} - \frac{\partial \tilde{p}}{\partial x} + \frac{1}{Re} \frac{\partial^2 \tilde{u}}{\partial x_j \partial x_j}, \quad (\text{C.5})$$

$$\frac{\partial \tilde{v}}{\partial t} + \bar{u}_j \frac{\partial \tilde{v}}{\partial x_j} = -\tilde{u}_j \frac{\partial \tilde{v}}{\partial x_j} - \frac{\partial \left( \tilde{u}_j \tilde{v} + \bar{u}_j'' \tilde{v}'' \right)}{\partial x_j} - \frac{\partial \tilde{p}}{\partial y} + \frac{1}{Re} \frac{\partial^2 \tilde{v}}{\partial x_j \partial x_j}. \quad (\text{C.6})$$

### C.1.2 Derivation of the governing equations for the random components

The governing equation for the random temperature field is obtained by subtracting equation (C.2) from equation (2.3):

$$\frac{\partial \theta''}{\partial t} + \langle u_j \rangle \frac{\partial \theta''}{\partial x_j} = -u_j'' \frac{\partial \langle \theta \rangle}{\partial x_j} - \frac{\partial \left( u_j'' \theta'' - \langle u_j'' \theta'' \rangle \right)}{\partial x_j} + Q'' + \frac{1}{Pe} \frac{\partial^2 \theta''}{\partial x_j \partial x_j}, \quad (\text{C.7})$$

where the relation  $(fg)'' = fg - \langle fg \rangle = \langle f \rangle g'' + f'' \langle g \rangle + f'' g'' - \langle f'' g'' \rangle$  has been used while deriving the above equation.

On a similar note, the governing equations for the streamwise and wall-normal random velocity components, *i.e.*  $u''$  and  $v''$ , can be expressed as

$$\frac{\partial u''}{\partial t} + \langle u_j \rangle \frac{\partial u''}{\partial x_j} = -u_j'' \frac{\partial \langle u'' \rangle}{\partial x_j} - \frac{\partial \left( u_j'' u'' - \langle u_j'' u'' \rangle \right)}{\partial x_j} - \frac{\partial p''}{\partial x} + \frac{1}{Re} \frac{\partial^2 u''}{\partial x_j \partial x_j}, \quad (\text{C.8})$$

$$\frac{\partial v''}{\partial t} + \langle u_j \rangle \frac{\partial v''}{\partial x_j} = -u_j'' \frac{\partial \langle v'' \rangle}{\partial x_j} - \frac{\partial \left( u_j'' v'' - \langle u_j'' v'' \rangle \right)}{\partial x_j} - \frac{\partial p''}{\partial y} + \frac{1}{Re} \frac{\partial^2 v''}{\partial x_j \partial x_j}. \quad (\text{C.9})$$

## C.2 Budget equation for $\overline{\tilde{v}(\tilde{\theta} - \tilde{u})}$

Subtracting equation (C.5) from equation (C.4), the governing equation for  $(\tilde{\theta} - \tilde{u})$  is obtained as

$$\begin{aligned} \frac{\partial(\tilde{\theta} - \tilde{u})}{\partial t} + \bar{u}_j \frac{\partial(\tilde{\theta} - \tilde{u})}{\partial x_j} = & -\tilde{u}_j \frac{\partial(\tilde{\theta} - \tilde{u})}{\partial x_j} - \frac{\partial \left( \widetilde{\tilde{u}_j \tilde{\theta}} + \widetilde{u_j'' \theta''} - \widetilde{\tilde{u}_j \tilde{u}} - \widetilde{u_j'' u''} \right)}{\partial x_j} \\ & + \tilde{Q} + \frac{\partial \tilde{p}}{\partial x} + \frac{1}{Pe} \frac{\partial^2 \tilde{\theta}}{\partial x_j \partial x_j} - \frac{1}{Re} \frac{\partial^2 \tilde{u}}{\partial x_j \partial x_j}. \end{aligned} \quad (\text{C.10})$$

Now, by following the three steps: first, multiply equation (C.6) with  $(\tilde{\theta} - \tilde{u})$ ; second, multiply equation (C.10) with  $\tilde{v}$ ; third, add the resultant two equations; the governing equation for  $\tilde{v}(\tilde{\theta} - \tilde{u})$  is obtained as

$$\begin{aligned} & \frac{\partial \{ \tilde{v}(\tilde{\theta} - \tilde{u}) \}}{\partial t} + \bar{u}_j \frac{\partial \{ \tilde{v}(\tilde{\theta} - \tilde{u}) \}}{\partial x_j} \\ = & -\tilde{v} \tilde{u}_j \frac{\partial(\tilde{\theta} - \tilde{u})}{\partial x_j} - (\tilde{\theta} - \tilde{u}) \tilde{u}_j \frac{\partial \tilde{v}}{\partial x_j} \\ & - (\tilde{\theta} - \tilde{u}) \frac{\partial \widetilde{u_j'' v''}}{\partial x_j} - \tilde{v} \frac{\partial \{ \widetilde{u_j'' (\theta'' - u'')} \}}{\partial x_j} \\ & + (\tilde{\theta} - \tilde{u}) \frac{\partial \widetilde{\tilde{u}_j \tilde{v}}}{\partial x_j} + \tilde{v} \frac{\partial \{ \widetilde{\tilde{u}_j (\tilde{\theta} - \tilde{u})} \}}{\partial x_j} \\ & - \frac{\partial}{\partial x_j} \left[ \tilde{u}_j \tilde{v} (\tilde{\theta} - \tilde{u}) - \frac{1}{Re} \left\{ \tilde{v} \frac{\partial}{\partial x_j} \left( \frac{\tilde{\theta}}{Pr} - \tilde{u} \right) + (\tilde{\theta} - \tilde{u}) \frac{\partial \tilde{v}}{\partial x_j} \right\} \right] \\ & - (\tilde{\theta} - \tilde{u}) \frac{\partial \tilde{p}}{\partial y} + \tilde{v} \left( \tilde{Q} + \frac{\partial \tilde{p}}{\partial x} \right) \\ & - \frac{1}{Re} \frac{\partial \tilde{v}}{\partial x_j} \frac{\partial}{\partial x_j} \left\{ \left( \frac{\tilde{\theta}}{Pr} - \tilde{u} \right) + (\tilde{\theta} - \tilde{u}) \right\}. \end{aligned} \quad (\text{C.11})$$

Applying averaging operation  $\overline{\{\}}$  to the above equation results in the budget equation for dissimilar heat and momentum flux for the coherent component  $\tilde{v}(\tilde{\theta} - \tilde{u})$ :

$$\begin{aligned}
& \frac{\partial \overline{\{\tilde{v}(\tilde{\theta} - \tilde{u})\}}}{\partial t} + \tilde{u}_j \frac{\partial \overline{\{\tilde{v}(\tilde{\theta} - \tilde{u})\}}}{\partial x_j} \\
= & -\tilde{v}\tilde{u}_j \frac{\partial (\tilde{\theta} - \tilde{u})}{\partial x_j} - \overline{(\tilde{\theta} - \tilde{u})\tilde{u}_j} \frac{\partial \tilde{v}}{\partial x_j} + \overline{u_j'' \tilde{v}''} \frac{\partial (\tilde{\theta} - \tilde{u})}{\partial x_j} + \overline{\{u_j''(\theta'' - u'')\}} \frac{\partial \tilde{v}}{\partial x_j} \\
& - \frac{\partial}{\partial x_j} \left[ (\tilde{\theta} - \tilde{u}) \overline{u_j'' \tilde{v}''} + \tilde{v} \overline{\{u_j''(\theta'' - u'')\}} + \tilde{u}_j \tilde{v}(\tilde{\theta} - \tilde{u}) - \frac{1}{Re} \left\{ \tilde{v} \frac{\partial}{\partial x_j} \left( \frac{\tilde{\theta}}{Pr} - \tilde{u} \right) + (\tilde{\theta} - \tilde{u}) \frac{\partial \tilde{v}}{\partial x_j} \right\} \right] \\
& + \left\{ -(\tilde{\theta} - \tilde{u}) \frac{\partial \tilde{p}}{\partial y} + \tilde{v} \left( \tilde{Q} + \frac{\partial \tilde{p}}{\partial x} \right) \right\} \\
& - \frac{1}{Re} \left[ \frac{\partial \tilde{v}}{\partial x_j} \frac{\partial}{\partial x_j} \left\{ \left( \frac{\tilde{\theta}}{Pr} - \tilde{u} \right) + (\tilde{\theta} - \tilde{u}) \right\} \right]. \tag{C.12}
\end{aligned}$$

The above equation is the general expression for the budget of  $\overline{\tilde{v}(\tilde{\theta} - \tilde{u})}$ .

### C.3 Budget equation for $\overline{v''(\theta'' - u'')}$

Subtracting equation (C.8) from equation (C.7), the governing equation for  $(\theta'' - u'')$  is obtained as

$$\begin{aligned}
\frac{\partial (\theta'' - u'')}{\partial t} + \langle u_j \rangle \frac{\partial (\theta'' - u'')}{\partial x_j} = & -u_j'' \frac{\partial \langle \theta \rangle - \langle u \rangle}{\partial x_j} - \frac{\partial (u_j'' \theta'' - \langle u_j'' \theta'' \rangle - u_j'' u'' + \langle u_j'' u'' \rangle)}{\partial x_j} \\
& + Q'' + \frac{\partial p''}{\partial x} + \frac{1}{Pe} \frac{\partial^2 \theta''}{\partial x_j \partial x_j} - \frac{1}{Re} \frac{\partial^2 u''}{\partial x_j \partial x_j}. \tag{C.13}
\end{aligned}$$

Now, by following the three steps: first, multiply equation (C.9) with  $(\theta'' - u'')$ ; second, multiply equation (C.13) with  $v''$ ; third, add the resultant two equations; the governing

equation for  $v''(\theta'' - u'')$  is obtained as

$$\begin{aligned}
& \frac{\partial \{v''(\theta'' - u'')\}}{\partial t} + \langle u_j \rangle \frac{\partial \{v''(\theta'' - u'')\}}{\partial x_j} \\
= & -u_j'' v'' \frac{\partial (\langle \theta \rangle - \langle u \rangle)}{\partial x_j} - u_j'' (\theta'' - u'') \frac{\partial \langle v \rangle}{\partial x_j} \\
& + (\theta'' - u'') \frac{\partial \langle u_j'' v'' \rangle}{\partial x_j} + v'' \frac{\partial \langle u_j'' (\theta'' - u'') \rangle}{\partial x_j} \\
& - \frac{\partial}{\partial x_j} \left[ u_j'' v'' (\theta'' - u'') + \frac{1}{Re} \frac{\partial}{\partial x_j} \left\{ v'' \frac{\partial}{\partial x_j} \left( \frac{\theta''}{Pr} - u'' \right) + (\theta'' - u'') \frac{\partial v''}{\partial x_j} \right\} \right] \\
& - (\theta'' - u'') \frac{\partial p''}{\partial y} + v'' \left( Q'' + \frac{\partial p''}{\partial x} \right) \\
& - \frac{1}{Re} \frac{\partial v''}{\partial x_j} \frac{\partial}{\partial x_j} \left\{ \left( \frac{\theta''}{Pr} - u'' \right) + (\theta'' - u'') \right\}. \tag{C.14}
\end{aligned}$$

Applying averaging operation  $\{\}$  to the above equation results in the budget equation for dissimilar heat and momentum flux for the random component  $\overline{v''(\theta'' - u'')}$ :

$$\begin{aligned}
& \frac{\partial \overline{v''(\theta'' - u'')}}{\partial t} + \overline{u_j} \frac{\partial \overline{v''(\theta'' - u'')}}{\partial x_j} \\
= & -\overline{u_j'' v''} \frac{\partial (\bar{\theta} - \bar{u})}{\partial x_j} - \overline{u_j'' v''} \frac{\partial (\bar{\theta} - \bar{u})}{\partial x_j} - \overline{u_j'' (\theta'' - u'')} \frac{\partial \bar{v}}{\partial x_j} - \overline{u_j'' (\theta'' - u'')} \frac{\partial \bar{v}}{\partial x_j} \\
& - \frac{\partial}{\partial x_j} \left[ \overline{\tilde{u}_j \{v''(\theta'' - u'')\}} + \overline{u_j'' v'' (\theta'' - u'')} + \frac{1}{Re} \frac{\partial}{\partial x_j} \left\{ v'' \frac{\partial}{\partial x_j} \left( \frac{\theta''}{Pr} - u'' \right) + (\theta'' - u'') \frac{\partial v''}{\partial x_j} \right\} \right] \\
& + \left\{ -(\theta'' - u'') \frac{\partial p''}{\partial y} + v'' \left( Q'' + \frac{\partial p''}{\partial x} \right) \right\} \\
& - \frac{1}{Re} \left[ \frac{\partial v''}{\partial x_j} \frac{\partial}{\partial x_j} \left\{ \left( \frac{\theta''}{Pr} - u'' \right) + (\theta'' - u'') \right\} \right]. \tag{C.15}
\end{aligned}$$

The above equation is the general expression for the budget of  $\overline{v''(\theta'' - u'')}$ .

## C.4 Budget equations for turbulent channel flow

For a fully developed turbulent channel flow, an averaged quantity  $\bar{f}$  is only a function of  $y$ . In addition, in the present study  $\tilde{Q} = Q'' = 0$  and  $Pr = 1$ . Therefore, the budget equations for  $\overline{\tilde{v}(\tilde{\theta} - \tilde{u})}$  and  $\overline{v''(\theta'' - u'')}$  gets simplified as

$$\begin{aligned}
 0 = & \underbrace{-\tilde{v}\tilde{v}\frac{\partial(\tilde{\theta} - \tilde{u})}{\partial y} + \overbrace{u_j''\widetilde{v''}}^{\text{coupling terms between coherent and random}}\frac{\partial(\tilde{\theta} - \tilde{u})}{\partial x_j} + \overbrace{\{u_j''(\theta'' - u'')\}}^{\text{coupling terms between coherent and random}}\frac{\partial\tilde{v}}{\partial x_j}}_{\text{production}} \\
 & \underbrace{-\frac{\partial}{\partial y}\left[(\tilde{\theta} - \tilde{u})\widetilde{v''v''} + \tilde{v}\{\widetilde{v''(\theta'' - u'')}}\right] + \tilde{v}\tilde{v}(\tilde{\theta} - \tilde{u}) - \frac{1}{Re}\frac{\partial\tilde{v}(\tilde{\theta} - \tilde{u})}{\partial y}}_{\text{diffusive flux}} \\
 & + \underbrace{\left\{- (\tilde{\theta} - \tilde{u})\frac{\partial\tilde{p}}{\partial y} + \tilde{v}\frac{\partial\tilde{p}}{\partial x}\right\}}_{\text{velocity/temperature fluctuation and pressure-gradient correlation}} \\
 & \underbrace{-\frac{2}{Re}\frac{\partial\tilde{v}}{\partial x_j}\frac{\partial(\tilde{\theta} - \tilde{u})}{\partial x_j}}_{\text{molecular dissipation}}. \tag{C.16}
 \end{aligned}$$

$$\begin{aligned}
0 = & \underbrace{-\overline{v''v''} \frac{\partial (\bar{\theta} - \bar{u})}{\partial y} - \overbrace{\widetilde{u_j''v''} \frac{\partial (\tilde{\theta} - \tilde{u})}{\partial x_j}}^{\text{coupling terms between coherent and random}} - \overline{u_j'' (\theta'' - u'')} \frac{\partial \tilde{v}}{\partial x_j}}_{\text{production}} \\
& - \underbrace{\frac{\partial}{\partial y} \left[ \tilde{v} \{ \widetilde{v'' (\theta'' - u'')} \} + v'' v'' (\theta'' - u'') - \frac{1}{Re} \frac{\partial}{\partial y} \{ v'' (\theta'' - u'') \} \right]}_{\text{diffusive flux}} \\
& + \underbrace{\left\{ -(\theta'' - u'') \frac{\partial p''}{\partial y} + v'' \frac{\partial p''}{\partial x} \right\}}_{\text{velocity/temperature fluctuation and pressure-gradient correlation}} \\
& - \underbrace{\frac{2}{Re} \frac{\partial v''}{\partial x_j} \frac{\partial (\theta'' - u'')}{\partial x_j}}_{\text{molecular dissipation}}. \tag{C.17}
\end{aligned}$$

In equations (C.16) and (C.17) the first three terms on the RHS (in the first line) are the production terms. The second and the third terms on RHS in equations (C.16) and (C.17) are equal but with opposite signs, indicating the coupling between coherent and random contributions to dissimilar control. The second line corresponds to turbulent and molecular diffusion. The fifth term (third line) represents the velocity/temperature fluctuation and pressure gradient correlation. The final term denotes molecular dissipation.

Now, the budget equation for  $\overline{v'(\theta' - u')}$  can be obtained by adding equations (C.16) and (C.17):

$$\begin{aligned}
 0 = & \underbrace{-\overline{v'v'} \frac{\partial(\bar{\theta} - \bar{u})}{\partial y}}_{\text{production}} \\
 & \underbrace{-\frac{\partial}{\partial y} \left[ \overline{v'v'(\theta' - u')} - \frac{1}{Re} \frac{\partial v'(\theta' - u')}{\partial y} \right]}_{\text{diffusive flux}} \\
 & + \underbrace{\left\{ -(\theta' - u') \frac{\partial p'}{\partial y} + v' \frac{\partial p'}{\partial x} \right\}}_{\text{velocity/temperature fluctuation and pressure-gradient correlation}} \\
 & \underbrace{-\frac{2}{Re} \frac{\partial v'}{\partial x_j} \frac{\partial(\theta' - u')}{\partial x_j}}_{\text{molecular dissipation}}. \tag{C.18}
 \end{aligned}$$

### Remarks

1. It is worth noting that equations (C.16) and (C.18) are the same for a laminar channel flow, since in the absence of random components  $\bar{v}(\bar{\theta} - \bar{u}) = \overline{v'(\theta' - u')}$ .
2. Similar to the case of uncontrolled flow, even under the wall blowing and suction, the integral of the turbulent diffusion within the entire domain is exactly zero, *i.e.*  $\int_{-1}^1 -\frac{\partial}{\partial y} \left[ \overline{v'v'(\theta' - u')} \right] dy = 0$ . On the other hand the integral of the viscous diffusion is non-zero:

$$\int_{-1}^1 \frac{\partial}{\partial y} \left[ \frac{1}{Re} \frac{\partial v'(\theta' - u')}{\partial y} \right] dy \equiv \frac{1}{Re} \left[ \frac{\partial v'(\theta' - u')}{\partial y} \right]_{y=-1}^{y=1} \neq 0, \tag{C.19}$$

since the viscous flux from the wall is non-zero under the present control input. This becomes evident from the Taylor series expansion of  $u'$ ,  $v'$ , and  $\theta'$  as shown below

$$\begin{aligned}
 u' &= 0 + b_1 y^+ + c_1 y^{+2} + d_1 y^{+3} + \dots \\
 v' &= v_w + 0 + c_2 y^{+2} + d_2 y^{+3} + \dots \\
 \theta' &= 0 + b_3 y^+ + c_3 y^{+2} + d_3 y^{+3} + \dots, \tag{C.20}
 \end{aligned}$$



---

where  $y^+$  is the distance from the wall.



# Appendix D

## Optimal control analysis of laminar developing channel flow

### D.1 Governing Equations

Schematic of the laminar developing channel flow considered for the analysis is shown in figure D.1. The streamwise and wall-normal directions are represented using  $x$  and  $y$  respectively. The velocity and thermal fields are assumed to be two-dimensional. The inlet velocity is specified as  $u_i^{in}(y)$ , which is a function of  $y$ . Similarly, the inlet temperature profile is given by  $\theta^{in}(y)$ . The profiles of streamwise velocity and temperature are set equal at the inlet and is given by  $u^{in} = \theta^{in} = (1 - e^{-y_{wall}/0.05})$ , where  $y_{wall}$  represents the distance from the wall. Specifically, both  $u^{in}$  and  $\theta^{in}$  take a value equal to one, except very close to the wall region where they are gradually reduced to zero, as shown in figure D.1. The profile of the wall-normal velocity is assumed to be zero at the inlet, *i.e.*  $v^{in} = 0$ .

The governing equations for the velocity field are the Navier-Stokes and continuity equations:

$$\frac{\partial u_i}{\partial t} + \frac{\partial (u_j u_i)}{\partial x_j} = -\frac{\partial p}{\partial x_i} + \frac{1}{Re} \frac{\partial^2 u_i}{\partial x_j \partial x_j}, \quad (\text{D.1})$$

$$\frac{\partial u_i}{\partial x_i} = 0, \quad (\text{D.2})$$

where all variables are normalized by uniform inlet velocity  $U_\infty^*$  and the channel half depth  $\delta^*$ . Here, a quantity with an asterisk represents a dimensional quantity, unless otherwise stated.

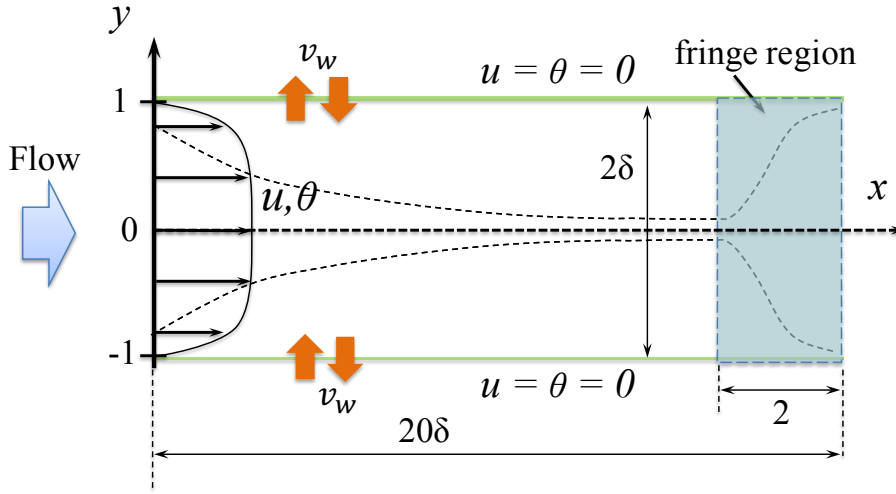


Figure D.1 Dimensions of the computational domain and coordinate system.

The Reynolds number is defined as  $Re = U_{\infty}^* \delta^* / \nu^*$ , where  $\nu^*$  is the kinematic viscosity of the fluid.

Since temperature in the present study is treated as a passive scalar, the transport equation for energy can be given by

$$\frac{\partial \theta}{\partial t} + \frac{\partial (u_j \theta)}{\partial x_j} = \frac{1}{RePr} \frac{\partial^2 \theta}{\partial x_j \partial x_j}, \quad (D.3)$$

where the Prandtl number  $Pr$  is the ratio of the kinematic viscosity  $\nu^*$  to the thermal diffusivity  $\alpha^*$ , namely,  $Pr = \nu^* / \alpha^*$ .

### D.1.1 Numerical Methodology

The velocity and thermal fields are solved using the same pseudo spectral code mentioned in chapter 2 and 3, where the number of Fourier modes in the  $x$  and  $y$  directions are  $(N_x, N_y) = (64, 33)$ . However, to realize a spatially-developing flow with a periodic boundary condition, we introduced a fringe region at the end of the computational domain. Inside the fringe region, artificial body force and heat source are imposed so that the velocity and thermal fields are forced to the prescribed inlet profiles, *i.e.*  $u_i^{in}$  and  $\theta^{in}$ . Adding the artificial terms,

equations (D.1) to (D.3) are modified as

$$\frac{\partial u_i}{\partial t} + \frac{\partial (u_j u_i)}{\partial x_j} = -\frac{\partial p}{\partial x_i} + \frac{1}{Re} \frac{\partial^2 u_i}{\partial x_j \partial x_j} + \eta_u (u_i^{in} - u_i), \quad (\text{D.4})$$

$$\frac{\partial u_i}{\partial x_i} = 0, \quad (\text{D.5})$$

$$\frac{\partial \theta}{\partial t} + \frac{\partial (u_j \theta)}{\partial x_j} = \frac{1}{Pe} \frac{\partial^2 \theta}{\partial x_j \partial x_j} + \eta_\theta (\theta^{in} - \theta). \quad (\text{D.6})$$

Here  $\eta_u$  is the coefficient specifying the magnitude of the artificial forcing on the velocity field, and  $\eta_\theta$  is the coefficient specifying the magnitude of the heat source term acting on the temperature field. The coefficients  $\eta_u$  and  $\eta_\theta$  have to be large enough to make the calculated velocity and temperature profiles to match with the prescribed inlet ones, while small enough to avoid numerical instability. They are typically set to be in the order of  $\Delta t^{-1}$ , where  $\Delta t$  is the numerical time step. In the present study  $\Delta t$  is set equal to 0.005.

The velocity boundary conditions at the wall are given by

$$u_i = \delta_{i,2} \phi, \quad (\text{D.7})$$

where  $\delta_{i,j}$  is Kronecker's delta function and is unity when  $i = j$ , zero otherwise. The control input  $\phi$  is in general a function of space and time. Similarly, the wall boundary condition for the temperature is given as

$$\theta = 0. \quad (\text{D.8})$$

In summary, our aim is to optimize the spatio-temporal distribution of  $\phi$  in order to enhance heat transfer with minimum pressure drop penalty throughout the entire channel. In this study,  $Re = 100$  and  $Pr$  is set equal to unity. Setting  $Pr = 1$  makes the transport equations for streamwise momentum and temperature take a similar form. Under the present thermal conditions (*i.e.*  $Pr = 1$  and  $u = \theta = 0$  at the wall), any dissimilarity between the streamwise velocity component and the scalar field should result from the continuity constraint on the velocity field.

### D.1.2 Performance indices

For an uncontrolled flow wall shear stress and heat transfer rate are quantified using skin friction coefficient ( $C_{fx}^0$ ) and Stanton number ( $St_x^0$ ) respectively. They are defined as

$$C_{fx}^0 = \frac{\tau_w^*(x)}{\frac{1}{2}\rho^*U_b^{*2}} = \frac{2}{Re} \frac{\partial u}{\partial y}, \quad (D.9)$$

$$St_x^0 = \frac{q_w^*(x)}{\rho^*C_p^*U_b^*\Theta_b^*} = \frac{1}{Pe} \frac{\partial \theta}{\partial y}, \quad (D.10)$$

where  $\tau_w^*(x)$ ,  $q_w^*(x)$ ,  $\rho^*$ , and  $C_p^*$  are the wall shear stress, heat flux at the wall, density of fluid, and the heat capacity of the fluid, respectively.

To quantify the performance of the control input, the following three non-dimensional parameters, *i.e.*, drag reduction rate ( $DR$ ), heat transfer augmentation rate ( $HTA$ ), and analogy factor ( $A$ ), are used. They are defined as

$$DR = \frac{C_{f0} - C_f}{C_{f0}}, \quad HTA = \frac{St - St_0}{St_0}, \quad A = \frac{St/St_0}{C_f/C_{f0}}, \quad (D.11)$$

where  $C_f$  and  $St$  represents the space and time averaged values of the skin friction coefficient and Stanton number for the controlled flow (It should be noted that the fringe region is excluded while calculating the spatial average). Here, the subscript zero is used to indicate the respective values for the uncontrolled flow. The purpose of the present study is to make  $A$  larger than unity and thus achieve dissimilar heat transfer enhancement.

### D.1.3 Parametric study

Parametric study was carried out to confirm the applicability of streamwise traveling-wave-like wall blowing and suction to generate dissimilar control in a laminar developing flow. Here the control input is given by

$$\phi = a \sin \left\{ \frac{2\pi}{\lambda_x} (x - U_p t) \right\}, \quad (D.12)$$

where  $a$ ,  $\lambda_x$ , and  $U_p$  are the amplitude, wavelength, and phase speed of the traveling wave. To ensure zero-net-mass-flux wall blowing and suction the control input is applied in sinusoidal mode, *i.e.*, identical sinusoidal traveling wave is applied at both the top and bottom walls. The wavelength and phase speed of the traveling wave are kept uniform along

the streamwise direction. The amplitude of the control input is also kept uniform along the streamwise direction except in the fringe region, where the control input varies as  $\phi_{fringe} = \phi[0.5 + 0.5 \cos \pi(x - 18)]$ . We then chose those parameters of the traveling wave, that maximise the analogy factor. Wall blowing and suction in the form of a traveling wave, characterised by the chosen wave parameters, is then employed as the initial control input for the optimal control analysis.

#### D.1.4 Optimal control analysis

In this method the control input is optimised by minimizing the cost functional defined as

$$J = \frac{1}{T \cdot S} \int_0^T \int_S \left\{ \frac{1}{2} \phi^2 + \left( -\frac{1}{Re} \frac{\partial u}{\partial x_j} + \frac{1}{Pe} \frac{\partial \theta}{\partial x_j} \right) n_j \right\} dS dt, \quad (D.13)$$

where  $S$  is the overall area of top and bottom walls, and  $n_j$  is the unit outward normal vector at the boundary. The first term corresponds to the cost of the control input. The second and third terms are the cost and merit of wall friction and wall heat flux, respectively. The temporal integration specifies the time period over which we modify the wall friction and wall heat flux, and  $T$  is called the time horizon.

The minimization of  $J$ , by applying zero-net-mass-flux wall blowing and suction ( $\phi$ ), have to be carried out under the restrictions given by the governing equations (D.4) to (D.6) for the velocity and temperature fields. This optimization problem can be solved by minimizing the following Hamiltonian given by

$$H = J + \left\langle u_i^* \left\{ \frac{\partial u_i}{\partial t} + \frac{\partial (u_j u_i)}{\partial x_j} + \frac{\partial p}{\partial x_i} - \frac{1}{Re} \frac{\partial^2 u_i}{\partial x_j \partial x_j} - \eta_u (u_i^{in} - u_i) \right\} - p^* \left( \frac{\partial u_i}{\partial x_i} \right) + \theta^* \left\{ \frac{\partial \theta}{\partial t} + \frac{\partial (u_j \theta)}{\partial x_j} - \frac{1}{Pe} \frac{\partial^2 \theta}{\partial x_j \partial x_j} - \eta_\theta (\theta^{in} - \theta) \right\} \right\rangle_V, \quad (D.14)$$

where  $u_i^*$ ,  $p^*$ , and  $\theta^*$  are the Lagrangian multipliers, which are called also as the *adjoint* variables. Here,  $V$  represents the volume of the computational domain. Hereafter, a quantity with an asterisk represents an adjoint variable. The bracket in equation (D.14) represents the spatio-temporal integral given as

$$\langle \cdot \rangle_V \equiv \int_0^T \int_V \cdot dV dt. \quad (D.15)$$

Now, for an arbitrary infinitesimal change of the control input, *i.e.*  $\phi'(x, z, t)$ , where a dashed quantity represents a perturbation, the corresponding changes in the velocity, pressure, temperature, cost functional, and Hamiltonian are respectively defined as

$$u'_i \equiv \frac{\mathcal{D}u_i}{\mathcal{D}\phi}\phi', \quad p' \equiv \frac{\mathcal{D}p}{\mathcal{D}\phi}\phi', \quad \theta' \equiv \frac{\mathcal{D}\theta}{\mathcal{D}\phi}\phi', \quad J' \equiv \frac{\mathcal{D}J}{\mathcal{D}\phi}\phi', \quad H' \equiv \frac{\mathcal{D}H}{\mathcal{D}\phi}\phi', \quad (\text{D.16})$$

where  $\mathcal{D}/\mathcal{D}\phi$  represents the Frechét differential operator with respect to  $\phi$ .

On applying the Fréchet differential to  $H$  we get

$$\begin{aligned} H' = & J' + \left\langle u_i^* \left\{ \frac{\partial u'_i}{\partial t} + \frac{\partial (u'_j u_i + u_j u'_i)}{\partial x_j} + \frac{\partial p'}{\partial x_i} - \frac{1}{Re} \frac{\partial^2 u'_i}{\partial x_j \partial x_j} + \eta_u u'_i \right\} - p^* \left( \frac{\partial u'_i}{\partial x_i} \right) \right. \\ & \left. + \theta^* \left\{ \frac{\partial \theta'}{\partial t} + \frac{\partial (u'_j \theta + u_j \theta')}{\partial x_j} - \frac{1}{Pe} \frac{\partial^2 \theta'}{\partial x_j \partial x_j} + \eta_\theta \theta' \right\} \right\rangle_{\Omega}. \end{aligned} \quad (\text{D.17})$$

On rearranging the terms, equation (D.17) can be written as

$$\begin{aligned} H' = & \left\langle u'_i \left\{ -\frac{\partial u_i^*}{\partial t} - u_j \left( \frac{\partial u_i^*}{\partial x_j} + \frac{\partial u_j^*}{\partial x_i} \right) + \frac{\partial p^*}{\partial x_i} - \theta^* \frac{\partial \theta^*}{\partial x_i} - \frac{1}{Re} \frac{\partial^2 u_i^*}{\partial x_j \partial x_j} + \eta_u u_i^* \right\} \right. \\ & \left. - p' \left( \frac{\partial u_i^*}{\partial x_i} \right) + \theta' \left\{ -\frac{\partial \theta^*}{\partial t} - u_j \frac{\partial \theta^*}{\partial x_j} - \frac{1}{Pe} \frac{\partial^2 \theta^*}{\partial x_j \partial x_j} + \eta_\theta \theta^* \right\} \right\rangle_{\Omega} + B, \end{aligned} \quad (\text{D.18})$$

where  $B$  is called the ‘boundary-term’ which depends only on initial and boundary conditions. The adjoint equations given below are derived such that all the terms except  $B$  vanishes from equation (D.18),

$$\frac{\partial u_i^*}{\partial t^*} - u_j \left( \frac{\partial u_i^*}{\partial x_j} + \frac{\partial u_j^*}{\partial x_i} \right) = -\frac{\partial p^*}{\partial x_i} + \theta^* \frac{\partial \theta^*}{\partial x_i} + \frac{1}{Re} \frac{\partial^2 u_i^*}{\partial x_j \partial x_j} - \eta_u u_i^*, \quad (\text{D.19})$$

$$\frac{\partial u_i^*}{\partial x_i} = 0, \quad (\text{D.20})$$

$$\frac{\partial \theta^*}{\partial t^*} - u_j \frac{\partial \theta^*}{\partial x_j} = \frac{1}{Pe} \frac{\partial^2 \theta^*}{\partial x_j \partial x_j} - \eta_\theta \theta^*. \quad (\text{D.21})$$

It should be noted that the adjoint equations are solved backward in time, so that  $t^*$  is defined as  $t^* = T - t$ . On applying proper initial and boundary conditions:  $u'_i = \theta' = 0$  at  $t = 0$ ;  $u_i^* = \theta^* = 0$  at  $t^* = 0$ ;  $(u', v', \theta') = (0, \phi', 0)$  and  $(u^*, v^*, \theta^*) = (-1, 0, 1)$  at the wall, the



Table D.1 Control Performance

	$C_f/2$	$DR$	$St$	$HTA$	$A$
Uncontrolled flow	0.0358	—	0.0193	—	—
sinusoidal traveling wave control with $\lambda_x = 4$ and $U_p = 0.60$	0.0448	-25.13%	0.0284	+47.15%	1.178
Optimal control	0.0025	+93.01%	0.0419	+117.09%	31.08

boundary term  $B$  reduces to a simple form. As a result, equation (D.18) ends up with

$$H' = \left\langle (\phi - p^* n_2) \phi' \right\rangle_S. \quad (D.22)$$

So minimization of  $H$ , *i.e.*  $H' < 0$ , can be achieved by taking the following form for  $\phi'$ :

$$\phi' \propto -(\phi - p_{wall}^* \cdot n_2). \quad (D.23)$$

It should be noted that  $n_2$  is 1 and  $-1$  at the top and bottom walls, respectively. equation (D.23) indicates that the control input is updated based on the adjoint pressure. The adjoint pressure appearing in equation (D.23) can be obtained by solving the governing equations (D.19) to (D.21).

### D.1.5 Results

As the first step, we conducted a parametric study to find out the most suitable values for the wavelength and phase speed for the traveling wave that maximizes the analogy factor. This was done by keeping the amplitude as 10% of  $U_\infty$ . As a result, the maximum value for the analogy factor of  $A = 1.178$  is obtained for  $\lambda_x = 4$  and  $U_p = 0.60$ . This traveling wave, with the wave parameters obtained from the parametric study, is then applied as the initial control input for the optimal control.

For the optimal control analysis, the control input is optimized over a time period corresponds to 1.5 times flow-through time ( $T = 30$ ), and zero-net-mass-flux wall blowing and suction is ensured by enforcing a sinuous mode configuration for the control input. The resulting cost functional decreases monotonically and reaches a minimum at an iteration number equal to 218 as shown in figure D.2. Comparison of the control performances obtained by the optimal control and the parametric survey are given in Table D.1.

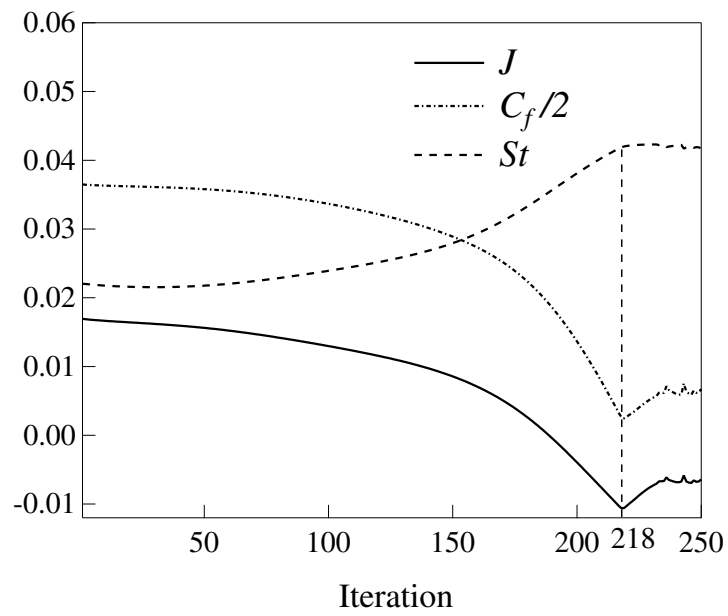


Figure D.2 Update of cost functional ( $J$ ), skin friction coefficient ( $C_f/2$ ), and Stanton number ( $St$ ) with iteration.

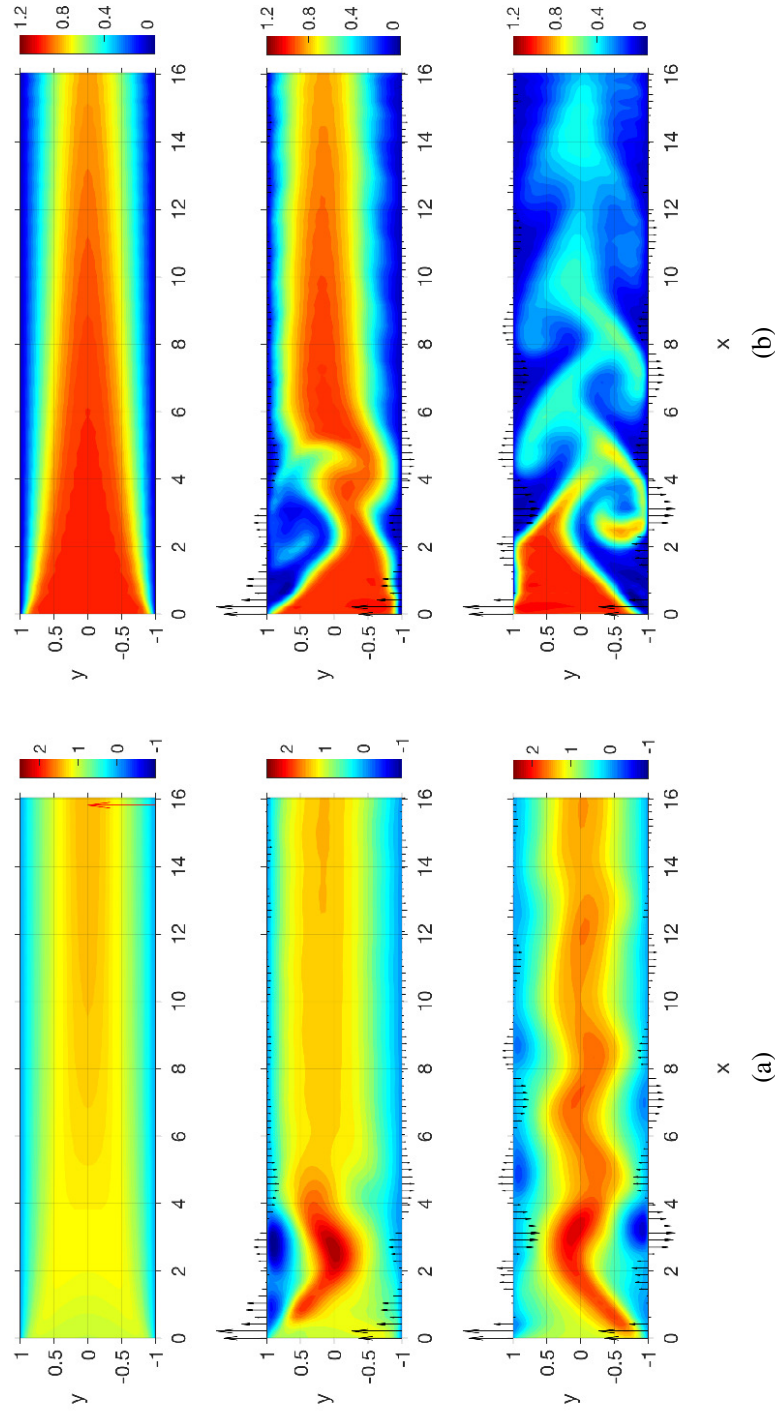


Figure D.3 Snapshots of the streamwise velocity field (*left*) and temperature field (*right*) for three different time steps: from top to bottom,  $t = 0$  (*initial field*);  $t = 4$ ;  $t = 27$ . The velocity vectors shown at the top and bottom wall represent the profile of the optimal control input for that particular time instant. A unit wall normal velocity vector is shown at  $x = 15.83$  in the velocity field for  $t = 0$  (top left figure) using a red arrow, as a reference.

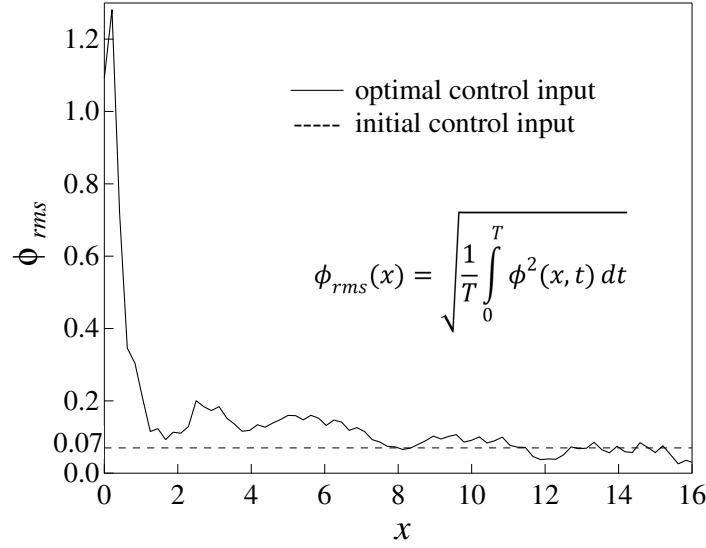


Figure D.4 The streamwise variation of the RMS value of the control input.

Three set of snapshots (each set contains one snapshot of streamwise velocity and temperature field) for the optimal control flow are shown in figure D.3. The first set of snapshots at  $t = 0$  corresponds to the initial flow field, taken from the uncontrolled developing flow. The second set of snapshots at  $t = 4$  shows the early stage in the evolution of the optimal control input. The flow field at  $t = 27$  (towards the end of the optimization-time-horizon) is shown in the third set of snapshots. As can be seen from the second and third snapshots, the control input has a relatively high magnitude near the inlet of the channel. This is also visible in figure D.4, where the RMS value of the control input is plotted as a function of the streamwise coordinate.

The recirculation region generated near the wall (due to high magnitude control input) causes a reduction in the skin friction coefficient and an increase in heat transfer near the wall. The magnitude of the dissimilarity keeps decreasing with the distance from the inlet due to the decrease in the control input magnitude. It can also be seen from the third snapshot that the wavelength of the control input increases as we go along the streamwise direction. Also, using the contour plot (not shown here) of the correlation coefficient , $CC$ , defined as

$$CC(\Delta x, \Delta t : x_0) = \frac{\int_t^{t+t_p} \phi(x_0, t) \phi(x_0 + \Delta x, t + \Delta t) dt}{\sqrt{\int_t^{t+t_p} \phi^2(x_0, t) dt} \sqrt{\int_t^{t+t_p} \phi^2(x_0 + \Delta x, t + \Delta t) dt}} \quad (D.24)$$

it was be found that the wavelength and the phase speed does not vary significantly from the initial control input, namely,  $\lambda_x = 4$  and  $U_p = 0.60$ . This means that the optimal control mostly changes the streamwise distribution of the intensity of the initial control input.

Our study shows that traveling-wave-like wall blowing and suction can generate dissimilar control effect even for a developing laminar channel flow at low Reynolds number. The optimal control analysis further reveals that the wave parameters, that characterise the optimal traveling wave, vary along the streamwise direction. The normalised wavelength varies about  $\lambda_x = 4$  and the normalised phase speed varies about  $U_p = 0.60$ . We found that, due to relatively high magnitude of the control input very close to the inlet of the channel, maximum dissimilarity is generated in that region.